

RIGA TECHNICAL UNIVERSITY
Faculty of Civil Engineering
Institute of Materials and Structures

Andrejs KOVALOVŠ

**ACTIVE TWIST DESIGN
OF HELICOPTER ROTOR BLADES**

Doctoral Thesis

Scientific supervisors:

Professor, Dr. sc. ing.
A. Chate

Professor, Dr. sc. ing.
E. Barkanov

RIGA 2015

ABSTRACT

In time of helicopter flight rotor blades produce significant vibration and noise as a result of variations in rotor blade aerodynamic loads with blade azimuth angle. For this reason future helicopters need to be improved with respect to environmental and public acceptance. The active twist control of helicopter rotor blades by an application of embedded piezo-composite actuators leads to significant vibration and noise reduction without the need for complex mechanisms in the rotating systems.

For the design of a rotor blade with active twist, a new design methodology was developed. This methodology is based on the new 3D finite element model, planning of experiments and response surface technique to obtain high piezoelectric actuation forces and displacements with the minimal actuator weight and energy applied. To investigate an active twist of the helicopter rotor blade, the structural static analysis with thermal load using 3D finite element model was developed by finite element software ANSYS. An optimisation problem for the optimum placement of MFC actuators in the helicopter rotor blade was formulated based on the results of parametric study of the rotor blades with C- and D- spars in model scale and taking into account the producer's requirements.

Optimisation results were obtained for two rotor blades with C- and D- spars in model and full scales and with two possible applications of the MFC actuators. Results shows that D-spar is more effective than C-spar in terms of minimal distance between location of centre of gravity and elastic axis, but the obtained maximal torsion angles are practically the same for both rotor blades.

Torsion angle obtained from the finite element simulation of helicopter rotor blades was successfully validated by experimental value to confirm the modelling accuracy. Design Tool was produced using the methodology developed for the optimum placement of actuators in the helicopter rotor blades. Designer can find compromise between necessary solutions using optimal results obtained or applying the developed Design Tool.

ANOTĀCIJA

Lidojuma laikā helikoptera rotora lāpstiņa rada stipras vibrācijas un trokšņus, kuru cēlonis ir izmaiņas aerodinamiskajās slodzēs uz lāpstiņām, mainoties to polārajam leņķim. Tādēļ nākotnes helikopteri ir jāuzlabo, lai tie būtu videi un cilvēkam nekaitīgāki. Rotora lāpstiņu savērpes aktīvā regulēšana ar iemontētiem pjezokompozītu aktuatoriem ļauj šīs vibrācijas un troksni samazināt, nelietojot sarežģītus mehānismus rotējošā sistēmā.

Lai projektētu rotora lāpstiņu ar aktīvo savērpi, ir izstrādāta jauna metodoloģija. Tā balstās uz jaunu 3D galīgo elementu modeli, eksperimentu plānošanu un reakcijas virsmas tehniku, lai iegūtu lielus pjezoelektriskās aktuācijas spēkus un pārvietojumus ar minimālu aktuatora svaru un pievadīto enerģiju. Lai izpētītu rotora lāpstiņu ar aktīva savērpi, tika veikta konstrukcijas statistiskā analīze, izmantojot 3D galīgos elementu modeli un programmatūru ANSYS. Izmantojot rezultātus, kas iegūti, veicot parametrisko analīzi, modeļa mēroga rotora lāpstiņām ar C- un D- lonžeroniem un ņemot vērā ražotāja prasības ir formulēta problēma par MK aktuatoru optimālu izvietošanu rotora lāpstiņās.

Optimizācijas rezultāti ir iegūti modeļa un pilna izmēra lāpstiņām ar C- un D- lonžeroniem divos MK aktuatoru iespējamajos pielietojumos. Rezultāti rāda, ka attiecībā uz minimālo attālumu starp smaguma spēka novietojumu un elastīgo asi, D- lonžerons ir efektīvāks par C- lonžeronu, bet maksimālie savērpes leņķi abos gadījumos ir vienādi.

Ar galīgo elementu metodi atrastais lāpstiņu savērpes leņķis labi sakrīt ar eksperimentos iegūto, kas apstiprina modelēšanas precizitāti. Izmantojot izstrādāto metodoloģiju, ir izveidots projektēšanas instruments aktuatoru optimālai izvietošanai rotora lāpstiņās. Projektētājam ir iespējamā izvēlēties vai nu lietot iegūtos optimālos rezultātus vai izmantot šo projektēšanas instrumentu.

Šo pētījumu atbalstīja Eiropas Komisijas FRAMEWORK6 programma, kontrakts No. AIP3-CT-2003-502773, ar nosaukumu "Integration of technologies in support of a passenger and environmentally friendly helicopter" (FRIENDCOPTER) un šis darbs izstrādāts ar Eiropas Sociālā fonda atbalstu Nacionālās programmas „Atbalsts doktorantūras programmu īstenošanai un pēcdoktorantūras pētījumiem” projekta „Atbalsts RTU doktorantūras attīstībai” ietvaros.

ACKNOWLEDGMENTS

I would like to thank my supervisors Prof. Evgeny Barkanov and Prof. Andris Chate for their guidance and support throughout my career at the Riga Technical University and help on writing and presenting my work. Provision of the financial support and software during the research is also greatly acknowledged. It is a great benefit and honour to work with them.

Furthermore, I wish to thank my colleagues from the Institute of Materials and Structures for creating a pleasant and inspiring working atmosphere.

Finally, I want to thank my family for their support regardless of what I do. And I want to address a special thanks to my wife, Zanna, for taking care of me every day.

This work was supported by the:

European Commission under FRAMEWORK6 program, contract No. AIP3-CT-2003-502773, integrated project “Integration of technologies in support of a passenger and environmentally friendly helicopter” (FRIENDCOPTER) [37].

European Social Fund within the project «Support for the implementation of doctoral studies at Riga Technical University».



TABLE OF CONTENTS

| | |
|--|----|
| ABSTRACT | 2 |
| ANOTĂCIJA..... | 3 |
| ACKNOWLEDGMENTS | 4 |
| TABLE OF CONTENTS | 5 |
| INTRODUCTION | 7 |
| 1. LITERATURE REVIEW | 8 |
| 1.1. Helicopter vibration reduction | 8 |
| 1.1.1. Main rotor vibration | 8 |
| 1.1.2. Passive vibration reduction | 11 |
| 1.1.3. Active vibration reduction..... | 11 |
| 1.2. Active twist rotor blades | 14 |
| 1.2.1. Experimental testing of the Active Twist Rotor blades | 15 |
| 1.2.2. Numerical study of the Active Twist Rotor blades | 23 |
| 1.2.3. Active Twist Optimisation | 28 |
| 1.3. Thesis objectives..... | 30 |
| 1.4. Structure of thesis | 30 |
| 2. STRUCTURE OF HELICOPTER ROTOR BLADES | 32 |
| 2.1. Model scale rotor blades | 32 |
| 2.1.1. Rotor blade with C-spar | 32 |
| 2.1.2. Rotor blade with D-spar | 35 |
| 2.2. Full scale rotor blade..... | 36 |
| 3. FINITE ELEMENT SIMULATION OF HELICOPTER ROTOR BLADES | 38 |
| 3.1. Finite element model | 38 |
| 3.2. Finite element analysis..... | 39 |
| 3.2.1. Thermal analogy..... | 39 |
| 3.2.2. Calculation of the elastic axis | 46 |
| 3.2.3. Modal analysis | 48 |
| 3.3. Convergence study..... | 49 |
| 3.4. Parametric study | 51 |
| 3.4.1. Rotor blade with C-spar | 52 |
| 3.4.2. Rotor blade with D-spar | 55 |
| 4. DESIGN OPTIMISATION METHODOLOGY | 57 |

| | |
|--|-----|
| 4.1. Optimisation problem statement..... | 57 |
| 4.2. Optimisation methodology | 61 |
| 4.2.1. Experiment design..... | 63 |
| 4.2.2. Response surface approximation..... | 65 |
| 4.2.3. Random search method | 68 |
| 5. OPTIMAL DESIGN OF MODEL SCALE ROTOR BLADES..... | 70 |
| 5.1. Optimisation results | 70 |
| 5.1.1. Solution of optimisation problem..... | 70 |
| 5.1.2. Rotor blade with C–spar | 75 |
| 5.1.3. Rotor blade with D–spar | 76 |
| 5.2. Comparative study | 77 |
| 5.3. Parametric study by response surfaces | 78 |
| 5.4. Experimental verification | 81 |
| 5.5. Design Tool..... | 84 |
| 6. OPTIMAL DESIGN OF FULL SCALE ROTOR BLADE | 88 |
| 6.1. Upscaling problem..... | 88 |
| 6.2. Optimisation results of full scale rotor blade..... | 90 |
| 6.2.1. Solution of optimisation problem..... | 90 |
| 6.2.2. Influence of the location of centre of gravity..... | 93 |
| 6.2.3. Optimal operating voltage..... | 94 |
| 7. CONCLUSIONS | 96 |
| REFERENCES | 99 |
| APPENDIX A. Parametric study of rotor blade with C– spar | 107 |
| APPENDIX B. Parametric study of rotor blade with D– spar | 113 |
| CURRICULUM VITAE | 120 |

INTRODUCTION

Like other transport systems, helicopters generate external vibration and noise due to the complex nature of their dynamic systems and suffer from NOx emission. It is therefore very essential that the new generation rotorcraft address these issues to improve the situation, to make them environmentally friendly and acceptable to the general public. The modern society needs this indispensable system due to its ability to fly medical, rescue and law enforcement missions. These missions require flight profiles close to populated areas.

Vibratory loads and noise in helicopters arise from a variety of sources such as the main rotor, tail rotor, engine, gearbox and fuselage. However, the most dominant source of vibration and noise is the main rotor, when the unsteady aerodynamic environment acting on highly flexible rotating blades. The high vibration in helicopter leads to discomfort of passenger, increase pilot workload, reduce component fatigue life, limit forward flight speeds and increase maintenance costs.

The traditional vibration reduction technique was a passive approach using, with vibration isolators and absorbers. However, this methodology imparts undesirable weight penalties and insufficient vibration reduction. Later, new control techniques were developed. This strategy involves active approach such as Higher Harmonic Control (HHC) and Individual Blade Control (IBC). Disadvantages of this concept are adverse power requirements, limitation on excitation frequencies in HHC and extreme mechanical complexity of hydraulic sliprings in IBC.

With an emergence of active materials, such as Active Fibre Composites and Macro Fibre Composites, the Active Twist Rotor concept was proposed. These new actuators only required electrical power to operate and do not require the complicate mechanical devices into to rotating system. Two main concepts were considered under development for the active material application: rotor blade flap actuation and blade twist actuation. Advantage of active twist actuation is simplicity of its actuation mechanism compared with that for flap actuation. This technology will allow to: blowing away the blade tip vortices responsible for the blade slap noise, use thin blade tips but delay flow separation through high blade incident angles leading to lower power requirement and generate secondary excitation loads counteracting the original unsteady forces and moments at the rotor hub. Finally, the piezoceramic actuators integrated and distributed into the rotor blade skin generate dynamic blade twist and camber adapted to the flight condition at any given time, which leads to significant vibration and noise reduction and improves flight performance.

1. LITERATURE REVIEW

This chapter presents an introduction to the vibration reduction with actively controlled twist blade, starting with some background and basic concepts for helicopter vibrations. The first section offers an introduction to the vibration reduction where various methodologies were examined in attempt to reduce the vibration. The next section is addressed to the problem of actively twisting of rotor blades evaluated to reduce rotorcraft vibration and noise levels. Finally, the structure and objectives of this thesis are presented.

1.1. Helicopter vibration reduction

This section provides literature overview of helicopter vibration reduction, by using different methodologies.

1.1.1. Main rotor vibration

Vibratory loads and noise in helicopters arise from a variety of sources such as the main rotor, tail rotor, engine, gearbox and fuselage. However, the most dominant source of vibration and noise is the main rotor, because of the unsteady aerodynamic environment acting on highly flexible rotating blades. The vibration level is generally low in hover, where the aerodynamic environment is almost axisymmetric and increases with higher forward speed. There are two regimes: low speed flight (transition) and high-speed flight, where the vibration levels are critical (Figure 1.1). There is typically a peak in the vibration level due to blade vortex interaction (BVI) which results in a substantially higher harmonic on the rotor. At low forward speed, the blade tip vortices in the wake stay close to the rotor disk, causing a severe blade vortex interaction which results in a substantially higher harmonic loading (Figure 1.2).

At high forward speed, the rotor disk tilts forward and the wake is swept away from the disk plane; the wake-induced vibrations become small at high advance ratio (Figure 1.2). In this case the dominant vibratory load is dynamical stall. At still higher flight velocities, the vibration again increases, primarily as a result of the higher harmonic loading produced by stall at the retreating blade and compressibility effects at the advancing side [55].

Vibratory loads of the rotor hub coming from the unsteady aerodynamic environment in which the rotor blades are operating. This highly periodic aerodynamic environment creates large periodic variations in blade velocity and angle of attack, and corresponding large

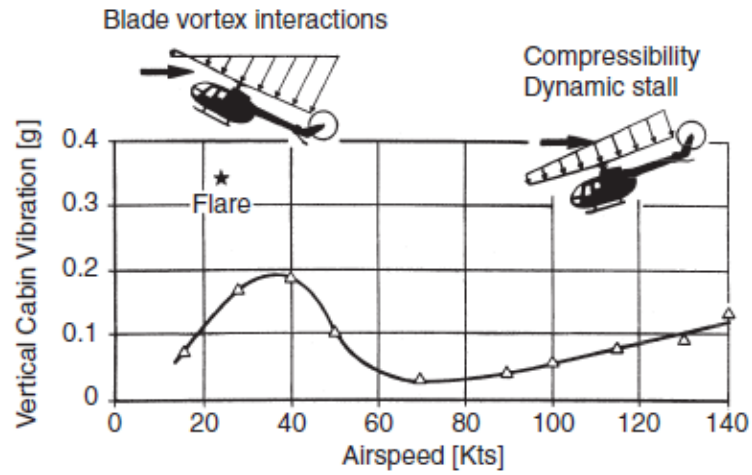
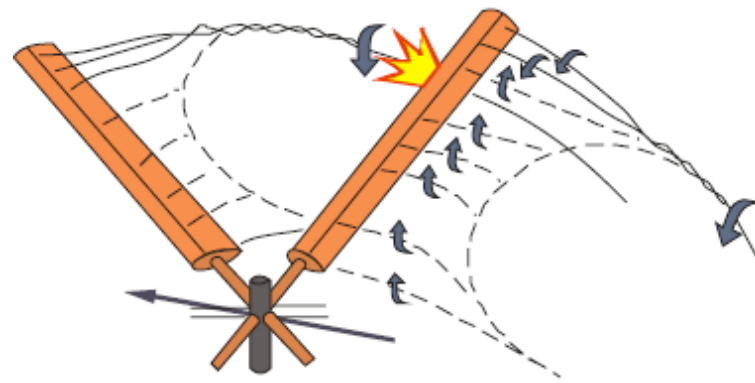
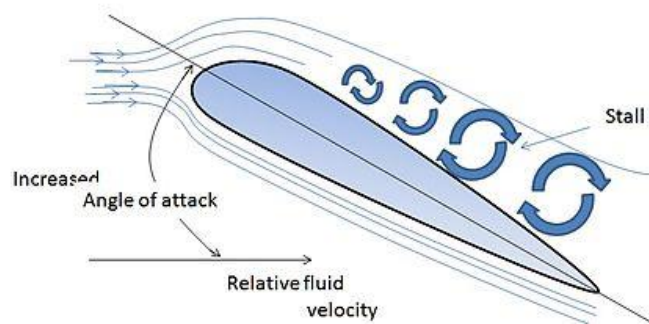
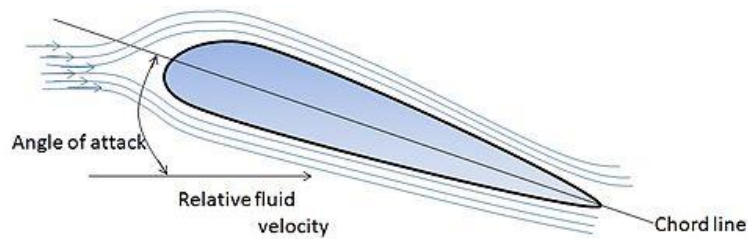


Figure 1.1. Vibration amplitude BO 105 as a function of airspeed [106]



a)



b)

Figure 1.2. Illustration of: (a) BVI [70], (b) dynamic stall [122]

periodic vibratory loads on the blades. A typical aerodynamics environment of the helicopter main rotor during forward flight is illustrated in Figure 1.3 where helicopter flight velocity adds to the blade element rotating velocities on the advancing side ($0^\circ < \psi < 180^\circ$) and subtracts from it on the retreating side ($180^\circ < \psi < 360^\circ$).

The resulting aerodynamic environment may be characterized as follows: high tip Mach number on the advancing side, and blade stall effects on the retreating side. A reverse flow region is also generated at the inboard on the retreating side. Such a complicated environment results in an instantaneous asymmetry of the aerodynamic loads acting among the blades at different azimuthal locations. This results in a vibratory response of a flexible blade structure, adding more complexity to the air loads asymmetry. This vibration is transmitted to the fuselage at the frequency of N_b/rev , where N_b is the number of blades. The mechanism becomes a primary source of fuselage excitation.

At present time in literature, the various methodologies for vibration reduction involving the passive and active strategies may be found. The next sections briefly overview these methodologies.

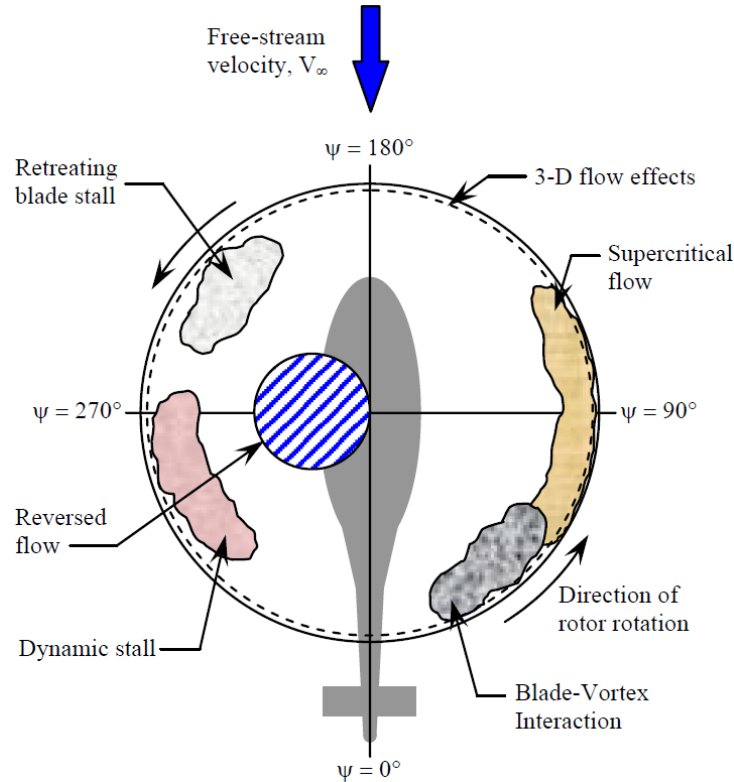


Figure 1.3. Rotary-wing flight vehicle aerodynamic environment in forward flight [118]

1.1.2. Passive vibration reduction

Since vibration is such a severe problem for the rotorcraft vehicles, a high priority was placed on the developing techniques for reducing vibrations and vibratory loads. Traditionally, vibration reduction is achieved by passive means such as pendulum absorbers and isolators. It is usually a single ‘degree of freedom’ (DOF) system with a small mass and a spring. Good reviews of passive vibration reduction methods are given by Reichert [80] and Loewy [66]. The main disadvantage of passive methods is that they have limited effectiveness over a narrow range of operating conditions and introduce weight penalties.

The second passive approach is blade design optimisation as another effective alternative for reducing helicopter vibration. The rotor blade fundamental properties (such as structural and aerodynamic) are chosen optimally to reduce overall vibration in the designing phase [39, 36, 13]. In this approach, the vibration reduction problem is formulated as a mathematical optimisation function with appropriate objective function and constraints. For the aerodynamic shape, sweep, anhedral, droop, etc., at the blade tip are considered as the design variables. For a composite rotor blade, the ply angles and thicknesses or any other cross-sectional parameters of spar can be used as the design variables. In many cases, both structural and aerodynamic shape optimisation design variables are used simultaneously. This approach do not have any weight penalty but the vibration reduction achieved is from 10 to 40% at a particular flight condition when the vibration characteristic of the rotor blade may change during operation depending on; the amount of fuel left in the fuel tank, the weight and location of payloads, rotor RPM, and aircraft speeds.

1.1.3. Active vibration reduction

During the last two decades, several approaches of active control were investigated by researchers which can be efficient over a wide range of operating conditions and result in limited weight penalty. The most commonly examined active vibration reduction strategies include Higher Harmonic Control (HHC) and Individual Blade Control (IBC).

The main objective of the HHC concept is to generate higher harmonic unsteady aerodynamic loads on the rotor blades that cancel the original loads responsible for the vibration (Figure 1.4). The unsteady aerodynamic loads are introduced by adding higher harmonic pitch input through actuation of the swash plate at higher harmonics. In HHC actuators are located below the swashplate, i.e. actuation takes place in the nonrotating system.

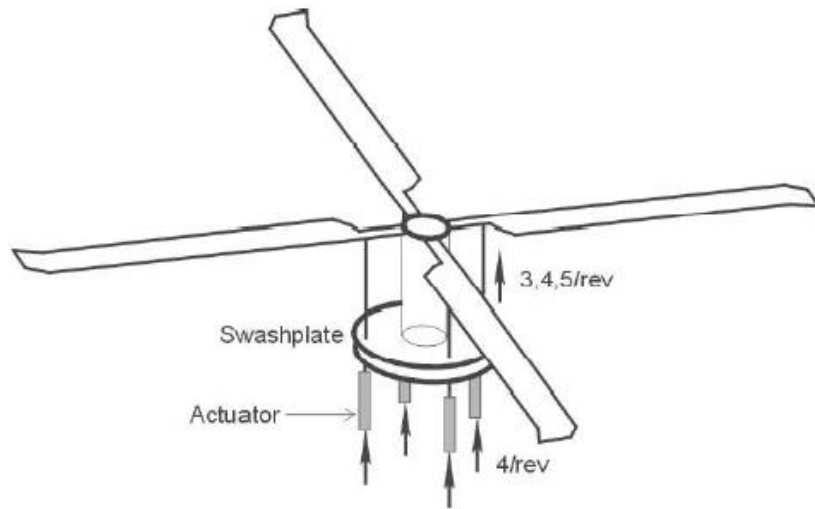


Figure 1.4. Scheme of a Higher Harmonic Control (HHC) [58]

HHC was demonstrated to reduce vibrations through numerical simulations [74, 75, 79], model and full scale wind tunnel tests [46, 97 73], as well as full-scale flight tests [120, 102, 109].

Individual Blade Control is another active strategy that was widely explored for helicopter vibration reduction. The main idea of IBC is similar to that of HHC (generating unsteady aerodynamic loads to cancel the original vibration), but with a different implementation method (Figure 1.5). The actuators used in IBC control the pitch of each blade individually at any combination of frequencies [57]. A hydraulic slip ring unit is required to transmit the hydraulic power to the actuators in the rotating frame the IBC concept can be extended to other important applications, such as noise reduction, lag damping augmentation, and stall, flutter suppression.

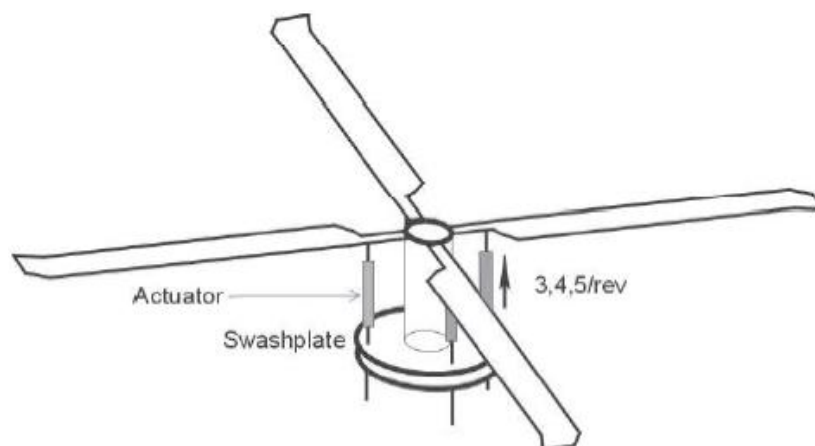


Figure 1.5. Scheme of Individual Blade Control (IBC) [58]

Several studies on this approach were conducted at Massachusetts Institute of Technology (MIT), and are well summarized in References [45, 43, 44]. Full-scale wind tunnel tests of this system were conducted at the National Aeronautics and Space Administration (NASA) Ames Research Center [50, 51, 52]. Several flight tests of the IBC system for vibration reduction were conducted successfully [64].

Higher Harmonic Control as well as Individual Blade Control for helicopter rotors promises to be a method to increase flight performance and to reduce vibration and noise. However, both approaches have limitations on their practical implementation. Apart from the considerable weight penalties and high cost, large actuation power is needed to pitch the entire blades.

To overcome many of the problems associated with the existing schemes of helicopter vibration reduction, considerable research was directed recently towards the applications of smart structures technology to actively control vibration in rotorcraft systems. The concept of trailing-edge flap was explored extensively for vibration reduction. This concept uses a small flap on each blade to generate the desired unsteady aerodynamic loads (Figure 1.6).

This concept can be equally effective, but uses less power than the conventional IBC system. In this approach, a partial span trailing edge flap is located in the outboard region of the blade. The active flap control inputs affect the blade inertial loads and rotor dynamics as well as the unsteady aerodynamic loads. In this method, one or more on-blade trailing-edge flaps, each of them spanning about 4–6 percent of the blade are actuated. This approach substantially reduces the control power for actuation when compared to HHC and IBC.

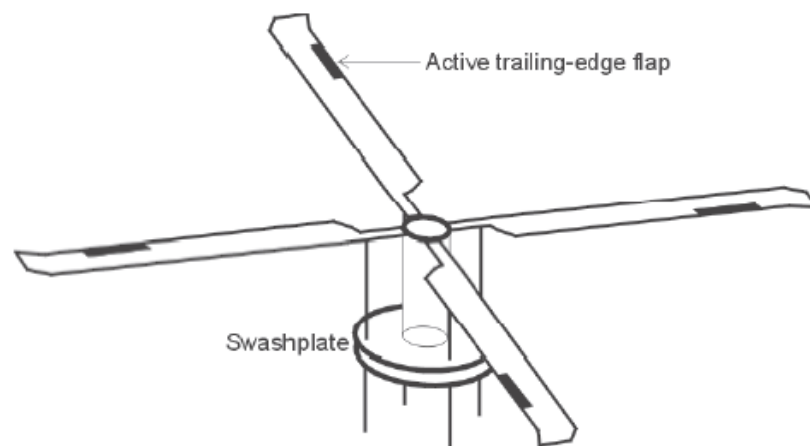


Figure 1.6. Scheme of Active Trailing-edge Flap (ATF) [58]

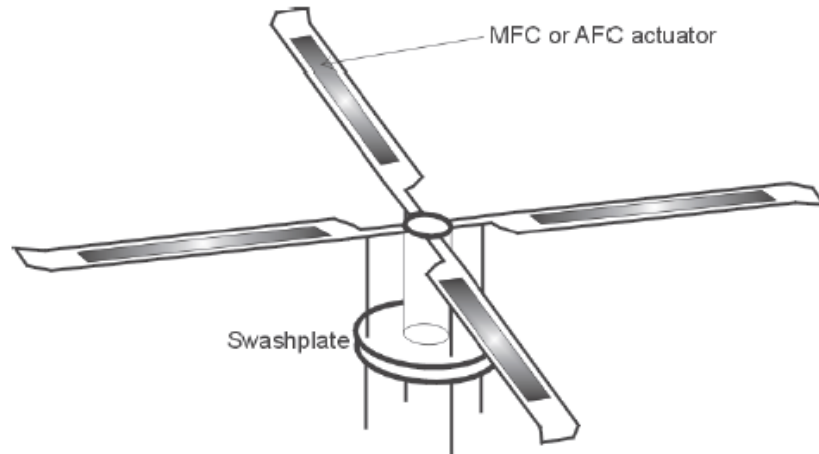


Figure 1.7. Scheme of Active Twist Rotor (ATR) [58]

Actively controlled trailing–edge flaps represent one of the most promising methods for vibration reduction in helicopters because of low power consumption, light weight, compact size, airworthiness and high adaptation. A number of analytical simulations [68, 104, 105], some wind tunnel tests [38, 59, 58] and full–scale whirl tower test [103, 35] of the active flap have demonstrated that it has the potential to significantly reduce the vibratory loads, alleviate noise, enhance the rotor performance and handling qualities.

With the emergence of smart materials, such as Active Fibre Composites and Macro–Fibre Composites the Active Twist Rotor (ATR) concept was proposed (Figure 1.7). The idea behind active twist is to modify the twist and the torsional stiffness of the rotating blade not only to improve the lift and the global helicopter performance but also to actively damp vibrations.

Main advantages of the active twist are the aerodynamically unchanged profile and the simplicity of its actuation mechanism compared to the active trailing–edge flap actuation. The detailed literature review will be described on the active twist rotor in Section 1.2.

1.2. Active twist rotor blades

This section provides literature review about active twist concepts on helicopter blades. The existing literature is classified into the three following sections: experimental testing, numerical simulation of the Active Twist Rotor blades and mathematical optimisation of the cross-section properties of the rotor blades.

1.2.1. Experimental testing of the Active Twist Rotor blades

The objective of active twist rotor is to reduce the vibration or Blade Vortex Interaction noise in helicopter rotor blade using active twist approach. This approach has gained popularity over the past decade. The early studies are mostly experimental in nature with simple modelling and were undertaken to prove the concept of active twist control using piezoceramic materials. The key idea was to check if the required $\pm 2^\circ$ of twist needed for suppressing vibration dramatically could be obtained with minimum consumption of power. A comprehensive literature review on active twist control of smart helicopter rotor can be found in Thakkar and Ganguli [108] and is briefly summarized in following sections.

The first active–twist rotor, using direct twist actuation, was developed by Chen and Chopra [24]. Chen and Chopra built a Froude–scale model rotor and concurrently developed an analytical model to predict the behaviour of the rotor blades with embedded piezo–ceramic actuators. For this, a uniform strain theory was formulated to predict the static torsion and bending response of rectangular section beams and rotor blades, followed by experimental validation.

Experiments were conducted on a 1.83m diameter, 1/8th Froude scale model of a two–bladed bearingless rotor [26, 27, 23]. The blade cross–section was NACA 0012. Total blade length was 67.51cm from tip to root and chord was 7.62cm. As seen in Figure 1.8, Chen and Chopra embedded piezoelectric actuators at a $+45^\circ$ in the upper skin and -45° in the lower skin to produce a shear strain that twists the blade. The piezo elements extended from approximately 17.5% to 70% chord and the ratio of piezo to fiberglass skin thickness was of the order of 4:1.

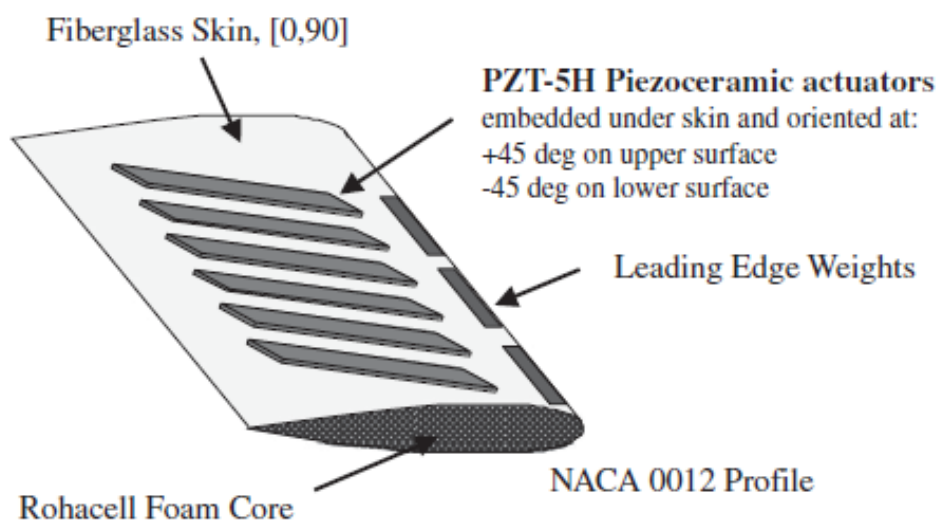


Figure 1.8. Active twist rotor using piezoceramic sheet actuators [29]

Two rotor configurations were built with varying actuator geometries to study the effect of actuator spacing and actuator thickness on the blade torsional response. The first configuration had 55 pairs of actuators spaced 0.254 cm apart and the second configuration had 12 pairs of actuators spaced 3.81cm apart. It was observed that an increase in the number of torsion actuators resulted in increase in the torsion stiffness of rotor blade and the 'interference effect' which reduces the twist. However, reducing the number of actuators reduces the stiffness and increases the twist. Blade testing showed that structural stiffness of the blade decreased as the actuator spacing was increased.

The blade was tested in Glenn L. Martin Wind Tunnel at the University of Maryland. Dynamic tests were performed in non-rotating and rotating conditions. The twist achieved here being small, only partial reduction was possible. The maximum tip twist values at resonance frequencies (50Hz and 90 Hz) were 0.35° and 1.1° respectively. At non-resonance frequencies, the response was less than 0.5° at 4/rev excitation.

With the emergence of piezo fiber technology the active twist concept was dramatically improved. With this technology it is possible to create an active piezo ply within a composite laminate, enabling the smart structures vision of active elasticity. The continuous piezo ply is structural more effective than the embedded monolithic piezo elements. The piezo fiber concept was originally developed by Hagood et al. [7] and was commercialized. Active fiber composites (AFC) are integrated within a composite rotor blade to induce a twisting moment. AFC are active plies oriented at 45° to the blade span in order to induce shear stresses and a distributed twisting moment along the blade.

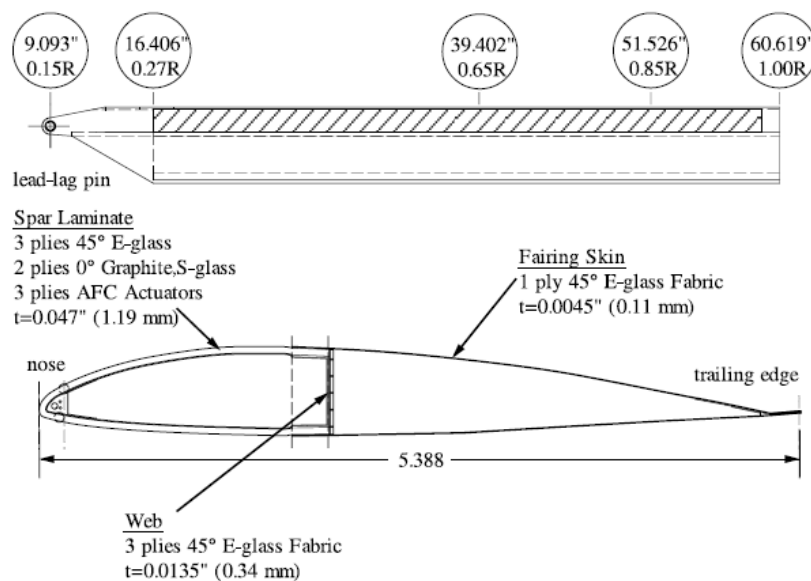


Figure 1.9. Schematic cross section of the complete CH-47D active blade section (Dimensions are in inches) [90]

Using this new actuator technology, Hagood et al. [32, 92, 89] built a 1/6th Mach scale CH-47D blade model for wind tunnel testing at Boeing Helicopters (Philadelphia) with incorporated AFC. The span of the blade was 60.619 in (153.97 cm) and the chord was 5.388 in (13.68 cm). Three diagonally placed AFC plies were incorporated in the co-cured D-spar blade lay-up (Figure 1.9).

Activation of the diagonally placed fibers induces shear in the spar skin, which generates blade twist. A design goal of $\pm 2^\circ$ blade twist was set. The blade specimen contained 7 groups of 6 AFC packs (3 in the top plies and 3 in the bottom). Of the 42 AFC packs installed in the blade, 11 were found to have poor electrical connection, and could not be activated. Thus, the blade actuation authority was somehow impaired. Bench tests performed at frequencies up to 67.5 Hz demonstrated a maximum twist authority of between 1° and 1.5° peak-to-peak ($\pm 0.5^\circ$ to $\pm 0.75^\circ$ amplitude). The full-length blade specimen was tested in a hover stand at 800 to 1336 rpm. The blade demonstrated hover testing resulted in recorded torsional strain and vertical hub force [91].

In 1999, a joint venture from NASA, Army and MIT built and tested an active twist rotor with a structural design similar to the Boeing model rotor. Once more, the twist is generated via AFC piezoelectric actuators embedded into the rotor blade spar [114, 115, 116].

A four-bladed, aeroelastically scaled, ATR model was designed and fabricated to be tested in the heavy gas (2.4 kg/m^3) medium of a transonic wind tunnel to achieve better Mach-scale similarity. AFCs were utilized in fabricating the rotor blades. Each ATR blade consisted of 24 AFC actuators to implement the active twist control (Figure 1.10). The AFC actuators are embedded directly in the structure of each blade D-spar, spanning from 0.30R (30% blade radius) to 0.98R (Figure 1.11).

The AFCs are placed in four layers through the thickness of the blades and are oriented such that the active strain is applied at $\pm 45^\circ$ relative the blade spanwise axis to permit

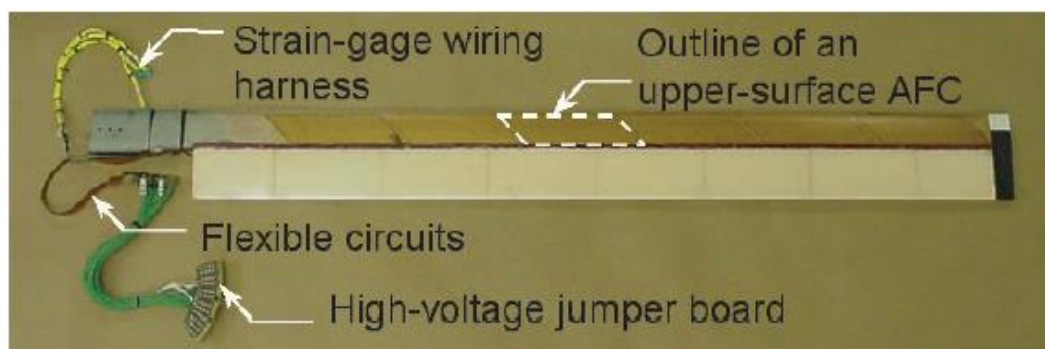


Figure 1.10. Final Active Twist Rotor prototype blade [17]

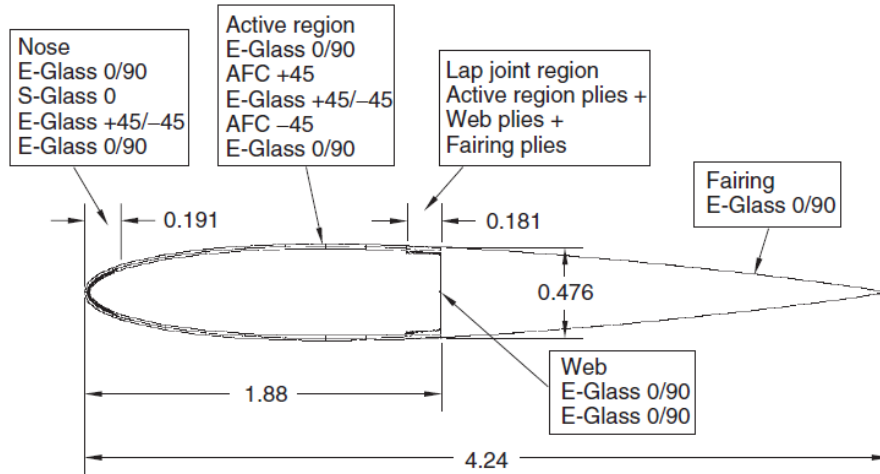


Figure 1.11. Schematic cross section of the final Active Twist Rotor scaled model blade section design (Dimensions are in inches) [17]

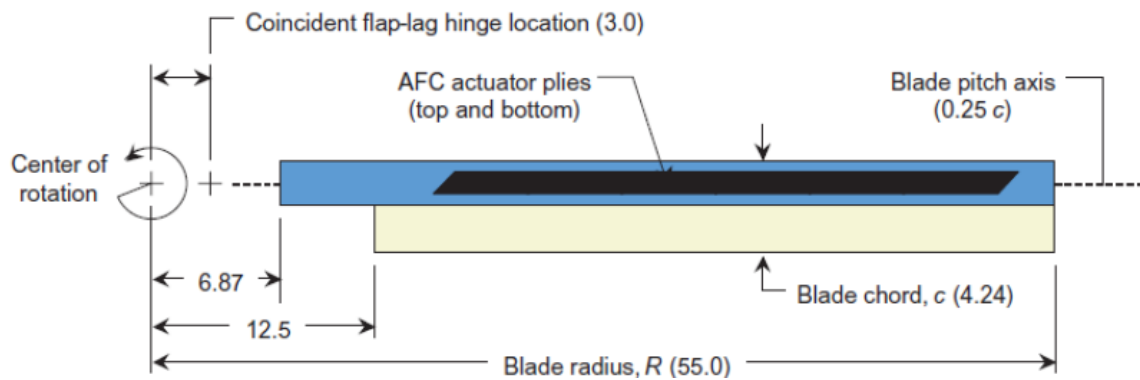


Figure 1.12. Active Twist Rotor scaled model blade geometry (Dimensions are in inches) [17]

maximum torsional control of the blades (Figure 1.12). They were actuated using separate high-voltage, low-current power channels for each blade. The pre-twist was linear with a twist of -10° from the center of rotation to the blade tip. NACA-0012 airfoil section was used. Hover testing was conducted to determine the basic frequency response characteristics of the ATR blades under active twist control.

For the non-rotating results, the blade was mounted on the bench in a single-cantilevered condition. Based on measured bending moment response, it was estimated that 1.1° to 1.4° maximum twist was generated for the $4 \pm 1/\text{rev}$ (33–55 Hz) frequency range at 1000 V electric excitation. Simulated forward flight experiments of an improved rotor will follow.

Cesnik et al. [16] further improved this technology and successfully tested a Mach-scaled rotor model with embedded active fibers in the Transonic Dynamics wind tunnel in both open-loop and closed-loop investigations.

In another paper, Cesnik et. al [17] investigated dynamic characteristics of active twist rotor blades analytically and experimentally. This paper presents a general framework to analyze and design active composite blades with distributed anisotropic piezoelectric strain actuators, investigates the frequency of an active twist rotor blade for both non-rotating and rotating conditions and then correlates the theoretical model with experiments on the bench and under hover conditions.

Shin et al. [99, 101] designed a vibration minimizing controller that implements a classical disturbance rejection algorithm with some modifications. The closed-loop controller was numerically simulated and the capability for hub vibratory load reduction was demonstrated.

They also refined analytical tools related to this rotor system. The results of a fully-articulated active blade model and its dynamic characterization under both non-rotating and rotating conditions were presented. The experimental test results showed 40db reduction in vertical shear vibratory loads and some reduction in other hub force and moment components.

Aeroelastic modelling of the ATR performance was performed by Wilkie et al. [119, 118]. Two aeroelastic modelling approaches were utilized to study piezoelectric active twist rotor systems. The first, PETRTA, utilizes a simplified mathematical model and is designed for use with the MATLAB numerical analysis package. The second employs the commercially available CAMRAD II code. Design cases used in the development of the NASA/Army/MIT ATR system were studied using both approaches. The results with both approaches are in consistently good agreement. The ATR prototype blade was originally expected to achieve static twist actuation amplitudes of between 2.0° to 2.5° , and hovering flight dynamic twist actuation amplitudes of 2.0° to 4.0° at an extended cycle of maximum applied voltage of 4000 Vpp/1200 Vdc.

In 2004, Boeing investigated the possibility of scaling the results of the Mach-scaled rotor to a full scale rotor blade [110]. The main focus of this investigation was laid on production and manufacturing approaches concerning the incorporation of the piezoelectric actuators and a robust and reliable wiring to provide the necessary power to the actuators. A 1.8 m CH-47D blade section with 24 layers of AFCs embedded in the spar laminate was build and successfully tested. It was shown that a full scale active twist blade with a meaningful actuation capability and acceptable natural frequencies can be built within the weight limit of a passive blade.

In parallel to Chen and Chopra, the German Aerospace Center (DLR) started to work with active twist rotor blades in the early 90th. While Chen and Chopra were using d_{31}

actuators the DLR decided to use the tension torsion coupling of helical windings within the rotor blade skin to generate the twist deformation.

The first demonstrator with this concept (AT0) was designed for non-rotating application only and showed a static peak-to-peak twist of $0.5^\circ/\text{m}$. Furthermore the actuation capabilities of this demonstrator under steady aerodynamical loads were shown in a non-rotating wind tunnel test.

During a Collaborative research within the European Integrated Project “Integration of Technologies in Support of a Passenger and Environmentally Friendly Helicopter” (FRIENDCOPTER), twist blades were investigated more intensively. A series of blades was built using thin skin integrated actuators.

At the first stage, several parameter studies for the optimisation of the skin lay-up were carried out [84, 81, 111]. The design philosophy was to find an optimum that considers the twist deflection that can be achieved with respect to the torsional rigidity. Then demonstrator blades were designed and manufactured [69, 83, 111].

The baseline of the blade characteristics were taken from the well-known BO-105 model rotor blade. The BO-105 blade features a C-Spar made of unidirectional glass fiber, a glass fiber skin and a foam core (Figure 1.13). The chord length of 121 mm and the radius of 2 m are in agreement with the original model rotor blade. The actuators that were used are Macro Fiber Composites (MFC), developed by NASA. These actuators are much more reliable than AFC actuators.

The first demonstrator built at DLR (Figure 1.14) is called AT1 and incorporated 2x11 standard MFCs with 45° fiber direction [112]. Based on this blade a second model rotor blade (AT2) was built [113].

The profile was changed into a symmetrical NACA 0012. To improve the performance, a good coverage with active material had to be realized. In addition to realize the desired actuation direction of 40° , special shaped MFC actuators were designed for the AT2 blade.

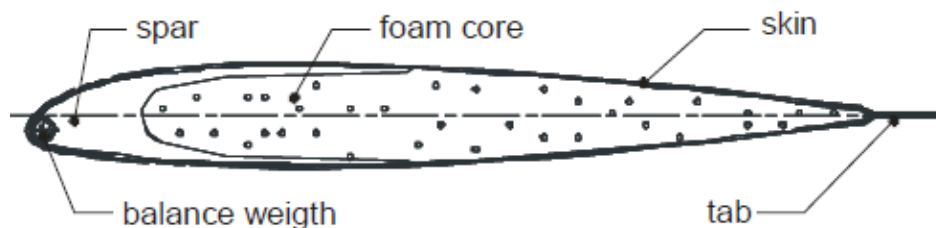


Figure 1.13. Schematic cross section of DLR active twist blade [111]



Figure 1.14. DLR Active Rotor Blades AT1 through AT5 (left to right) [111]

Two times six actuators were integrated into the rotor blade skins. The actuator orientation was chosen to be $+40^\circ$, whereas the skin was made of unidirectional glass fiber laminates with an orientation of -30° (inner skin). The area surrounding the actuators was provided with additional unidirectional glass fiber layers in a $+40^\circ$ direction (outer skin). The outer skin is used to carry the loads of the actuators and to decrease the change in stiffness in the transition region between skin and actuators. The anisotropy of the skin allows the actuators to work in a relatively soft direction (approximately perpendicular to the fibers of the inner skin), whereas the complete blade still keeps its torsional stiffness by the shear stiffness perpendicular to the actuators.

The blade AT3 shows a parabolic tip and varies the profile from NACA 23012 at the blade root to a high speed profile OA209 at the outer 10%. The skin consists of symmetrical glass layers of $\pm 45^\circ$.

The Blades AT4 and AT5 both show rectangular planform again. The airfoil is NACA23012 all the way from the root to the tip. A pre twist of $-4^\circ/\text{m}$ is inbuilt. The AT4 shows passive glass layer of $\pm 45^\circ$ and actuators of 45° . The AT5 is designed with a different design goal which is maximum twist without any considerations of the blade stiffness.

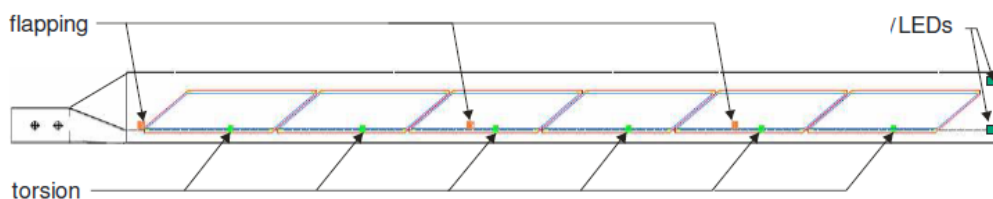


Figure 1.15. Sensor positions AT2 [111]

The testing under centrifugal loads was carried out in the DLR whirl tower. It is equipped with a test rig to spin the blades, but also includes many different types of measuring equipment. One of these is an optical method to measure the tip twist by taking pictures of the blade integrated LEDs as they pass the high speed camera [82, 113].

All blades were equipped with several sets of strain gauges. As an example, nine sets of strain gauges are implemented into the AT2. Six sets were implemented for measurement of torsion (one for each actuator) and 3 for flapping. The locations of the strain gauges are shown in Figure 1.15.

DLR presented the evidence that the active twist blades with MFCs can generate sufficient twist deformation under full centrifugal loads at different higher harmonic excitations. Figure 1.16 shows the peak-to-peak active tip twist that was derived during centrifugal testing at a nominal rotor speed of 1043 rpm. Comparing the static active twist with and without centrifugal loads is in Figure 1.17.

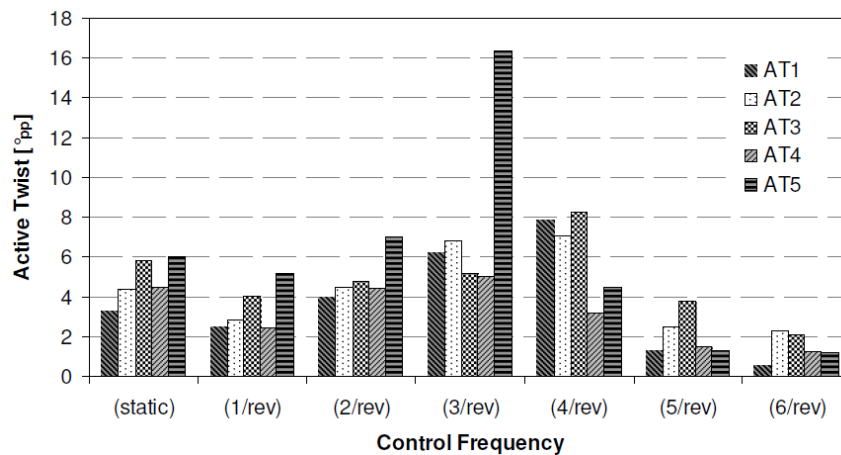


Figure 1.16. Maximum active tip twist (centrifugal testing, 1043rpm) [111]

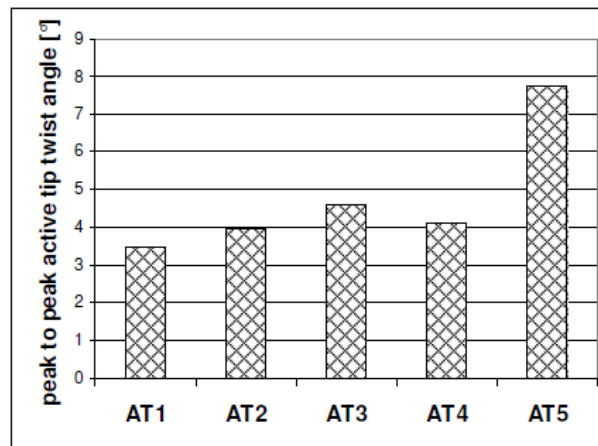


Figure 1.17. Quasi static active tip torsion angle (lab test) [111]

It can be noted that the blade can be designed in a way that the tip twist remains almost unchanged (AT1, AT2, AT4). For other designs, a decrease (AT5) or even increase (AT3) of the static active tip twist due to centrifugal effects, aerodynamics or differing boundary conditions is possible.

1.2.2. Numerical study of the Active Twist Rotor blades

The studies discussed until now were more focused towards experiments. Addressing this issue, some researchers discussed detailed modelling of smart composite rotors.

Chattopadhyay et. al [21] presented numerical results for a four-bladed bearingless model rotor with self-sensing piezoelectric actuators mounted at 45 degrees on the top and bottom walls of the composite box-beam blade. The composite box beam consisted of Graphite/epoxy in stacking sequence of $[-45/45]_{2s}$ in horizontal walls and $[45]_8$ in vertical walls. The box-beam dimensions were: length is 7.92 m, width is 0.18 m and height is 0.05 m. The thickness of PZT was 0.196 mm and the blade had a rectangular planform with a linear twist of -10 deg.

Firstly, a comprehensive analysis technique was developed for the analysis of rotor dynamic loads using a composite rotor blade built around an active box beam. Secondly, the model was used to investigate reduction in hub dynamic loads using closed-loop control. A higher order theory based approach was used to model the smart composite beam [22].

In this theory, higher order displacement field was developed to model the individual walls of arbitrary thickness, in the presence of eccentricity. The theory approximates the elasticity solution so that the beam cross-sectional properties are not reduced to one-dimensional beam parameters. It considers in-plane and out-of-plane warping. Because the relationships between the induced strain due to actuation and the applied electric field are nonlinear at high voltages, the formulation includes these nonlinear induced strain effects. For the rotor analysis, an unsteady aerodynamic model was coupled with a rotor blade dynamic model to develop an integrated rotor vibratory load analysis procedure. The rotor dynamic analysis accounted for deformations in the flap, lag and torsion directions. A finite-state induced flow model was used for predicting the aerodynamic loads. Parametric studies were also done to assess the influence of number and location of actuators on the vibratory load reduction at the hub.

In another set of important studies on smart composite rotors, Cesnik and Shin [14, 15] performed detailed modelling of the active twist rotors with AFCs. The analysis was based on

an asymptotic formulation for the two-cell thin-walled anisotropic active beam. This formulation stems from shell theory, and the displacement field (including out-of-plane warping) is not assumed a priori, but results from an asymptotical approach. It was observed in case of two celled box beams that increasing the stiffness in the active members always decreased the actuation. A two-cell model of the blade cross-section was developed, and relative stiffness parameter studies were performed to identify optimal configuration. The baseline configurations of the two box beams are depicted in Figure 1.18.

They found that there was a possibility of obtaining an increase in twist actuation in the two-cell model, on adding passive plies at the regions other than the active one. An important conclusion of the study was that the net change in twist actuation in the two-cell active beam depends on the local stiffness variation in the active or passive region. Conventional design belief, that torsional stiffness must be reduced to increase twist actuation was not found to be true. It was shown that torsional stiffness can be increased up to 20% with an increase in twist actuation of about 5%.

The authors mention that the single-cell cross-section model is incapable of capturing the interaction between active and non-active cross-sectional walls and hence is insufficient to predict the performance of multi-cell beams. Overall, the active model was found to be in good agreement with the experiments and therefore could be used to design and analyze future active helicopter blade systems.

Park and Shin [77, 98] presented the design of a novel integral twist actuated blade that uses single crystal piezoelectric fiber composites. These composites efficiently reduce the vibration and acoustic signal of helicopters. Figure 1.19 shows the cross-section of the designed Advanced Active Twist Rotor (AATR) blade using single crystal MFC actuators. The cross-section uses a NACA0012 airfoil and consists of the nose, active spar, web and fairing. In the active spar region, in order to maximize the twist actuation, the single crystal MFC plies should be oriented $\pm 45^\circ$ with respect to the blade axis.

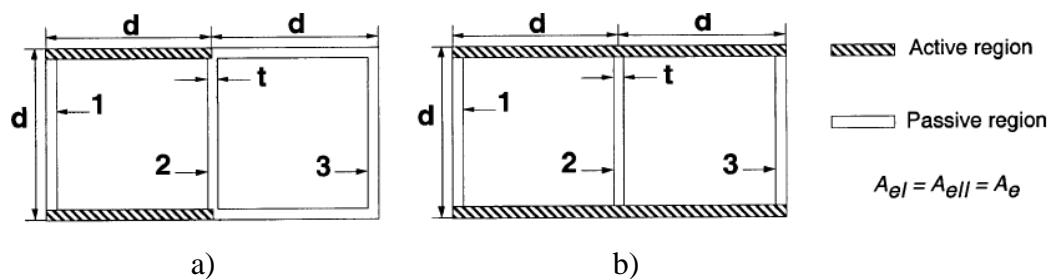


Figure 1.18. Baseline configurations of two-cell box beams: (a) asymmetric case; (b) symmetric case [14]

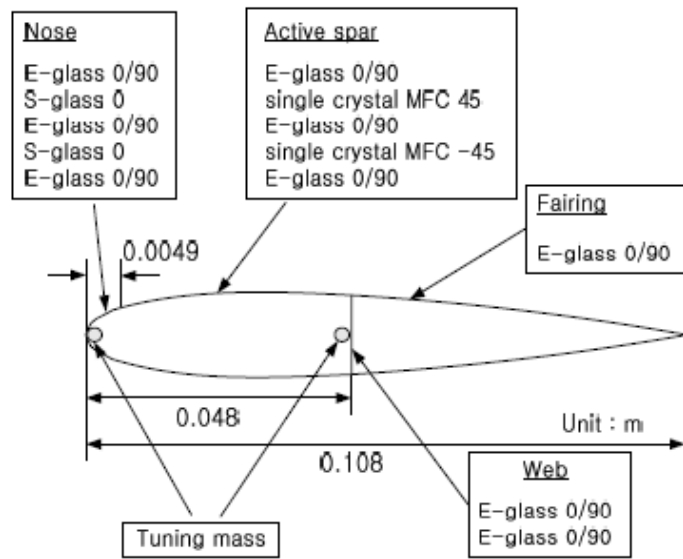


Figure 1.19. Cross-section of the Advanced Active Twist Rotor blade

The new ATR concept was known as the Advanced Active Twist Rotor (AATR) blade can reduce the vibration and acoustic signals of the helicopter more efficiently. However, much lower input-voltage and active region length are used compare with previous ATR blade concepts. Design and analysis of the blade structure consisted of a 2D cross-section analysis and 1D beam analysis. The cross-section modelled as a two-cell composite beam (Figure 1.20). The twist actuation frequency response of the AATR blade shows that the AATR blade can achieve higher twist actuation which is sufficient to alleviate the helicopter vibration although lower input voltage is used as compared with the ATR blades using the AFC and the standard MFC.

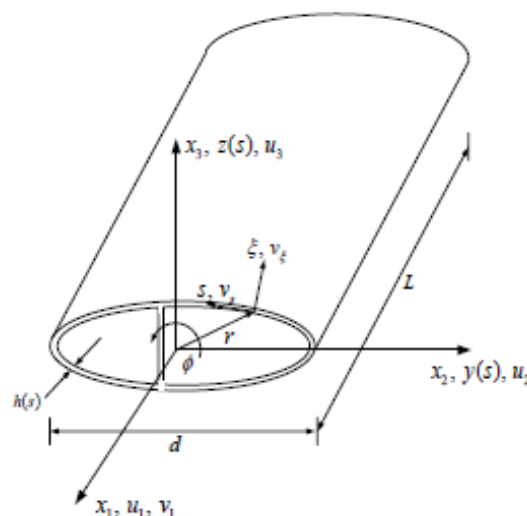


Figure 1.20. Two-cell thin-walled cross-section beam

In another study, Ghiringelli et. al [40] developed an analytical procedure for modelling of an active twist helicopter rotor using active fiber composites. The rotor blade was twisted using induced– strain actuators distributed into the structure of the blade. Active fiber components made of piezoelectric fibers actuated by inter digitated electrodes (IDE) was used. Fiberglass was used for the outer skin and also placed between the piezoelectric plies. Unidirectional graphite epoxy (T900) was used for the inner part of the spar. The elastic, inertial, and piezoelectric properties of the blade section were determined by a dedicated semi analytical formulation.

Buter and Breitback [11] investigated the active twist concept using an actively controlled tension–torsion–coupling of the structure at the DLR (German Aerospace Laboratory). Tension–torsion coupling is an anisotropic behaviour which appears in structural components. It can be realized by properly orienting the blade stiffness's. The anisotropic material behaviour has to be separated from the anisotropic structural behaviour resulting from structural elements like ribs or stringers. The actuator was integrated inside a composite helicopter rotor blade. The rotor blade was represented by a tension–torsion coupled thin–walled rectangular beam similar to the BOI05 model rotor with a scaling factor of 2.54.

The calculation of this beam is based on an extended Wlassow theory. A piezoelectric stack actuator was found to be suitable for twisting the blade and a deformation of $\pm 1.5^\circ$ was achieved. However, a disadvantage of the actuator was the high spanwise stiffness of the rotor blade spar. The adaptive twist was achieved using only the outer part of the blade resulting in a comparatively small control effect.

In the FRIENDCOPTER Project, a finite element analysis based procedure was used to determine the stiffness and piezoelectric properties of an active twist rotor blade [41]. The cross–sectional properties obtained were used in a multibody analysis of the active twist rotor to obtain vibration suppression by open and closed loop controls [40]. Pierangelo et. al [67] presents preliminary results about the design and optimisation of a model-scale active twist blade actuated by means of Macro Fiber Composites. The participating partners set up and performed some preliminary parametric studies and constrained optimisations of an innovative configuration for an active twist blade section.

Thornburgh et al. [67] performed parametric studies on model-scale blades in order to determine the variables critical for active twist response and to determine the effect of twist rate on cross-sectional constraints like mass per unit length, chordwise location of shear center, center of gravity and natural frequencies of blade and material stresses. They also looked at the effect of scaling changes on optimal structural design.

Brockmann and Lammering [10] derived a three dimensional beam finite element model with regard to all the gyroscopic terms and the actuation capabilities in a shear–flexible formulation with out-of-plane torsional warping. The results obtained were compared with analytical solution for the static case and results from the finite element shell model. The model showed good agreement with the finite element shell model except in the cases where deformation in the cross–sectional plane was observed since the beam formulation assumed undeformable shape.

Cesnik et al. [20] performed numerical parametric studies with UM/VABS for wing sections with double and triple cells to determine a cost effective way to add active material to the cross section.

Sekula and Wilbur conducted a series of parametric design studies with structural and aerodynamic parameters to understand the twist actuation in rotor blades [95, 96, 117]. In the parametric study with structural variables [96], the effect on blade active twist, rotor power required, blade loads and vibratory hub loads were studied due to the variation in blade torsional, flap-wise and lead-lag stiffnesses, sectional mass and torsional inertia, and center of gravity and elastic axis locations. The analysis was done using CAMARAD II [56] and the effect of actuators was represented by two torsion moments producing equal but opposing loads at the blade ends. In a similar study, the effect of aerodynamic parameters like linear blade twist, blade tip sweep, droop and taper on active twist performance was studied [95, 117]. Based on the analysis, a candidate design of AATR (Advance Active Twist Rotor) with –10 deg linear twist, 30 deg sweep, 10 deg droop and 2.5:1 taper ratio was proposed. In these studies, the external active twisting moment applied was assumed to be independent of the variation in blade structural and aerodynamic properties.

Blade–vortex interaction noise-generated by helicopter main rotor blades is one of the most severe noise problems and is very important both in military applications and community acceptance of rotorcraft. Some studies have addressed BVI noise using IBC concept. However, the only study addressing BVI noise using smart active twist rotor appears to be that by Chen et. al [25]. Noise reductions of 2-4 dB were predicted for strong, close blade vortex interactions and 7–10 dB for weaker interactions. However, they found that complete unsteady loading suppression was not possible with current technology due to large stroke and high frequency actuation required. The authors mention that the development of smart materials such as single crystal piezoceramics which have an order of magnitude of higher stroke capability than present day materials is likely to result in the capability to almost completely eliminate BVI noise. Furthermore, there is a need to develop actuator control

strategies based on open or closed loop pressure feedback which need to be investigated for realistic implementation.

More comprehensive and thorough reviews of trends of the active material actuation for the rotor blade control were steadily carried out at corresponding periods [42, 30, 28].

1.2.3. Active Twist Optimisation

This section provides literature review of active twist optimisation.

Sekula and Wilbur [94] studied the optimum blade tip planform for a model-scale active twist rotor. The analysis identified blade tip design traits which simultaneously reduce rotor power of an unactuated rotor while leveraging aeromechanical couplings to tailor the active response of the blade. Optimizing the blade tip planform for minimum rotor power in forward flight provided a 5% improvement in performance compared to a rectangular blade tip, but reduced the vibration control authority of active twist actuation by 75%. Optimizing for maximum blade twist response increased the vibration control authority by 50% compared to the rectangular blade tip, with little effect on performance. Combined response and power optimisation resulted in a blade tip design which provided similar vibration control authority to the rectangular blade tip, but with a 3.4% improvement in rotor performance in forward flight.

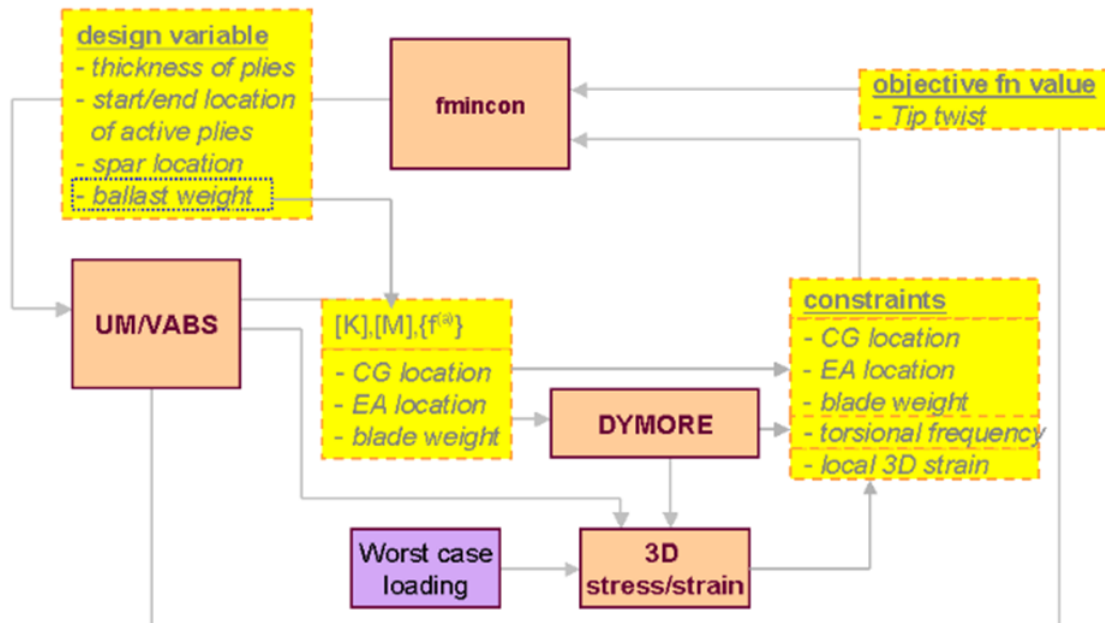


Figure 1.21. Flow chart of the design optimisation framework for active twist rotor blades

Cesnik and co-workers [19, 18] developed an optimisation framework to design an active blade that maximizes the static twist actuation while satisfying constraints on various blade requirements. The framework included UM/VABS for active cross section analysis, DYMORE for one dimensional geometrically exact beam analysis, a based cross-sectional parametric mesh generator and MATLAB's gradient based optimizer (Figure 1.21).

Results showed that the Active Twist Rotor (ATR) blade [100] could exhibit 30% higher twist actuation than the tested one. The same framework was used to design the ATR-A blade for tests in NASA's Transonic Dynamics Tunnel. The ATR-A was based on a scaled model of AH-60D blade that has a more complex geometry and the final design obtained included manufacturing constraints.

Park et al. [78] presented design optimisation of a new ATR blade with single crystal piezoelectric fiber composites. In order to design the new ATR blade a design optimisation developed for an active helicopter blade. The framework included 2D cross-sectional analysis, the 1D beam analysis, the gradient-based optimizer and various related modules. They proposed a new Advanced ATR blade (the AATR-II blade with improved twist actuation performance) that reduces vibratory loads in forward flight using much lower input-voltage. The AATR-II blade requires only 10% the input-voltage of the ATR design.

In the FRIENDCOPTER project [67], the objective was to maximize the twist per unit span of a uniform beam section under given constraints on airfoil shape, chordwise location of center of gravity and shear center, torsional frequency and beam stiffness. The design variables used were chordwise location, length and thicknesses of piezoelectric layers, ballast mass and four parameters that define the front C-spar.

Kumar [65] presented a new strategy and the corresponding framework for the optimum design of active twist rotor blades. The optimisation problem in the framework is solved using a surrogate-based approach in which the "true" objective function and constraints are replaced with computationally efficient functional relationships. The surrogate-based optimisation problem is solved in combination with the Efficient Global Optimisation (EGO) algorithm which accounts for uncertainty in surrogate predictions. To demonstrate the capability of the framework, three different optimisation problems were considered, namely, (a) maximizing static active twist per unit length, (b) maximizing amplitude of dynamic active twist at the blade tip at a fixed actuation frequency, and (c) maximizing dynamic twist at a range of actuation frequencies.

1.3. Thesis objectives

The main objective of the present thesis is the development of new modelling and optimisation methodology for the design of a rotor blade with an active twist to enhance its capability for vibration and noise reduction. This methodology is based on the new 3D finite element model, planning of experiments and response surface technique to obtain high piezoelectric actuation forces and displacements with the minimal actuator weight and energy applied.

The thesis objectives are achieved by solving the following problems:

- Development of the realistic 3D finite element models of the helicopter rotor blades in model-scale and full-scale for their analysis and optimal design.
- Parametric studies of the rotor blades with C- and D- spars in order to determine the influences of the cross-sectional design parameters on the active twist and study the dependence of the behaviour functions on the design parameters.
- Solution of optimisation problem for the model scale rotor blades with C- and D- spars and with two possible applications of the piezoelectric actuators.
- Development of the Design Tool for the optimum placement of Macro Fiber Composite actuators in the helicopter rotor blades.
- Solution of optimisation problem for the full scale rotor blade with C- spar and two possible applications of the piezoelectric actuators.

1.4. Structure of thesis

This thesis consists of seven chapters, which are organized as follows:

Chapter 1 provides the literature review on the vibration and noise reduction in helicopters with actively controlled twist blades.

Chapter 2 describes the structure of helicopter rotor blades with C- and D- spars in model scale and full scales rotor blade. The dimensions and material properties of these blades are presented.

Chapter 3 presents the finite element modelling and numerical parametric study of the rotor blades with C- and D- spars. Parametric study is used to formulate an optimisation problem.

Chapter 4 describes an optimisation methodology, based on the planning of experiments and response surface technique for the design of new rotor blade with MFC

actuators. The mathematical statement of the optimisation problem is presented and each component of the methodology is described in details.

Chapter 5 presents the optimisation results for the model scale rotor blades with C- and D- spars and two possible applications of the piezoelectric actuators. Torsion angle obtained from the finite element simulation of helicopter rotor blade is compared with the experimental value to confirm the modelling accuracy. The Design Tool was produced for the optimum placement of Macro Fibre Composite actuators in the helicopter rotor blades.

Chapter 6 presents the optimisation results for the full scale rotor blade and two possible applications of the piezoelectric actuators. Before optimal design solution of full scale rotor blade the numerical upscaling problem is investigated.

Finally, the research efforts and achievements in this thesis are summarized in the **Chapter 7**.

2. STRUCTURE OF HELICOPTER ROTOR BLADES

The structure of helicopter rotor blades with C- and D- spars in model scale and full scale rotor blade with C-spar is described in this chapter. The model scale BO105 helicopter rotor blade with C-spar is used as the baseline case. The dimensions and material properties of these blades are presented.

2.1. Model scale rotor blades

The dimensions and material properties of the rotor blade in the model scale with two spar configurations are given in this section.

2.1.1. Rotor blade with C-spar

The baseline configuration was taken from the well-known passive BO105 model scale rotor blade, since the baseline (passive) rotor blade was well-studied and characterized over the years. The investigated BO105 model rotor blade presented in Figure 2.1 consists of C-spar made of unidirectional Glass Fibre Reinforced Polymer (GFRP), skin made of $\pm 45^\circ$ GFRP, Macro Fibre Composite (MFC) actuators embedded into the skin, foam core and balance weight. The thickness of GFRP skin is $t=0.25 \times n$, where n is the number of layers, and thickness of MFC actuators is 0.3 mm. MFC actuator consists of rectangular piezoceramic fibres embedded in an epoxy matrix and sandwiched between polyamide films that has attached interdigitated electrode patterns as shown in Figure 2.2. The direction of piezoceramic fibres in MFC actuators coincides with the direction of the outside GFRP skin layers to maximize the twist actuation capabilities of the active plies on the top and bottom of

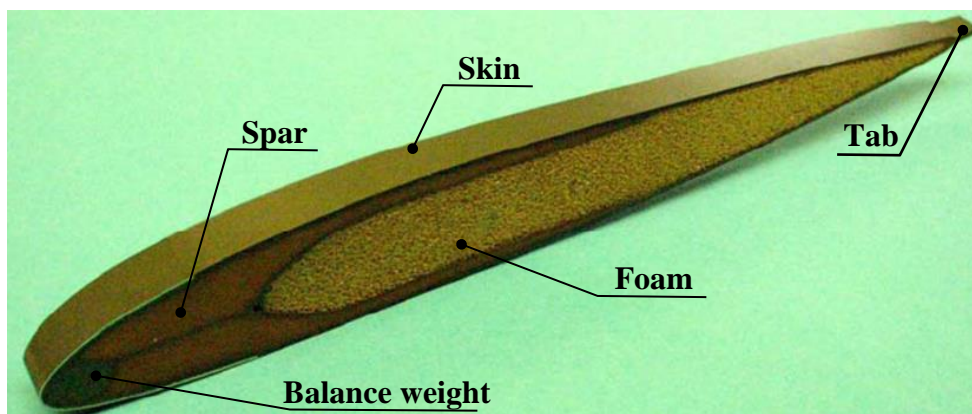


Figure 2.1. Cross-section of the BO105 model scale rotor blade

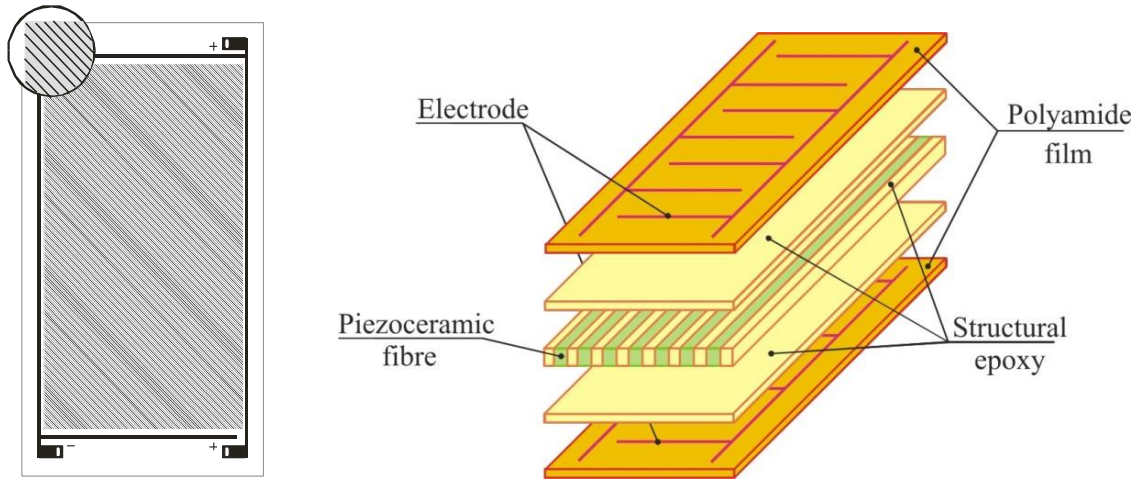


Figure 2.2. Macro Fibre Composite actuator

rotor blade.

Figure 2.3 shows a baseline rotor blade planform and cross-section dimensions. This model is equipped with NACA23012 airfoil and has a rectangular shape with active part length 1.56 m and chord length 0.121 m. The blade is not pretwisted and the radius of this rotor is 2 m. The general dimensions and characteristics of this baseline blade are listed in Table 2.1. The material properties of the rotor blade and MFC actuator are given in Tables 2.2, 2.3, 2.4.

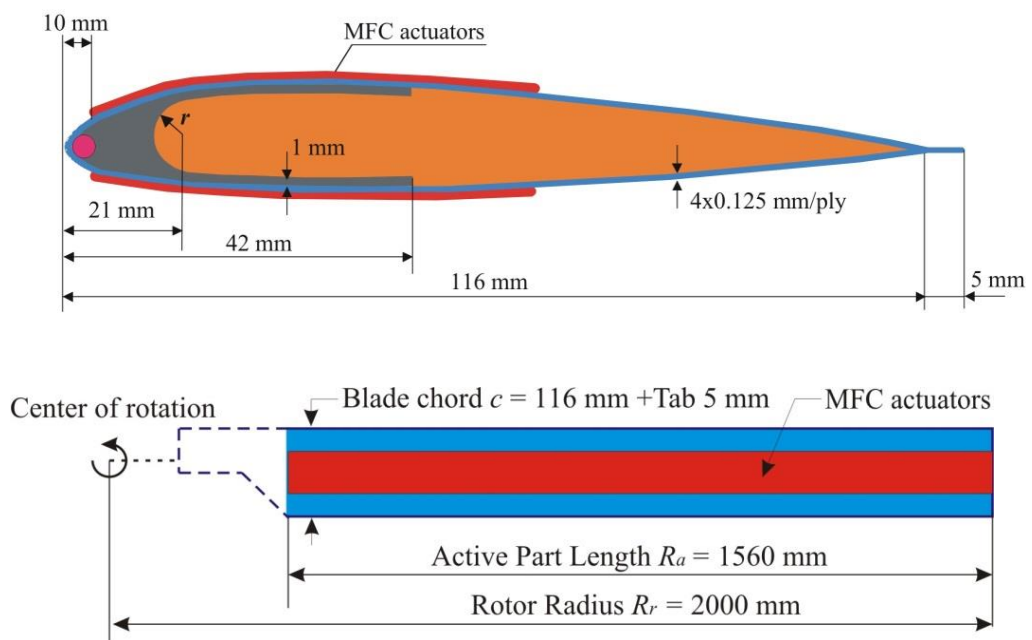


Figure 2.3. Cross-section and planform of the model scale rotor blade with C-spar

Table 2.1.

Characteristics of the BO105 model scale rotor blade [2]

| Title | Symbol | Units | |
|----------------------------|----------|--------------------|-----------|
| Airfoil section | – | – | NACA23012 |
| Rotor radius | R_r | [m] | 2.00 |
| Active part length | R_a | [m] | 1.56 |
| Profile thickness | – | [%] | 12 |
| Rotor blade chord | c | [m] | 0.121 |
| Centre of gravity location | y_{cg} | [% c] | 25.1 |
| Elastic axis location | y_{ea} | [% c] | 20.6 |
| Mass per unit span length | m | [kg/m] | 0.95 |
| First torsional frequency | f_{T1} | [Hz] | 67.9 |
| Flap bending stiffness | EI | [Nm ²] | 250 |
| Torsion stiffness | GJ | [Nm ²] | 160 |

Table 2.2.

Material properties: Glass Fibre Reinforced Polymer

| | Symbol | Units | Unidirectional GFRP |
|-----------------|-----------------------|----------------------|---------------------|
| Young's modulus | E_x | [GPa] | 45.166 |
| Young's modulus | $E_y = E_z$ | [GPa] | 11.981 |
| Shear modulus | G_{yz} | [GPa] | 1.289 |
| Shear modulus | $G_{xy} = G_{xz}$ | [GPa] | 4.583 |
| Poisson's ratio | ν_{yz} | – | 0.325 |
| Poisson's ratio | $\nu_{xy} = \nu_{xz}$ | – | 0.238 |
| Density | ρ | [kg/m ³] | 2008 |

Table 2.3.

Material properties: foam and balance weight

| | Symbol | Units | Foam Rohacell 51FX | Lead |
|-----------------|--------|----------------------|--------------------|-------|
| Young's modulus | E | [GPa] | 0.035 | 13.79 |
| Shear modulus | G | [GPa] | 0.014 | 2.00 |
| Poisson's ratio | ν | – | 0.25 | 0.44 |
| Density | ρ | [kg/m ³] | 52 | 11300 |

Table 2.4.

Material properties: Macro Fibre Composite actuator

| | Symbol | Units | Macro Fibre Composite |
|-------------------------------|-----------------------|----------------------|-----------------------|
| Young's modulus | E_x | [GPa] | 30.0 |
| Young's modulus | $E_y = E_z$ | [GPa] | 15.05 |
| Shear modulus | G_{yz} | [GPa] | 5.7 |
| Shear modulus | $G_{xy} = G_{xz}$ | [GPa] | 10.7 |
| Poisson's ratio | ν_{yz} | – | 0.35 |
| Poisson's ratio | $\nu_{xy} = \nu_{xz}$ | – | 0.44 |
| Density | ρ | [kg/m ³] | 4700 |
| Piezoelectric charge constant | d_{33} | [m/V] | $4.18 \cdot 10^{-10}$ |
| Piezoelectric charge constant | $d_{31} = d_{32}$ | [m/V] | $1.98 \cdot 10^{-10}$ |

2.1.2. Rotor blade with D-spar

The model scale rotor blade with D-spar was additionally chosen for the comparative study and optimisation. D-spar is a rotor blade cross-section that is hollow in nature with a single vertical spar (web) used to carry a large portion of the stresses otherwise carried by the skin. The cross-section dimensions of the rotor blade with D-spar are shown in Figure 2.4. The blade is based on the existing baseline BO105 model scale rotor blade. The web in D-spar is a continuation of the spar 'moustaches' in C-spar. It is made from unidirectional GFRP and has substantially the same thickness as the spar 'moustaches'.

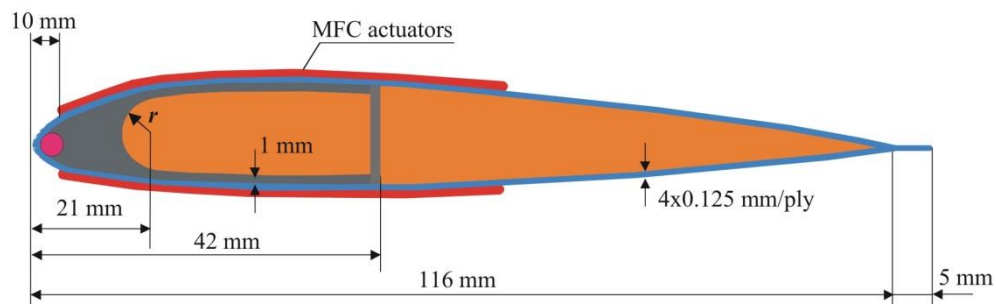


Figure 2.4. Cross-section of the model scale rotor blade with D-spar

2.2. Full scale rotor blade

The full scale rotor blade with C-spar is chosen as an actual rotor blade to demonstrate the active twisting actuation performance using MFC actuators. In real construction, this full scale rotor blade is based on the passive BO105 model scale rotor blade with C-spar and equipped with NACA23012 airfoils. The cross-section parameters of the model scale rotor blade are multiplied by the scale factor 2.67. The chord length of 310 mm is in agreement with the original full scale rotor blade.

Figure 2.5 shows the basic blade planform and cross-section dimensions selected for the full scale rotor blade. The general dimensions and characteristics of the full scale rotor blade are listed in Table 2.5.

In compare with the model scale rotor blades the full scale rotor blade structure includes a composite blade root. This root is made of unidirectional GFRP and is a continuation of the C-spar. The stiffness properties of the rotor blade root are given in Table 2.6. The material properties of the rotor blade and MFC actuator are given in Tables 2.2, 2.3, 2.4.

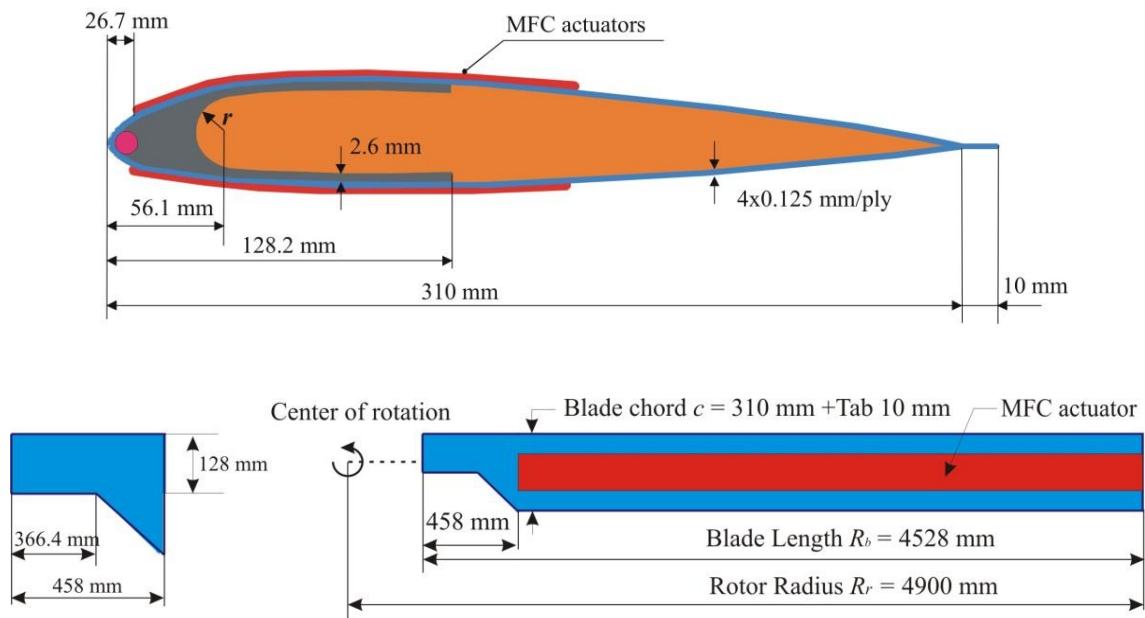


Figure 2.5. Cross-section and planform of the full scale rotor blade with C-spar

Table 2.5.

Characteristic of the full scale rotor blade [2]

| Title | Symbol | Units | |
|---------------------------------|----------|--------------------|------------|
| Airfoil section | – | – | NACA23012 |
| Rotor radius | R | [m] | 4.9 |
| Blade length | R_b | [m] | 4.528 |
| Active part length | R_a | [m] | 4.070 |
| Profile thickness | – | [%] | 12.0 |
| Rotor blade chord | c | [mm] | 310+Tab 10 |
| Centre of gravity location | y_{cg} | [% c] | 23.0 |
| Elastic axis location | y_{ea} | [% c] | 12.0 |
| Blade mass per unit span length | m | [kg/m] | 5.3 |
| Flap bending stiffness | EI | [Nm ²] | 12000 |
| Torsion stiffness | GJ | [Nm ²] | 7000 |

Table 2.6.

Stiffness properties: root of the full scale rotor blade

| Title | Symbol | Units | Baseline blade root |
|------------------------|-------------|--------------------|---------------------|
| Lead lag stiffness | EI_{lag} | [Nm ²] | 86000 |
| Flap bending stiffness | EI_{flap} | [Nm ²] | 8600 |
| Torsion stiffness | GJ | [Nm ²] | 8700 |

3. FINITE ELEMENT SIMULATION OF HELICOPTER ROTOR BLADES

This chapter presents the finite element modelling and numerical parametric studies of the rotor blades with C- and D- spars. 3D finite element models are developed by commercial finite element software ANSYS 11.0. Influence of the possible design parameters (spar geometry, skin lay-up, position and size of actuators) on the active twist is studied in detail.

3.1. Finite element model

3D finite element model of the rotor blade (Figure 3.1) is produced using commercial finite element software ANSYS, where rotor blade skin and spar “moustaches” are modelled by the linear layered structural shell elements SHELL99, whereas spar and foam by 3D 20 node structural solid elements SOLID186. Some model simplifications were done, namely foam material was removed from the rotor blade tail. This gives the possibility to decrease the dimension of the finite element model and to preserve a proportional mesh for the blade skin without accuracy loss for the results obtained. It is necessary to note that node offset option is applied for the joint skin-spar “moustaches” structure to preserve the rotor blade profile. In this case, the finite element nodes are located at the top surface. Balance weight was modelled by volume element. The web of D-spar is modelled by SHELL 99 element. The MFC

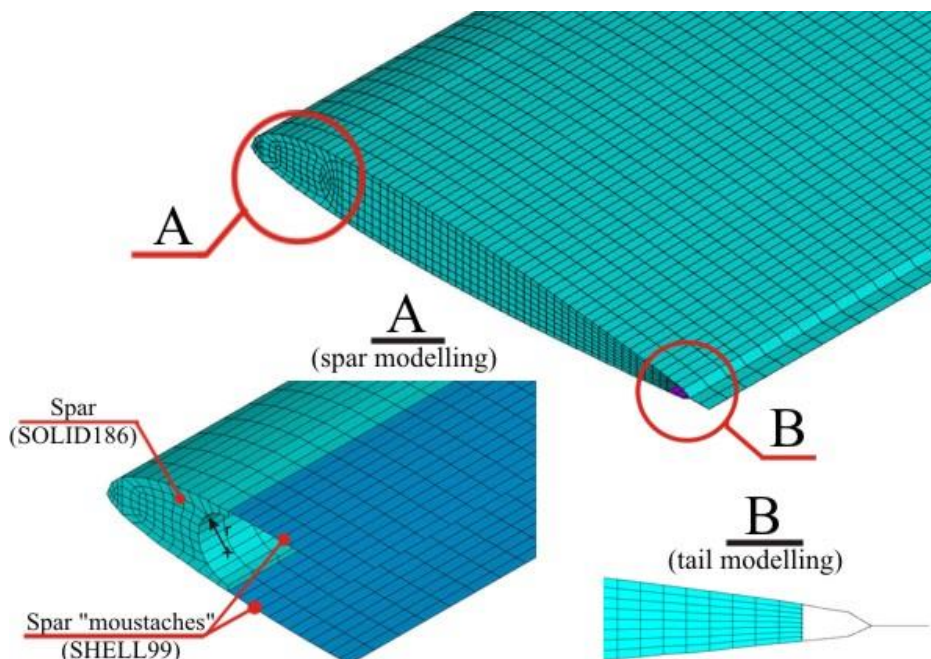


Figure 3.1. 3D finite element model of the rotor blade

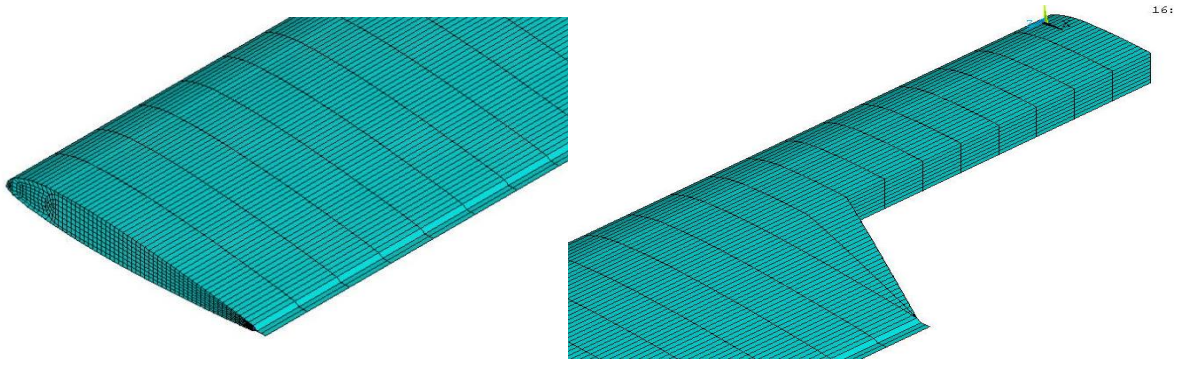


Figure 3.2. Finite element model of the full scale rotor blade with root

actuators are modelled by shell elements SHELL99 and embedded as an additional layer in the skin. The adhesive layer between MFC actuators and skin is ignored.

Difference between model scale and full scale blades is a root in the full scale rotor blade. The root is modelled by the linear layered structural shell elements SHELL99 (Figure 3.2). The finite element model was constrained at the one side of the blade with a clamped boundary condition. The clamped condition was realized by putting the constraints on nodes, when all DOF's (degrees of freedom) are fixed.

3.2. Finite element analysis

This section presents a description of the structural static analysis with thermal load, static torsion analysis and modal analysis using 3D finite element model of the rotor blade with MFC actuators.

3.2.1. Thermal analogy

Piezoelectric behaviour is characterised by the coupling of mechanical and electric fields, which is a natural property of the materials such as quartz and ceramics. Applying a voltage to a piezoelectric material creates a displacement, while vibrating of a piezoelectric material generates a voltage.

In the linear piezoelectricity, the equations of elasticity are coupled to the charge equation of electrostatics by means of piezoelectric constants (IEEE Standard on Piezoelectricity [49])

$$\{\sigma\} = [c^E]\{\varepsilon\} - [e]^T \{E\} \quad (3.1)$$

$$\{D\} = [e]\{\varepsilon\} + [\varepsilon^\varepsilon]\{E\} \quad (3.2)$$

or equivalently

$$\begin{Bmatrix} \{\sigma\} \\ \{D\} \end{Bmatrix} = \begin{bmatrix} [c^E] & [e] \\ [e]^T & -[\varepsilon^\varepsilon] \end{bmatrix} \begin{Bmatrix} \{\varepsilon\} \\ \{E\} \end{Bmatrix} \quad (3.3)$$

where: $\{\sigma\}$ is the stress vector, $\{D\}$ is the electric flux density vector, $\{\varepsilon\}$ is the strain vector, $\{E\}$ is the electric field intensity vector, $[E]$ is the elasticity matrix, $[e]$ is the piezoelectric stress matrix, $[\varepsilon]$ is the dielectric matrix. The superscripts E and ε denote that the respective constants are evaluated at constant electric field and constant stress. Equation 3.1 is the actuator equation and Equation 3.2 is the sensor equation, respectively.

The elasticity matrix $[c]$ can be given directly in uninverted form $[c]$ or in inverted form $[c]^{-1}$ as a general anisotropic symmetric matrix

$$[c] = \begin{bmatrix} c_{11} & c_{12} & c_{13} & c_{14} & c_{15} & c_{16} \\ & c_{22} & c_{23} & c_{24} & c_{25} & c_{26} \\ & & c_{33} & c_{34} & c_{35} & c_{36} \\ & & & c_{44} & c_{45} & c_{46} \\ & & & & c_{55} & c_{56} \\ & & & & & c_{66} \end{bmatrix} \quad (3.4)$$

symmetric

The piezoelectric stress matrix $[e]$ relates the electric field vector $\{E\}$ in the order x, y, z to the stress vector $\{\sigma\}$ in the order x, y, z, xy, yz, xz and is of the form

$$e = \begin{bmatrix} e_{11} & e_{12} & e_{13} \\ e_{21} & e_{22} & e_{23} \\ e_{31} & e_{32} & e_{33} \\ e_{41} & e_{42} & e_{43} \\ e_{51} & e_{52} & e_{53} \\ e_{61} & e_{62} & e_{63} \end{bmatrix} \quad (3.5)$$

The dielectric matrix $[\varepsilon^\varepsilon]$ uses the electrical permittivities and can be described in orthotropic or anisotropic form

$$[\varepsilon] = \begin{bmatrix} \varepsilon_{11} & 0 & 0 \\ 0 & \varepsilon_{22} & 0 \\ 0 & 0 & \varepsilon_{33} \end{bmatrix} \text{ or } [\varepsilon] = \begin{bmatrix} \varepsilon_{11} & \varepsilon_{12} & \varepsilon_{13} \\ & \varepsilon_{22} & \varepsilon_{23} \\ \text{symmetric} & & \varepsilon_{33} \end{bmatrix} \quad (3.6)$$

The finite element discretization is performed by establishing the nodal solution variables and the element shape functions over an element domain which approximates the solution.

$$\{u_c\} = [N^u]^T \{u\} \quad (3.7)$$

$$V_c = \{N^v\}^T \{V\} \quad (3.8)$$

where: $\{u_c\}$ is the displacement within element domain in the x, y, z directions, $\{u\}$ is the vector of nodal displacement, $[N^u]$ is the matrix of displacement shape functions, $\{N^v\}$ is the vector of electrical potential shape function, $\{V\}$ is the vector of nodal electrical potential, V_c the is electrical potential within element domain.

Then, the strain ε and electric field E are related to the displacements and potentials, respectively, as

$$\{\varepsilon\} = [B_u] \{u\} \quad (3.9)$$

$$\{E\} = -[B_v] \{V\} \quad (3.10)$$

$$[B_u] = \begin{bmatrix} \frac{\partial}{\partial x} & 0 & 0 & \frac{\partial}{\partial y} & 0 & \frac{\partial}{\partial z} \\ 0 & \frac{\partial}{\partial y} & 0 & \frac{\partial}{\partial x} & \frac{\partial}{\partial z} & 0 \\ & & \frac{\partial}{\partial z} & & \frac{\partial}{\partial y} & \frac{\partial}{\partial x} \end{bmatrix}^T \quad (3.11)$$

$$[B_v] = \begin{bmatrix} \frac{\partial}{\partial x} & \frac{\partial}{\partial y} & \frac{\partial}{\partial z} \end{bmatrix}^T \{N^v\} \quad (3.12)$$

After the application of the variational principle and finite element discretisation [1], the coupled finite element matrix equation is

$$\begin{bmatrix} [M] & [0] \\ [0] & [0] \end{bmatrix} \begin{Bmatrix} \ddot{\mathbf{u}} \\ \dot{\mathbf{V}} \end{Bmatrix} + \begin{bmatrix} [C] & [0] \\ [0] & [C^{vh}] \end{bmatrix} \begin{Bmatrix} \dot{\mathbf{u}} \\ \dot{\mathbf{V}} \end{Bmatrix} + \begin{bmatrix} [K] & [K^z] \\ [K^z]^T & [K^d] \end{bmatrix} \begin{Bmatrix} \mathbf{u} \\ \mathbf{V} \end{Bmatrix} = \begin{Bmatrix} \{F_u\} \\ \{F_v\} \end{Bmatrix} \quad (3.13)$$

where: $[K]$ is the element stiffness matrix, $[M]$ is the element mass matrix, $[C]$ is the element structural damping matrix, $[C^{vh}]$ is the element dielectric damping matrix, $[K_d]$ is the element dielectric permittivity coefficient matrix, $[K_z]$ is the piezoelectric coupling matrix, $\{F_u\}$ is the vector of nodal, surface and body charges, $\{F_v\}$ is the applied nodal charge vector. This equation clearly shows the coupling of displacement and electric fields.

For static type situation, the equation is

$$\begin{bmatrix} [K] & [K^z] \\ [K^z]^T & [K^d] \end{bmatrix} \begin{Bmatrix} \mathbf{u} \\ \mathbf{V} \end{Bmatrix} = \begin{Bmatrix} \{F_u\} \\ \{F_v\} \end{Bmatrix} \quad (3.14)$$

In practice, voltage may also be specified as an input to the actuators. In this case the following equilibrium equation, for static type situation, can be written as:

$$K \cdot u = F_u - F_{act} \quad (3.15)$$

where $F_{act} = K_z V$ is an additional force vector due to the voltage V applied to the actuators.

To perform finite element analysis, involving piezoelectric effects, the coupled field elements that take into account mechanical and electrical coupling are required. These coupled field elements should contain all the necessary nodal degrees of freedom for the electrical-mechanical coupling. In a simple coupled field element, there are four DOF at each node, three displacement components u_i ($i=1,2,3$) and voltage V .

Nowadays, the commercial finite element software ANSYS [4] is equipped with 3D and 2D solid elements allowing to model piezoelectric effect. In the finite element models with these elements the piezoelectricity matrix, the electrical permittivity matrix and the anisotropic stiffness matrix are specified as the material properties. Another approach to activate piezoelectric effect within ANSYS is thermal analogy.

Thermal analogy between piezoelectric strains and thermally induced strains is used

to model piezoelectric effects when piezoelectric coefficients characterising an actuator are introduced as the thermal expansion coefficients. Preliminary work was done to demonstrate results in the use of the thermal analogy to model the static and dynamic behaviour of the simple piezoelectric structures [60–63].

Development of the analogy begins with the constitutive equation for the converse piezoelectric effect (Equation 3.1). The piezoelectric stress matrix can be obtained as follows

$$[e]^T = [c^E][d]^T \quad (3.16)$$

where $[d]$ is the piezoelectric strain coefficient matrix. The Equation 3.1 can be written as

$$\{\sigma\} = [c^E]\{\varepsilon\} - [c^E][d]^T\{E\} = [c^E](\{\varepsilon\} - [d]^T\{E\}) \quad (3.17)$$

Taking into account the thermal effect, the generalized Hooke's Law equation, can be written as follows

$$\{\sigma\} = [c^E]\{\varepsilon\} - [c^E]\{\alpha\}\Delta T = [c^E](\{\varepsilon\} - \{\alpha\}\Delta T) \quad (3.18)$$

where $\{\alpha\}$ is the thermal expansion coefficient vector and ΔT is the temperature difference.

Comparing Equation 3.17 with Equation 3.18, piezoelectric and thermal strains relationship is obtained

$$\varepsilon_{voltage} = \varepsilon_{thermal} \quad (3.19)$$

$$[d]^T\{E\} = \{\alpha\}\Delta T \quad (3.20)$$

The electric field E between electrodes is given by equation

$$E = \frac{\Delta V}{\Delta_{el}} \quad (3.21)$$

where ΔV is the voltage difference between the electrodes and Δ_{el} is the effective electrode

spacing (Figure 3.4). Equation 3.20 can be rewritten as

$$[d]^T \frac{\Delta V}{\Delta_{el}} = \{\alpha\} \Delta T \quad (3.22)$$

By setting $\Delta T = \Delta V$, the desired changes in voltage for the piezoelectric elements can be directly input into the FEM code via the thermal analogy as changes in temperature. As a result, the equality may be rewritten and simplified to

$$\alpha_{3i} = \frac{d_{3i}}{\Delta_{el}} \quad (i=1,2,3) \quad (3.23)$$

where the piezoelectric strain coefficient d_{3i} characterises the electromechanical properties of the piezoelectric material and describes the deformation of the material depending on the orientation of the electric field. The first subscript denotes the direction of the electric field and the second subscript denotes the direction of the deformation.

The knowledge of the three piezoelectric strain coefficients d_{31} , d_{32} and d_{33} is sufficient to fully characterize the electromechanical properties of the piezoelectric material. When an electric field E_3 is applied in the poling direction, an extension along the same direction occurs where its amplitude is governed by the piezoelectric coefficient d_{33} . This effect is called the d_{33} effect (Figure 3.3). Moreover, because of the applied electric field,

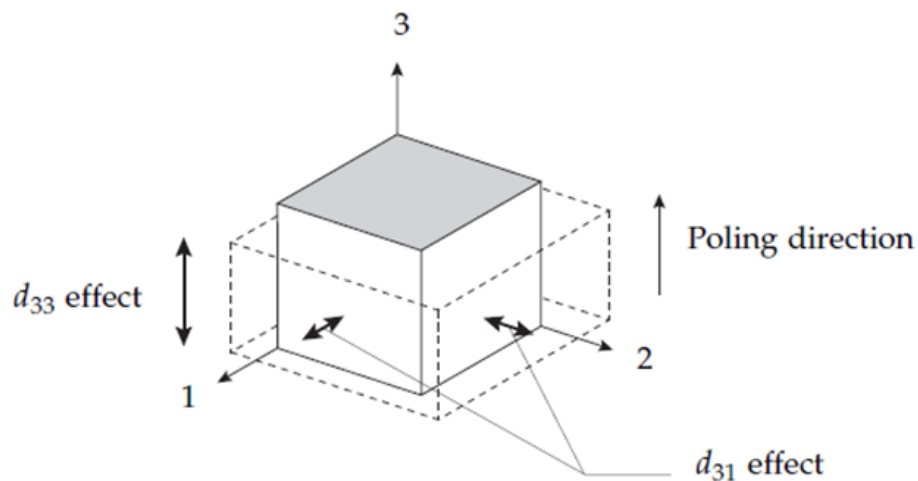


Figure 3.3. Piezoelectric material main deformation [[12]]

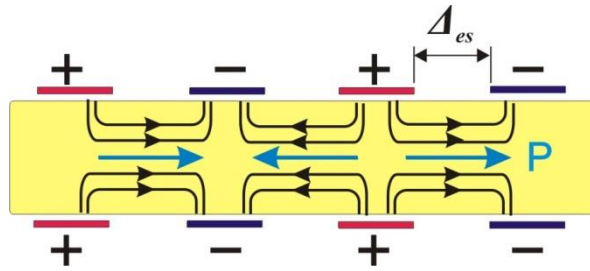


Figure 3.4. Cross-sectional view of electric field in the fibre of MFC actuator

shrinkage is observed along the directions 1 and 2 perpendicular the electric field, the amplitude of which is controlled by d_{31} and d_{32} respectively (by d_{31} and d_{32} have negative values). Piezoceramic has an isotropic behaviour in the directions 1 and 2, hence $d_{31} = d_{32}$. A deformation along the 1- and 2-axes, which is characterised by the d_{31} coefficient, is called the d_{31} effect.

The interdigitated electrodes of MFC actuator are placed perpendicular to the fibers and deliver the electric field required to activate the piezoelectric effect in the fibres as seen in Figure 3.4. The poling of fibres (P) and in-plane voltage actuation allows creating the d_{33} piezoelectric effect, which is stronger than the d_{31} effect used by the traditional piezoelectric actuators with poling and voltage actuation through the thickness [47].

By using the actual piezoelectric properties for the proposed MFC actuator, it is then possible to generate analogous thermal expansion coefficients for use within ANSYS according to Equation 3.23. The thermal analogy is involved in the static structural analysis to determine the torsion angle (Figure 3.5) and strains arising in the helicopter rotor blade. As the additional parameters the location of centre of gravity and the rotor blade mass are found from the finite element model.

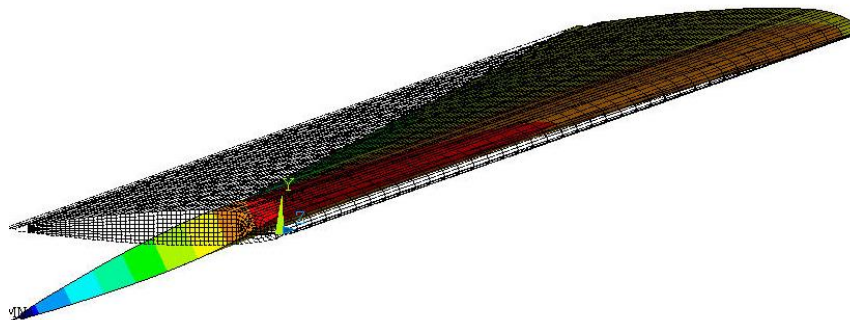


Figure 3.5. Twist of rotor blade

3.2.2. Calculation of the elastic axis

The chordwise elastic axis location is defined as the position along the chord line where a force applied normal to the chord line produces bending without torsion of the blade at any section. Determination of the elastic axis location is more complicated problem and requires a solution of an additional static torsion problem with two forces applied independently from the both sides of the sought elastic centre.

The first force P_1 applied to the unsupported part of the blade is directed parallel to the axis z (Figure 3.6a). The force is applied at a small distance l_0 from the blade nose; therefore the deformation of a blade is described by two values: the vertical displacement, also called bending, and twist. The resultant of the rotor blade displacement is calculated as $\Delta_1 = \Delta_{z1} - \Delta_{z2}$. The second force P_2 is applied at a distance l from the force P_1 (Figure 3.6b). The resultant of the rotor blade displacement is calculated as $\Delta_2 = \Delta_{z3} - \Delta_{z4}$.

The calculated values Δ_1 and Δ_2 of the blade displacement are laid off along the axis z on the coordinate plane zy at the locations of the force application, respectively (Figure 3.7).

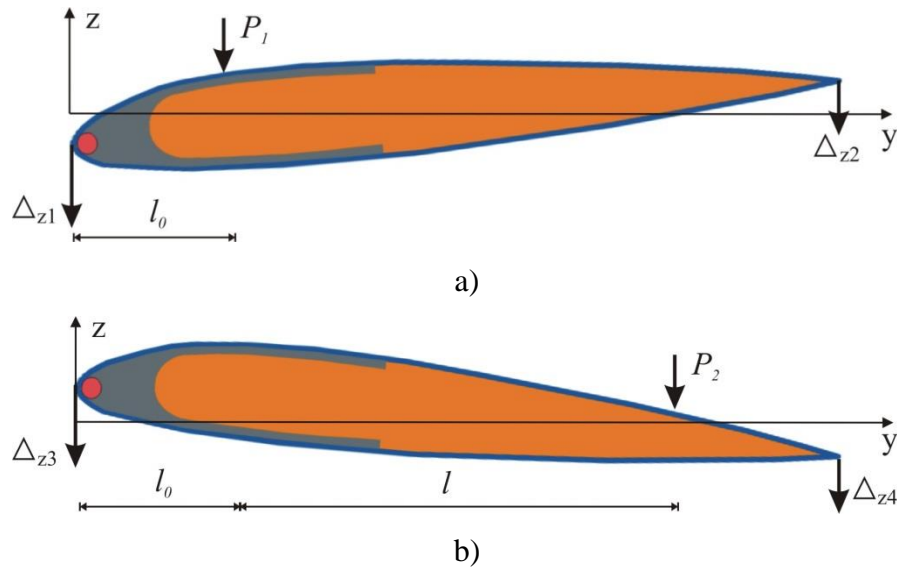


Figure 3.6. Loading conditions and deflection of the rotor blade

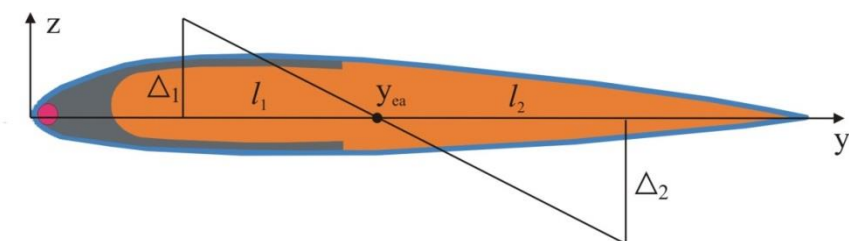


Figure 3.7. Graphical presentation of elastic axis

The resulting points are connected by a straight line whose intersection with the axis y determines the elastic axis location.

Denoting the distances from the external forces P_1 and P_2 from the elastic axis as l_1 and l_2 , respectively, we can write the following expression, in which the distance to the external forces are proportional to their displacements

$$\frac{l_1}{\Delta_1} = \frac{l_2}{\Delta_2} \quad (3.24)$$

or equivalently

$$\frac{\Delta_2}{\Delta_1} = \frac{l_2}{l_1} \quad (3.25)$$

Relation $\frac{l_2}{l_1}$ can be rewritten as

$$\frac{l_2}{l_1} = \frac{l-l_1}{l_1} = \frac{l}{l_1} - 1 \quad (3.26)$$

Combining Equation 3.25 and 3.26

$$\frac{l}{l_1} = \frac{\Delta_2}{\Delta_1} + 1 \quad (3.27)$$

where l_1 is calculated as

$$l_1 = \frac{l}{1 + \frac{\Delta_2}{\Delta_1}} \quad (3.28)$$

Hence the elastic axis location is

$$y_{ea} = (l_0 + l_1) = l_0 + \frac{l}{1 + \frac{\Delta_2}{\Delta_1}} \quad (3.29)$$

3.2.3. Modal analysis

The undamped natural modes of vibration for the 3D finite element model of the rotor blade are calculated within the ANSYS. The general equation of motion in this case is

$$[M]\{\ddot{D}\} + [K]\{D\} = \{F\} \quad (3.30)$$

where: $[M]$ is the mass matrix, $[K]$ is the stiffness matrix, $\{\ddot{D}\}$ is the nodal acceleration vector, $\{D\}$ is the node displacement vector, and $\{F\}$ is the applied time varying nodal load vector [31]. This equation is a set of differential equations in matrix form for the dynamic response of a structure modelled with a finite number of degree of freedom. For the free vibration problem the load is set to zero ($F=0$) and the Equation 3.30 becomes as the following

$$[M]\{\ddot{D}\} + [K]\{D\} = \{0\} \quad (3.31)$$

The nodal displacements and accelerations associated with free vibration may be written as

$$\{D\} = \{A\} \sin \omega t \quad (3.32)$$

$$\{\ddot{D}\} = -\{A\} \omega^2 \sin \omega t \quad (3.33)$$

where $\{A\}$ is the eigenvector associated with each value of ω^2 , ω^2 is an eigenvalue and ω is one of the natural frequencies of vibration. Combining Equations 3.31, 3.32 and (3.33 yields the eigenproblem for undamped free vibration of a multi-degree-of-freedom system

$$([K] - \omega^2 [M])\{A\} = \{0\} \quad (3.34)$$

The modal analysis with block Lanczos mode-extraction method is used to determine the first torsion eigenfrequency (Figure 3.8).



Figure 3.8. First torsion eigenfrequency of the rotor blade

3.3. Convergence study

To start calculations, a convergence of the finite element results should be examined for different meshes. Due to complexity of the structure analysed and large differences (factors greater than 1000) between Young and shear module of different rotor blade components (spar and foam materials), two separate convergence problems were solved for the rotor blade parts: skin mesh along the span of blade and node offset option of skin.

The variants of the finite element mesh of the skin taken for the calculations are outlined in Figure 3.9. The number of elements in the simulation models systematically increased along the span of blade from 20 to 120 elements with the step of 20 elements. In the cross-section of the rotor blade, mesh is not changed. The actuation voltage was fixed at 1000 V. The results of the convergence study are given in Table 3.1.

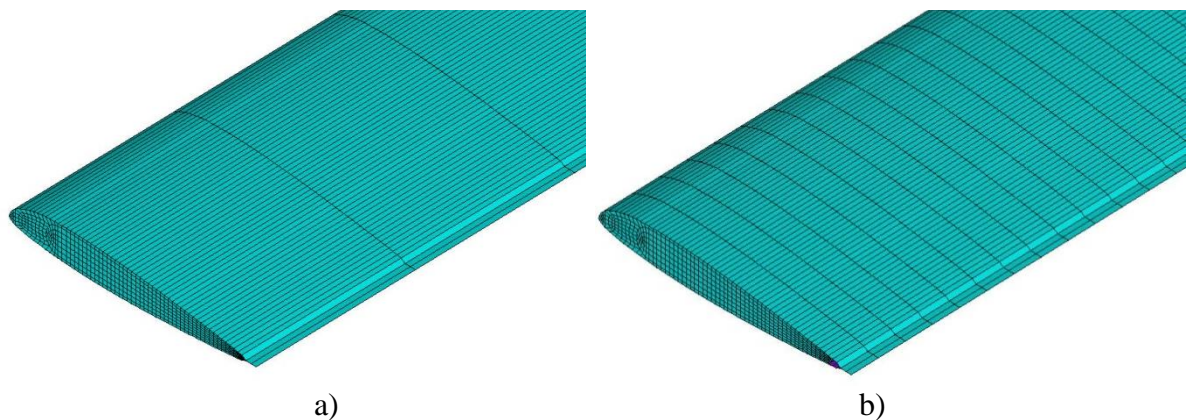


Figure 3.9. Finite element models with different number of elements along the span of blade: (a) 20 elements, (b) 120 elements

Table 3.1.

Solution convergence for different skin meshes

| Number of elements | y_{cg} [%c] | y_{ea} [%c] | m [kg/m] | f_{T1} [Hz] | ε [μ strain] | φ [$^{\circ}$] |
|--------------------|---------------|---------------|------------|---------------|-------------------------------|--------------------------|
| 20 | 30.7 | 17.3 | 1.23 | 55.59 | 842 | 3.38 |
| 40 | 30.7 | 17.4 | 1.23 | 55.59 | 782 | 3.37 |
| 60 | 30.7 | 17.4 | 1.23 | 55.62 | 756 | 3.37 |
| 80 | 30.7 | 17.5 | 1.23 | 55.65 | 741 | 3.37 |
| 100 | 30.7 | 17.5 | 1.23 | – | 732 | 3.36 |
| 120 | 30.7 | 17.5 | 1.23 | – | 725 | 3.36 |

Constant values: $l_1=48$ mm, $l_2=24$ mm, $t_{spar}=1.0$ mm, $t_{skin}=0.5$ mm, $L=100$ mm

The results show that influence of the number of finite elements along the span of blade on the centre of gravity location, elastic axis location and mass per unit span is absent. Influence on the torsion angle is insignificant. The maximal strains arising in the blade demonstrate an average influence depending on the number of elements. The difference

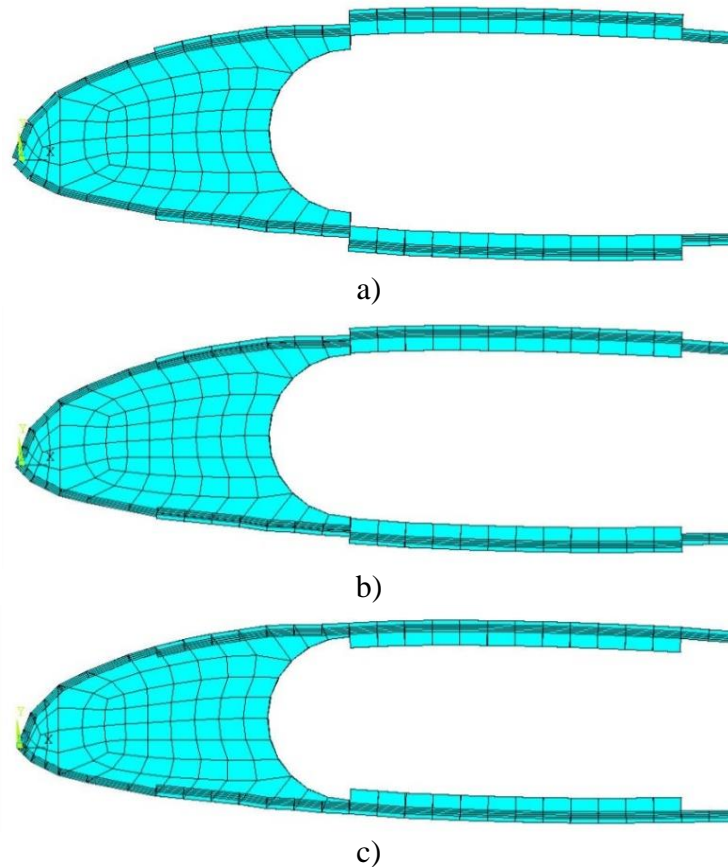


Figure 3.10. Joint skin-spar “moustaches” structure presented by different node offset option: (a) top surface, (b) midsurface, (c) bottom surface

Table 3.2.

Joint skin-spar “moustaches” structure convergence

| Number of variants | y_{cg} [% c] | y_{ea} [% c] | m [kg/m] | f_{T1} [Hz] | ε [μstrain] | φ [°] |
|--------------------|-------------------|-------------------|---------------|------------------|----------------------------|------------------|
| a | 30.7 | 23.4 | 1.23 | - | 782 | 1.95 |
| b | 30.7 | 18.3 | 1.23 | - | 756 | 2.65 |
| c | 30.7 | 17.5 | 1.23 | 55.65 | 741 | 3.37 |

Constant values: $l_1=48$ mm, $l_2=24$ mm, $t_{spar}=1.0$ mm, $t_{skin}=0.5$ mm, $L=100$ mm

between 20 and 120 elements is 14%. The strain was considered in the laminated composite including MFC actuators layer.

The calculation of the first torsional frequency with 100 and 120 elements along the span of blade was not performed because a (virtual) memory of personal computer was insufficient. In two last cases, the results of frequencies are not available.

The joint skin-spar “moustaches” structure was modeled using different node offset options, when the finite element nodes are located at the top, middle and bottom surfaces (Figure 3.10). The rotor blade with 80 elements along the span of blade was used in this study. The results of this study are outlined in Table 3.2. It is seen that influence of the node offset on the centre of gravity location and mass per unit span is absent. The significant difference between different node offset options is obtained for elastic axis and torsion angle. Differences between a) and c) variants for strain is less than 5%.

From the results of mesh analysis, a finite element model with 80 elements along the span of blade and with skin nodes located at bottom surface was chosen for future calculations and research. It is necessary to note that node offset option c) was applied to preserve the rotor blade profile (Table 3.2).

3.4. Parametric study

In these sections parametric studies of the rotor blades with C- and D- spars were carried out in order to determine the influences of the cross-sectional design parameters on the torsion angle (φ) and study the dependence of the behaviour functions on the design parameters. The behaviour functions are included the chordwise location of centre of gravity (y_{cg}) and elastic axis (y_{ea}), blade mass per unit span length (m) and first torsional frequency (f_{T1}). Additionally, for the structural integrity, the maximum allowable blade local strain was studied.

3.4.1. Rotor blade with C-spar

Before formulation of the optimisation problem, a parametric study was carried out with the purpose to decrease the number of design parameters and by this way to increase the accuracy of the optimal results obtained. The design parameters (Figure 3.11) used for this study are spar “moustaches” thickness (t_{spar}) and length (l_1), spar circular fitting (l_2), skin thickness (t_{skin}) and MFC actuator chordwise length (L). Table 3.3 shows the design parameters used for the parametric study are varied within the specified borders.

Finally, for the structural integrity, the maximum allowable strain constraint under the worst case loading condition with a safety factor of 1.4 is added. The maximum strain constraint is defined for composite material and MFC actuators.

An influence of the design parameters on the objective and behaviour functions was estimated using the relative changes of the design parameter within the examined borders. It is necessary to note that the skin thickness is examined as a discrete value design parameter with the following step $\Delta t_{(+45/-45)} = 0.25$ mm.

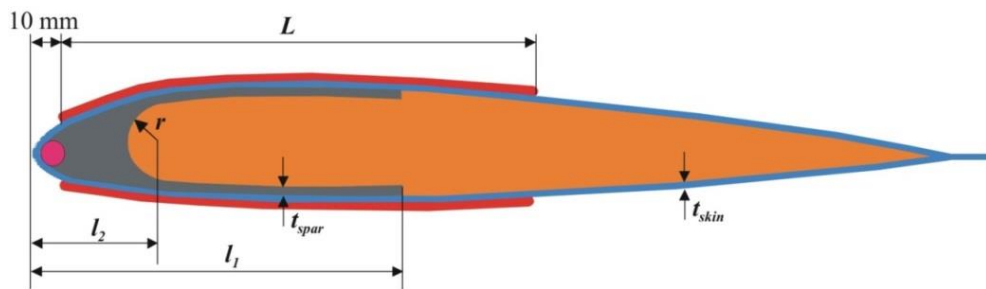


Figure 3.11. C-spar design parameters

Table 3.3.

Variations of C-spar design parameters

| Notation | Symbol | Units | Variation |
|-----------------------|---------------|----------------------|---------------------------------------|
| Skin thickness | t_{skin} | [mm] | $0.25 \leq t_{skin} \leq 1.25$ |
| Spar thickness | t_{spar} | [mm] | $0.50 \leq t_{spar} \leq 2.50$ |
| Spar length | l_1 | [mm] | $0.50 \leq l_1 \leq 2.50$ |
| Spar circular fitting | l_2 | [mm] | $16 \leq l_2 \leq 24$ |
| MFC chordwise length | L | [mm] | $0 \leq L \leq 100$ |
| Local strain | ε | [$\mu\varepsilon$] | $1.4 \times \text{Max strain} < 4000$ |

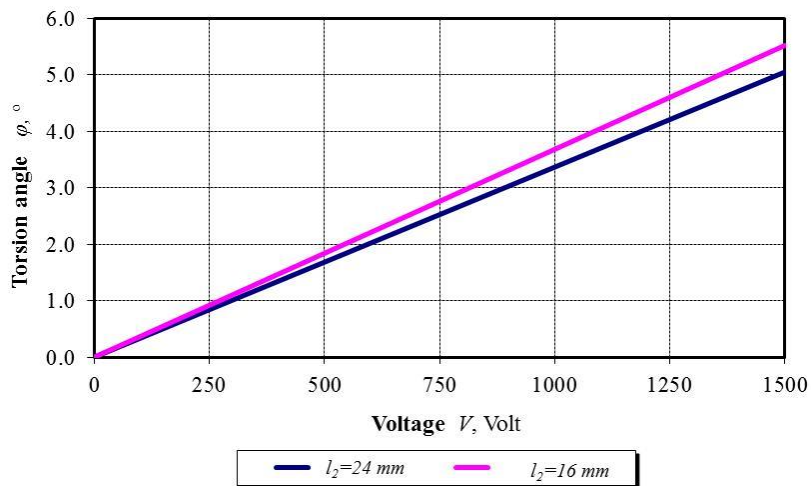


Figure 3.12. Influence of voltage applied on torsion angle

Firstly, the influence of an applied voltage on the value of torsion angle is analysed. A linear relationship between the torsion angle and voltage allows one to find solution in any point of the range from 0 to 1500 V (Figure 3.12). Therefore, for all the active twist studies presented in this thesis, the actuation voltage was fixed at 1000 V.

Torsion angle is used as the objective function to be maximized. Information about the degree of influence of each design parameters on the torsion angle is of primary importance. Summary results of the parametric analysis are presented in Figure 3.13.

It is seen, that the spar “moustaches” length had the smallest influence on the torsion angle (1.9% for $l_2 = 24$ mm and 2.0% for $l_2 = 16$ mm) in comparison with other design parameters. The spar “moustaches” thickness (5.9% for $l_2 = 24$ mm and 6.6% for $l_2 = 16$ mm) and spar circular fitting (8.5%) had a moderate effect. The largest influence on the and spar

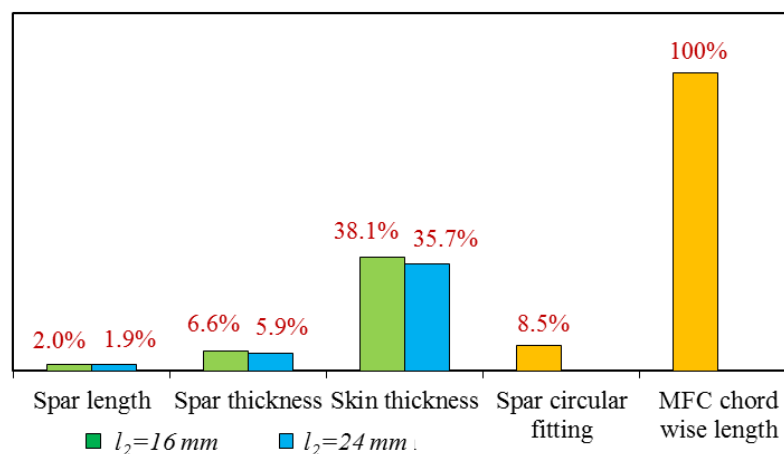


Figure 3.13. Influence of the design variables on torsion angle

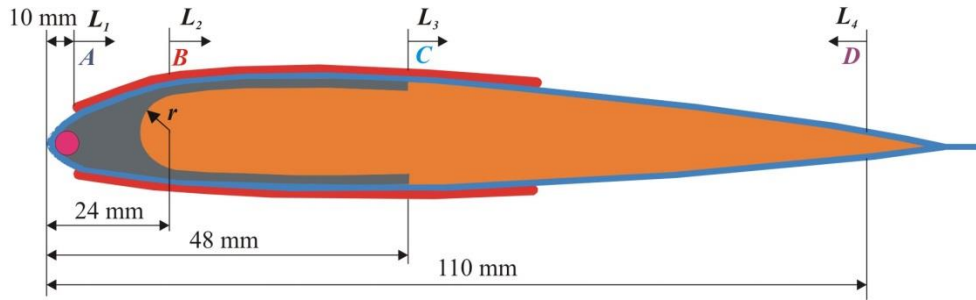


Figure 3.14. Placement of MFC actuators

fitting (8.5%) had a moderate effect. The largest influence on the torsion angle had the skin thickness (35.7% for $l_2 = 24$ mm and 38.1% for $l_2 = 16$ mm) and MFC actuator chordwise length. Moreover, the parametric study showed that the calculated strains were considerably less the permissible value $4000 \mu\epsilon$.

Additional investigations were carried out to evaluate an influence of the MFC actuator location and chordwise length on the rotor blade torsion angle. The diagrams presented in Figure A.5 (see Appendix A) demonstrate that there is a knee approximately in the place of spar circular fitting. This feature can be successfully used for a study of MFC optimal location in the rotor blade. On this reason, four variants of MFC location were considered (Figure 3.14):

1. MFC actuator gluing from A to D (L_1);
2. MFC actuator gluing from B to D (L_2);
3. MFC actuator gluing from C to D (L_3);
4. MFC actuator gluing from D to A (L_4).

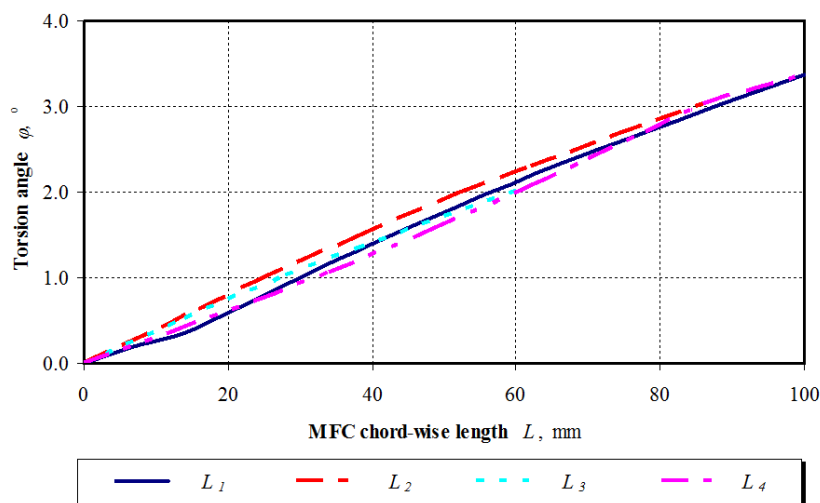


Figure 3.15. Influence of MFC actuator chordwise length and gluing variant on torsion angle ($l_1=48$ mm, $l_2= 24$ mm, $t_{skin}=0.5$ mm, $t_{spar}=1$ mm)

Numerical results presented in Figure 3.15 give possibility to choose an optimal strategy for MFC actuator gluing in the chordwise direction of the rotor blade. It is seen that the variant 2 with a gluing from point B to point D is the more effective. In this case, it is possible to avoid a knee in the diagram.

The parametric study results obtained are summarized in the Appendix A. These results demonstrate how the design variables considered affect the location of centre of gravity, elastic axis, blade mass per unit span, first torsional frequency and torsion angle.

3.4.2. Rotor blade with D-spar

This section is devoted to the dependence of the objective function and the behaviour functions on the design parameters of the rotor blade with D-spar. The design parameters (Figure 3.16) used for this study are spar “moustaches” thickness (t_{spar}) and length (l_1), web thickness (t_{web}), the same thickness of the web and spar ($t_{spar} = t_{web}$), spar circular fitting (l_2), skin thickness (t_{skin}) and MFC actuator chordwise length (L).

Variations of D-spar design parameters are presented in Table 3.4. Data presented in Figure 3.17 illustrate the influences of each design parameter on the torsion angle. The results

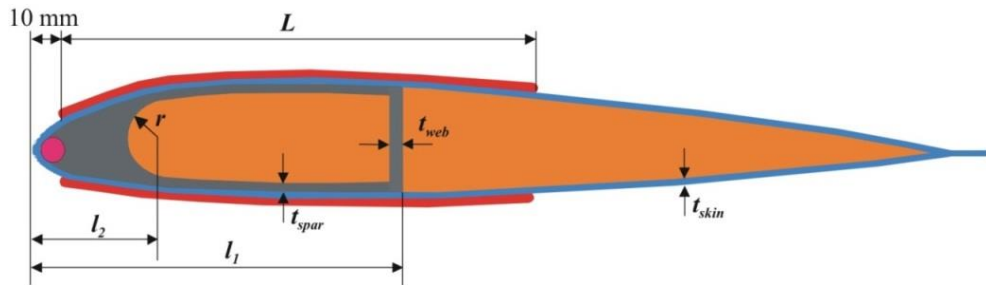


Figure 3.16. D-spar design parameters

Table 3.4.

Variations of D-spar design parameters

| Notation | Symbol | Units | Variation |
|-----------------------|--------------------|-------|--|
| Skin thickness | t_{skin} | [mm] | $0.25 \leq t_{skin} \leq 1.25$ |
| Spar thickness | t_{spar} | [mm] | $0.50 \leq t_{spar} \leq 2.50$ |
| Web thickness | t_{web} | [mm] | $0.50 \leq t_{web} \leq 2.50$ |
| Spar=Web thickness | $t_{spar}=t_{web}$ | [mm] | $0.50 \leq t_{spar} + t_{web} \leq 2.50$ |
| Spar length | l_1 | [mm] | $0.50 \leq l_1 \leq 2.50$ |
| Spar circular fitting | l_2 | [mm] | $16 \leq l_2 \leq 24$ |
| MFC chordwise length | L | [mm] | $0 \leq L \leq 100$ |

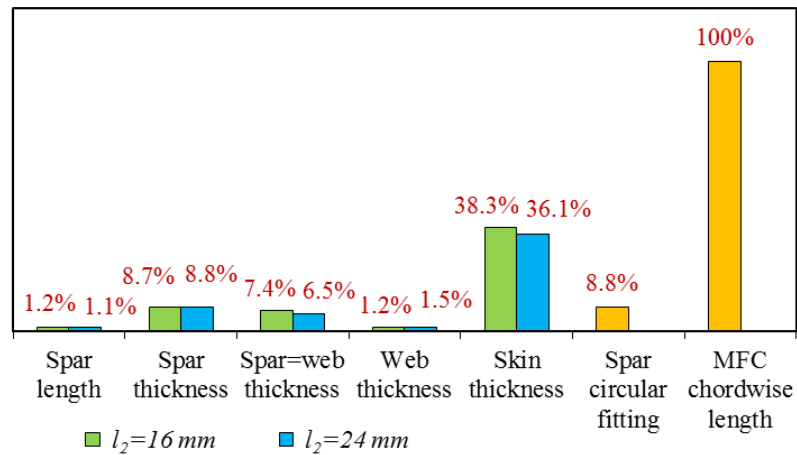


Figure 3.17. Influence of the design parameters on torsion angle

obtained in these studies testify that the spar “moustaches” length and web thickness had the smallest influence on the torsion angle (less than 5%). The spar “moustaches” thickness, the joint thickness of the web and spar “moustaches”, and spar circular fitting demonstrate a moderate influence of ~8.0%. The largest influence on the torsion angle had the skin thickness (36.1% for $l_2 = 24 \text{ mm}$ and 38.3% for $l_2 = 16 \text{ mm}$) and MFC chordwise length.

Numerical results presented in Appendix B illustrate how the design parameters affect the torsion angle, location of centre of gravity and elastic axis, mass of cross-section and first torsional frequency.

4. DESIGN OPTIMISATION METHODOLOGY

This chapter presents the development of an optimisation methodology, based on the planning of experiments and the response surface technique for the design of new rotor blade with MFC actuators. The chapter begins with the mathematical statement of the optimisation problem. Then the proposed methodology for rotor blade optimisation is shown with a flowchart. The descriptions for each component of the methodology follow.

4.1. Optimisation problem statement

The formulation of optimisation problem begins with identifying the design variables, which are primarily varied during the optimisation process. Usually, a design problem involves many design parameters, some of which are highly sensitive to the proper working of the design. These parameters are called the design variables in the optimisation procedures.

Having chosen the design variables, the next task is to identify the constraints associated with the optimisation problem. The constraints represent some functional relationships among the design variables and other design parameters satisfying certain physical phenomenon and certain resource limitations.

The next task in the formulation procedure is to find the objective function in terms of the design variables and other problem parameters. The common engineering objectives involve minimization or maximization of the objective function. Although most of the objectives can be quantified (expressed in mathematical form), there are some objectives that may not be possible to formulate mathematically. In such a case, the approximating mathematical expressions are used.

The final task of the formulation procedure is to set the minimum and maximum bounds on the each design variable. In general, all design variables are restricted to lie within the minimum and maximum bounds. When all four tasks are completed, the mathematical formulation of a general optimisation problem can be stated as follows:

$$\begin{aligned} &\text{Maximize} && f(x) \\ &\text{Subject to} && g_j(x) \leq 0 \quad k=1,2,3,\dots,K \\ & && x_i^{(L)} \leq x_i \leq x_i^{(U)} \quad i=1,2,3,\dots,N \end{aligned}$$

where $f(x)$ is an objective function; $x = (x_1, x_2, \dots, x_n)$ are the design variables; $x_i^{(L)}$, $x_i^{(U)}$ are

the minimum and maximum bounds of the design variables and $g_j(x)$ is constraint function.

For the active twist optimisation of helicopter rotor blade, the objective function $f(x)$ is the torsion angle. The main design variables used in this optimisation problem was taken according to the results of parametric study of the rotor blades with C– and D– spar.

The influence of spar geometry, skin lay-up, position and size of actuators on the torsion angle was studied in helicopter rotor blade with C–spar and D–spar. The parametric study of blade with C–spar has shown that the spar “moustaches” length has the smallest influence on the torsion angle (less than 5%). The spar “moustaches” thickness and spar circular fitting demonstrate an influence in the range: 5.9-8.5%. The largest influence on the torsion angle has the skin thickness (35.7% for $l_2 = 24$ mm and 38.1% for $l_2 = 16$ mm) and MFC chordwise length.

The parametric study of blade with D–spar has shown that the spar “moustaches” length and web thickness also has the smallest influence on the torsion angle (less than 5%). The spar “moustaches” thickness, the same thickness of the web and spar “moustaches” and spar circular fitting demonstrate an influence in the range: 6.5-8.8%. The largest influence on the torsion angle has the skin thickness (36.1% for $l_2 = 24$ mm and 38.3% for $l_2 = 16$ mm) and MFC chordwise length.

Due to their insignificant influence on the torsion angle the spar “moustaches” length in C–spar and the spar “moustaches” length and web thickness in D–spar were excluded from the set of design variables.

Thus, four design variables are used for solution of the optimisation problems in the rotor blades with C– and D– spar

- Spar “moustaches” thickness (t_{spar}).
- Spar circular fitting (l).
- Skin thickness (t_{skin}).
- MFC actuator chordwise length (L).

In the D–spar, the design variable t_{spar} means the same thickness for the web and spar “moustaches” ($t_{spar} = t_{web}$). The design variables of the rotor blades with C– and D– spar is shown in Figure 4.1. Minimum and maximum bounds (domain of interest) for these design variables are listed in Table 4.1.

Through the mathematical optimisation problem, the static twist actuation performance of a blade is maximized while satisfying a series of blade constraints. The

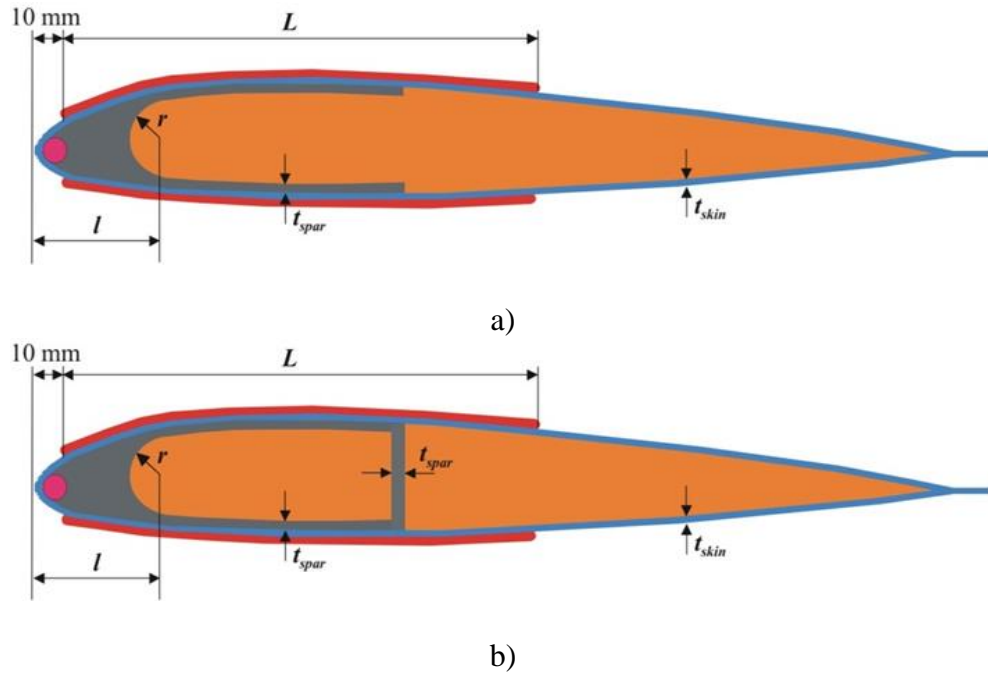


Figure 4.1. Design variables: (a) C-spar design, (b) D-spar design

maximum strain criterion was applied for composite material and MFC actuators and calculated values were compared with the allowable ones. The numerical results of the parametric study were showed that the calculated strains are less than admissible everywhere. Thus, a strain is not considered directly as the constraint in the problems studied in this thesis. The selected constraints for this study are:

- Chordwise location of centre of gravity (y_{cg}).
- Chordwise location of elastic axis (y_{ea}).
- Blade mass per unit span length (m).
- First torsional frequency (f_{T1}).

Table 4.1.

Domain of interest for optimisation: model scale

| Title | Symbol | Units | Bounds |
|-----------------------|------------|-------|--------------------------------|
| Spar circular fitting | l | [mm] | $16 \leq l \leq 24$ |
| Skin thickness | t_{skin} | [mm] | $0.25 \leq t_{skin} \leq 1.25$ |
| Spar thickness | t_{spar} | [mm] | $0.50 \leq t_{spar} \leq 2.50$ |
| MFC chord-wise length | L | [mm] | $16 \leq L \leq 100$ |

Table 4.2.

Minimum and maximum bounds of the constraints: model scale

| Title | Symbol | Units | Bounds |
|----------------------------|----------|--------|--------------------------|
| Centre of gravity location | y_{cg} | [%c] | $22 \leq y_{cg} \leq 30$ |
| Elastic axis location | y_{ea} | [%c] | $10 \leq y_{ea} \leq 25$ |
| Mass per unit span length | m | [kg/m] | $m \leq 1.35$ |
| First torsional frequency | f_{T1} | [Hz] | $f_{T1} \geq 59.1$ |

The constraints for the chordwise locations of the cross-sectional center of gravity and elastic axis are taken into account for aeroelastic stability. Aeroelastic instabilities result from aerodynamic forces that are influenced by the motion of structure. The main type of aeroelastic instability involving coupling of the torsion and the bending of the helicopter rotor blade is flutter. When flutter occurs, it rapidly creates vibrations, and eventual failure of the structure. Locations of the centre of gravity and the elastic axis have an influence on flutter stability. Another concern in the helicopter rotor design with MFC actuators is attempted to minimize the distance between the center of gravity and elastic axis in order to increase the torsion angle and to improve an active control of the rotor blade. The constraints for the blade mass per unit span length and the first torsional frequency of the blade are accounted for a desirable blade dynamics. The lower and upper bounds of constraints for optimisation are given in Table 4.2.

An optimisation problem for the optimum placement of MFC actuators in the full scale rotor blade is formulated on the results of parametric study of model scale rotor blade with C–spar described above. The design variables of the full scale rotor blade are shown in Figure 4.2. Minimum and maximum bounds (domain of interest) for these design variables are listed in Table 4.3. The bounds of the design variables for the full scale rotor blade are determined multiply the bounds of the design variables for the model scale rotor blade by the scale coefficient 2.67. Constraints used during the optimisation are given in Table 4.4.

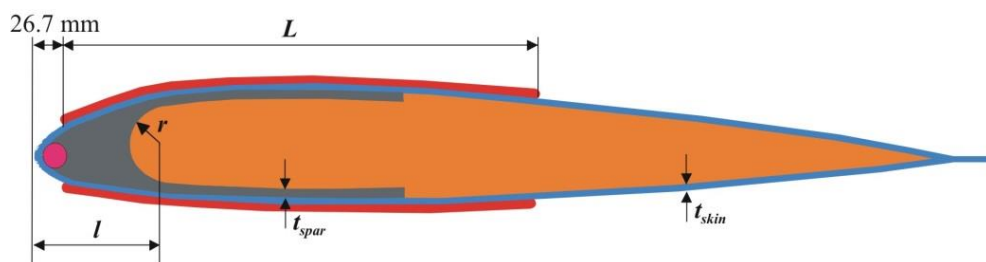


Figure 4.2. Design variables

Table 4.3.

Domain of interest for optimisation: full scale

| Title | Symbol | Units | Bounds |
|-----------------------|------------|-------|--------------------------------|
| Spar circular fitting | l | [mm] | $42.7 \leq l \leq 64.1$ |
| Skin thickness | t_{skin} | [mm] | $0.25 \leq t_{skin} \leq 1.25$ |
| Spar thickness | t_{spar} | [mm] | $1.34 \leq t_{spar} \leq 6.68$ |
| MFC chord-wise length | L | [mm] | $42.7 \leq L \leq 267.0$ |

Table 4.4.

Minimum and maximum bounds of the constraints: full scale

| Title | Symbol | Units | Bounds |
|---------------------------------|----------|--------|--------------------------|
| Centre of gravity location | y_{cg} | [%c] | $y_{cg} = 30$ |
| Elastic axis location | y_{ea} | [%c] | $10 \leq y_{ea} \leq 25$ |
| Blade mass per unit span length | m | [kg/m] | $m \leq 11$ |
| First torsional frequency | t | [Hz] | $f_{T1} \geq 21$ |

4.2. Optimisation methodology

Due to the large dimension of the numerical problem to be solved, an optimisation methodology is developed employing the method of experimental design and the response surface technique. The basic idea of this approach is that simple mathematical models (response surfaces) are determined only using the finite element solutions in the reference points of the experimental design. The significant reduction in calculations is achieved in this case in comparison with the conventional optimisation methods. The general flowchart of the optimisation methodology is shown in Figure 4.3.

The optimisation methodology consists of six stages. In the first stage, a plan of experiments is produced in dependence on the number of design variables and number of experiments. In the second stage, the numerical model is created in order to model the response of a structure and then finite element analysis is performed in the reference points of the experimental design. In the third stage, the numerical data obtained by the finite element calculations in the sample points is used in order to build the approximating functions using the response surface method. These simple mathematical models obtained from the data of experiments are used as the objective functions and the constraints in the optimal design

problem. The non-linear optimisation problem is executed by the random search method using the obtained response surfaces in the next stage. The optimal result of non-linear optimisation is checked using the finite element solution in the five stages. The optimal design variables are used in the numerical model in order to compare difference between the optimisation result and the numerical solution. If the difference between the optimal result and the finite element solution is higher than 5% it is needed to improve the correlations of the approximating functions or change of the design space for some parameters. The procedures are executed before obtaining the final optimal solution.

Two software codes were used for the optimisation of helicopter rotor blade. The first program is universal software EdaOpt which is developed in Machine and Mechanism Dynamics Research Laboratory for the design of physical and numerical experiments, metamodeling and optimisation [6]. This program was used for planning of experiment and simple random search optimisation method. For the approximation of the obtained data the corresponding program RESINT was used in this research [5]. The program was developed also in Riga Technical University and proposed as the algorithm of selection of the terms for non-polynomial regression function [34].

In the following sections, a summary of the theoretical framework required for the optimal designing and optimisation of the rotor blade is presented. The experimental design, which is not dependent on the mathematical model of the object under consideration, is

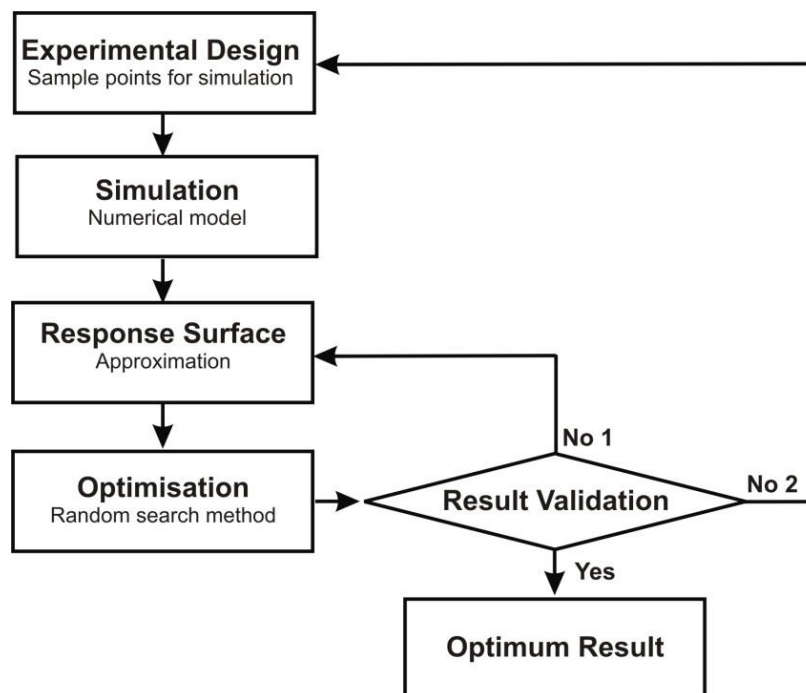


Figure 4.3. The flowchart of optimisation methodology for the designing of rotor blade

described in section 4.2.1. Accuracy of the approximation, as well as the choice of the approximating functions, could have an influence on the optimisation problem solution. For this reason, the choice of the approximation technique is given in the next Section 4.2.2. Finally, describing of the random search method for the solution of optimisation problem is presented in section 4.2.3.

4.2.1. Experiment design

An important aspect of the rotor blade design optimisation is the *design of experiments*. These strategies were originally developed for the model fitting of physical experiments, but can also be applied to numerical experiments. The objective of design of experiments is the selection of the points where the response should be evaluated. A detailed description of the design of experiment theory can be found in Box and Draper [9], Myers and Montgomery [71], among many others.

There is also an important distinction between physical experiments and computer experiments. In physical experiments, there is a measurement error and other random sources of noise that cannot be controlled, which affect the choice of the design point. However, in computer experiments, there is no random error; i.e., for a deterministic computer code, a given input will always yield the same output. Thus, the design of computer experiments need only be space-filling [93, 54]. The classical and space filling design methods are graphically illustrated in Figure 4.4.

Numerous space-filling experimental designs were developed in an effort to provide more efficient and effective means for sampling deterministic computer experiments based on Latin hypercubes (LH). Different space-filling criteria for LH designs were proposed by many authors: Maximin Latin hypercubes [48], Minimal Integrated Mean Squared Error designs [93], Orthogonal array-based LH designs [107], Orthogonal Latin hypercubes [121], Integrated Mean Squared Error (IMSE) and optimal Latin hypercubes [76].

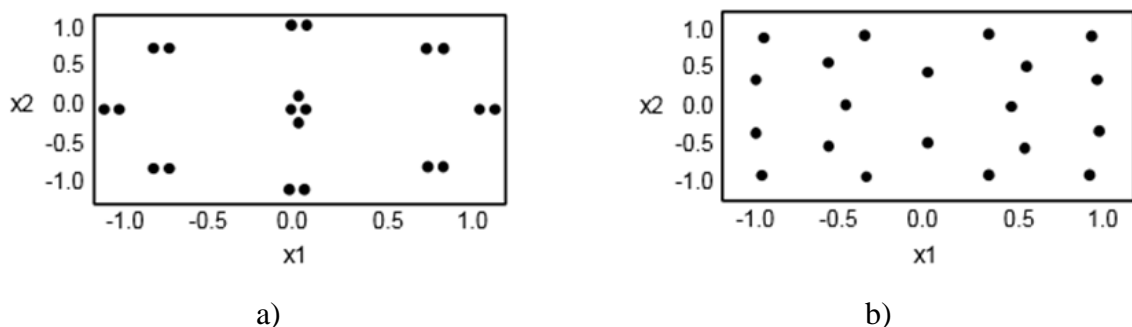


Figure 4.4. Graphical interpretations of Classic Design (a) and Space Filling design (b) [8]

Audze and Eglais [5] suggested a non-traditional criterion for elaboration of the plans of experiments which is not dependent on the mathematical model of the object or process under consideration. The initial information for development of the plan is the number of variables n and the number of experiments k . The number of levels of factors (same for each factor) is equal to the number of experiments and for each level there is only one experiment. The points of experiments in the domain of factors are distributed as regular as possible. For this reason the following criterion is used:

$$\Phi = \sum_{i=1}^k \sum_{j=i+1}^k \frac{1}{l_{ij}^2} \Rightarrow \min \quad (4.1)$$

where l_{ij} is a distance between the points having numbers i and j ($i \neq j$). Physically it is equal to the minimum of potential energy of the repulsive forces for the points with unity mass if the magnitude of these repulsive forces is inversely proportional to the distance between the points. Minimum of this criterion are being defined. The problem to minimize the criterion (Equation 4.1) leads to the solving of a non-linear programming problem. Solving the non-linear programming problem, the plans of experiments were determined for different number of the design variables n and number of the experiments k .

The plan of experiment is characterised by the matrix of plan B_{ij} . The domain of interest (domain of variables) is determined as $x_j \in [x_j^{\min}; x_j^{\max}]$, where x_j^{\min} and x_j^{\max} are the lower and the upper bounds of design variables, respectively. Thus, in this domain the sample points, where the experiments must be performed, are calculated by the expression:

$$x_j^{(i)} = x_j^{\min} + \frac{1}{k-1} (x_j^{\max} - x_j^{\min}) (B_{ij} - 1) \quad i = 1, 2, \dots, k; \quad j = 1, 2, \dots, n \quad (4.2)$$

Since the matrices of plan B_{ij} are universal, these may be used for various design and optimisation problems. The Audze – Eglais experimental design will be employed in this thesis. The program EDAOpt [6] was used for the generation of the experimental design.

4.2.2. Response surface approximation

Mathematical models using data of experiments can be obtained by various methods. Low-order polynomial approximations are the most widely used and are described in every statistics book, and implemented in every statistics program. First, second and third-order polynomials can be expressed as follows:

$$\hat{F}(x) = b_0 + \sum_{i=1}^m b_i x_i \quad (4.3)$$

$$\hat{F}(x) = b_0 + \sum_{i=1}^m b_i x_i + \sum_{i=1}^m \sum_{j=i}^m b_{ij} x_i x_j \quad (4.4)$$

$$\hat{F}(x) = b_0 + \sum_{i=1}^m b_i x_i + \sum_{i=1}^m \sum_{j=i}^m b_{ij} x_i x_j + \sum_{i=1}^m \sum_{j=i}^m \sum_{k=j}^m b_{ijk} x_i x_j x_k \quad (4.5)$$

where m is total amount of variables; b_0 , b_i , b_{ij} , b_{ijk} are unknown coefficients of regression functions.

As stated by Myers and Montgomery [71], there is a considerable practical experience indicating that second-order models work well in solving real response surface problems. In general it is thought that third and higher order polynomials can over-fitting data, consequently avoiding construction of global behaviour of the parameters. On the contrary, first order-polynomials are too simple and give prediction errors too high for use in science and engineering.

In general, the design variables in engineering problems are not equally distributed. For example, in the analysis of a simple beam bending, beam length, height and thickness have different effects on the response. Moreover, the response parameters are commonly affected by only some of the input variables, and the irrelevant parameters become approximation noise that decreases prediction accuracy. In light of this, it seems reasonable to use partial polynomials instead of full-order polynomial approximations. In such an assumption, the polynomial parameters are used adequately with relevance to the input variables [3]. By generalising the idea of polynomials, the nonlinear regression function is the linear combination of any kind of function. Such a model is written as follows:

$$\hat{F}(x) = b_0 F_0(x_1, x_2, \dots, x_D) + b_1 F_1(x_1, x_2, \dots, x_D) + \dots + b_{m-1} F_{m-1}(x_1, x_2, \dots, x_D) \quad (4.6)$$

where $F = \{F_i\}$ is a set of linearly independent functions consisting exclusively of m functions.

Eglais [34] proposed the algorithm of selection of the terms for non-polynomial regression function. In his work, the “correlation” approach for the optimal choice of the number of terms was also proposed. This method was also used in [86, 87, 88] to determine the simple mathematical models for the structural optimisation problems. This approximation method proposed by Eglais is employed for the solution of the optimisation problem considered here and is briefly outlined further.

In the present approach the form of the regression equation is unknown in advance. There are two requirements for the regression equation: accuracy and reliability. Accuracy is characterised as a minimum of standard deviation of the table data from the values given by the regression equation. Increasing the number of the terms in the regression equation, it is possible to obtain a complete agreement between the table data and values given by the regression equation. However, it is necessary to note that prediction in the intervals between the table points cannot be accurate.

For an improvement of prediction, it is necessary to decrease the distance between the points of the experiments by increasing the number of experiments or by decreasing the domain of factors. Reliability of the regression equation can be characterised by the affirmation that standard deviations for the table points and for any other points are approximately the same. Obviously, the reliability is greater for a smaller number of terms of the regression equation.

The regression equation can be written in the following form

$$y = \sum_{i=1}^p A_i f_i(x_j) \quad (4.7)$$

where A_i are the coefficients of the equation of regression, $f_i(x_j)$ are the functions from the bank of simple functions $\varphi_1, \varphi_2, \dots, \varphi_k$ which are assumed as,

$$\varphi_k(x_j) = \prod_{i=1}^n x_j^{\alpha_{ki}} \quad (4.8)$$

where n is the number of the object parameters and a_{ki} is a positive or negative integer including zero. Synthesis of the equation from the bank of simple functions is carried out in two stages: selection of perspective functions from the bank and then step-by-step elimination of the selected functions.

Selection of the perspective functions is carried out in the following manner. For all functions from the bank, with the least square method, coefficients A_i and B_i of simple equations of regression are determined:

$$y_i = A_i + B_i \varphi_i(x_i) \quad (4.9)$$

The sum of deviations is also calculated

$$S_i = \sum_{j=1}^k [A_i + B_i \varphi_i(x_j) - y_j]^2 \quad (4.10)$$

where k is the number of points. Simple functions with minimum S_i are selected as perspective. After that we find the perspective function for the differences

$$\Delta_j = A_0 + \sum_{i=1}^p A_i f_i(x_j) - y_j; \quad j = 1, 2, \dots, k \quad (4.11)$$

where p is the number of the selected perspective functions, $f_i(x_j)$ are the selected perspective functions, A_0 and A_i are the coefficients found by the least square method.

After selection of the predicted number of the perspective functions, the elimination is carried out. In the first stage, all variants are tested with the least square method and the function, which leads to the minimum of the sum of deviations, is chosen for each variant. In the second stage, the elimination is carried out using the standard deviation

$$\sigma_0 = \sqrt{\frac{S}{k-p+1}}, \quad \sigma = \sqrt{\frac{1}{k-1} \sum_{i=1}^k \left(y_i - \frac{1}{k} \sum_{j=1}^k y_j \right)^2} \quad (4.12)$$

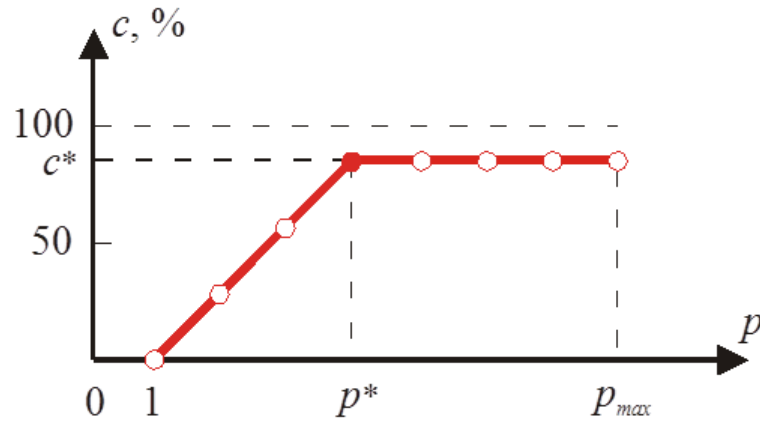


Figure 4.5. Diagram of elimination for the correlation coefficient

or correlation coefficient

$$c = \left(1 - \frac{\sigma}{\sigma_0}\right) * 100\% \quad (4.13)$$

where k is the number of experimental points, p is the number of the selected perspective functions and S is the minimum sum of deviations. It is more convenient to characterise the accuracy of the regression equation by the correlation coefficient (Figure 4.5).

If insignificant functions are eliminated from the regression equation, the reduction of the correlation coefficient is negligible. If in the regression equation only significant functions are presented, elimination of one of them leads to important decrease of the correlation coefficient.

4.2.3. Random search method

Most of the real world system models involve the nonlinear optimisation with the complicated objective functions or the constraints for which analytical solutions (solutions using quadratic programming, geometric programming, etc.) are not available. In such cases one of the possible solutions is the search algorithm in which, the objective function is first computed with a trial solution and then the solution is sequentially improved based on the corresponding objective function value till convergence.

The search algorithms can be broadly classified into two types: (1) direct search algorithm and (2) indirect search algorithm [33]. Direct search methods are those where the optimal point is sought by „trial and error“. Techniques called *pattern search* methods identify the appropriate directions in which successive trials have to proceed. These methods

require only the objective function and not its partial derivatives in order to find minimum. Hence, such methods are often called nongradient methods. In general, direct search methods are not as efficient as descent methods and most suitable for problems that are simple and involve a relatively small number of variables. On the other hand, descent methods utilize, in addition to the function value, the first, and in some cases second, derivative of the objective function. Descent methods are also called *gradient methods*.

In the present thesis, the non-linear optimisation problem is executed by the random search method which is one of the direct search algorithms [72]. A random search method simply selects a starting vector x^0 , evaluates $f(x)$ at x^0 , and then randomly selects another vector x^1 and evaluates $f(x)$ at x^1 . In effect, both a search direction and step length are chosen simultaneously. After one or more stages, the value of $f(x^k)$ is compared with the best previous value of $f(x)$ from among the previous stages, and decision is made to continue or terminate the procedure. Variations of this form of random search involve randomly selecting a search direction and then minimizing (possibly by random step) in that search directions as a series of cycles. Clearly, the optimal solution can be obtained with a probability of 1 only as $k \rightarrow \infty$ but as a practical matter, if the objective function is quite flat, a suboptimal solution may be quite acceptable.

5. OPTIMAL DESIGN OF MODEL SCALE ROTOR BLADES

In this chapter, optimisation results are presented for the model scale rotor blades with C- and D- spars and two possible applications of the piezoelectric actuators. Analysis of numerical data by the response surfaces is carried out to investigate an influence of different design variables on the behaviour functions. Torsion angle obtained from the finite element simulation of helicopter rotor blade is compared with the experimental value to confirm the modelling accuracy. Finally, Design Tool that was produced using the methodology developed for the optimum placement of Macro Fiber Composite actuators in the helicopter rotor blades is presented.

5.1. Optimisation results

The plan of experiment and verification of the response surfaces are presented in the first section. The optimisation results of the rotor blades with C- and D- spars are displayed in the next sections.

5.1.1. Solution of optimisation problem

For the optimisation problem solution, the plan of experiment with four unknown parameters ($n=4$), namely, $(x) = [l, t_{skin}, t_{spar}, L]^T$, and 30 experiment points ($k=30$) were selected for rotor blades. The minimal number of experiments for second order polynomial with n variables is $(n+1)(n+2)/2$. It is common practice to use a two times greater number of experiments. The plans of experiments are presented in Figure 5.1 and numerical values of the experimental plan are given in Table 5.1.

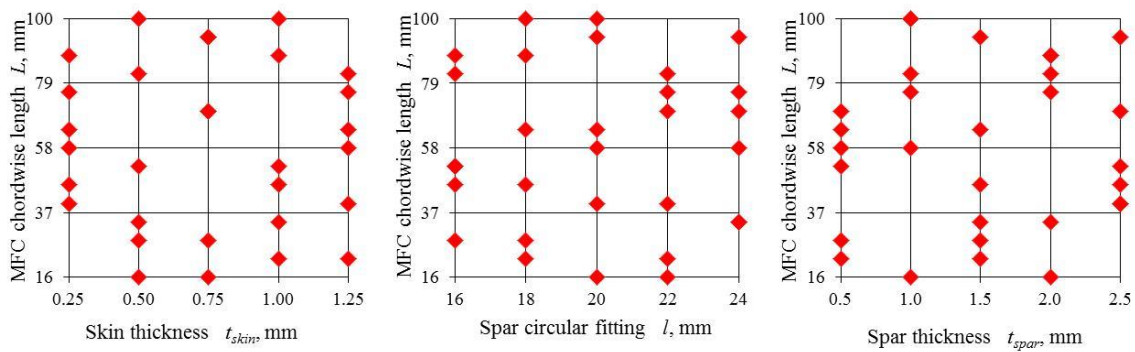


Figure 5.1. Plans of experiments: 2D-view

Table 5.1.

Plan of experiment

| Experimental points | Design variables | | | |
|---------------------|-----------------------------------|-----------------------------------|-----------------------------------|---|
| | Spar circular fitting l , mm | Skin thickness t_{skin} , mm | Spar thickness t_{spar} , mm | MFC actuator chordwise length L , mm |
| 1 | 20 | 0.75 | 2.5 | 94 |
| 2 | 24 | 0.50 | 2.0 | 34 |
| 3 | 16 | 1.00 | 2.0 | 88 |
| 4 | 16 | 0.50 | 1.0 | 82 |
| 5 | 22 | 0.25 | 2.0 | 76 |
| 6 | 16 | 0.50 | 2.5 | 52 |
| 7 | 20 | 1.25 | 0.5 | 58 |
| 8 | 20 | 0.50 | 1.0 | 100 |
| 9 | 22 | 0.50 | 1.0 | 16 |
| 10 | 16 | 1.00 | 0.5 | 52 |
| 11 | 22 | 1.25 | 2.5 | 40 |
| 12 | 24 | 1.00 | 1.5 | 34 |
| 13 | 18 | 0.25 | 2.0 | 88 |
| 14 | 24 | 0.75 | 2.5 | 70 |
| 15 | 22 | 1.25 | 2.0 | 82 |
| 16 | 18 | 1.00 | 1.0 | 100 |
| 17 | 18 | 1.00 | 2.5 | 46 |
| 18 | 20 | 0.25 | 0.5 | 64 |
| 19 | 20 | 0.25 | 2.5 | 40 |
| 20 | 20 | 0.75 | 2.0 | 16 |
| 21 | 24 | 0.75 | 1.5 | 94 |
| 22 | 18 | 1.25 | 1.5 | 64 |
| 23 | 22 | 1.00 | 0.5 | 22 |
| 24 | 16 | 0.25 | 1.5 | 46 |
| 25 | 24 | 0.25 | 1.0 | 58 |
| 26 | 22 | 0.75 | 0.5 | 70 |
| 27 | 24 | 1.25 | 1.0 | 76 |
| 28 | 16 | 0.75 | 1.5 | 28 |
| 29 | 18 | 0.50 | 0.5 | 28 |
| 30 | 18 | 1.25 | 1.5 | 22 |

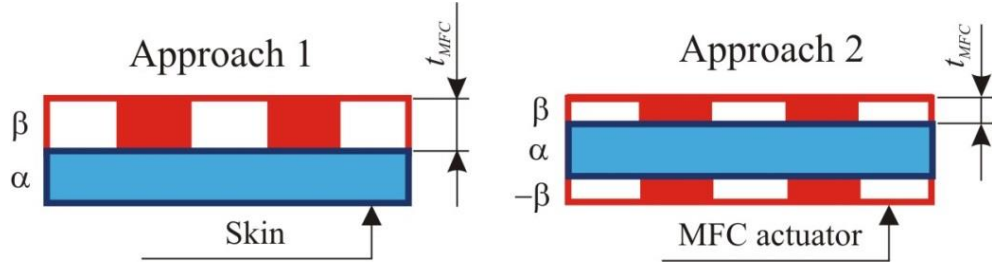


Figure 5.2. Application of MFC actuators

For an improvement of the twist actuation performance of rotor blades with C- and D-spars, two design solutions for an application of MFC actuator were used in this study (Figure 5.2):

- Approach 1 – application of MFC actuator on the top of skin;
- Approach 2 – application of MFC actuator on the top and bottom of skin.

Subsequently in the points of plan of experiments the finite element solutions were obtained. In the next stage the numerical data obtained by the finite element calculations in the points of plan of experiments was used in order to build the approximating functions using the program RESINT. Relationship between the design variables x and the corresponding behaviour functions $f(x)$ of the finite element model of rotor blades were build employing partial polynomial approximations. Approximating function for the torsion angle (φ) is given as

$$f(x) = 0.408 + 0.087 \cdot z_4 - 0.095 \cdot z_3 - 0.046 \cdot z_2 \cdot z_4 + 0.444 \cdot z_2 \cdot z_2 - 0.002 \cdot z_4 \cdot z_4 - 0.004 \cdot z_1 \cdot z_4 + 0.002 \cdot z_2 \cdot z_2 \cdot z_4 \cdot z_4 \quad (5.1)$$

Here, the normalized variables z_i are introduced

$$\begin{aligned} z_1 &= (-5 + 0.25 \cdot x_1) \\ z_2 &= (-1.5 + 2 \cdot x_2) \\ z_3 &= (-1.5 + x_3) \\ z_4 &= (-1.381 + 0.024 \cdot x_4) \end{aligned} \quad (5.2)$$

where x_1 is the spar circular fitting (l), x_2 is the skin thickness (t_{skin}), x_3 is the spar “moustaches” thickness (t_{spar}), and x_4 is the MFC actuator chordwise length (L).

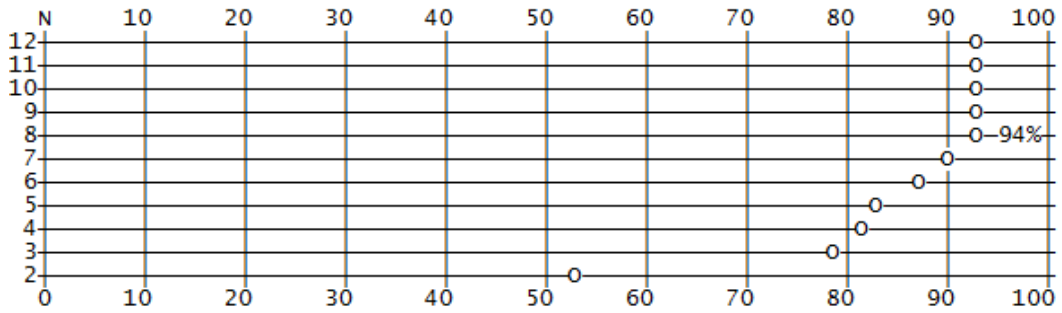


Figure 5.3. Diagram of elimination

Correlation of the approximating function with the finite element calculations data for the torsion angle (φ) is $c=94.0\%$. The elimination diagram is shown in Figure 5.3. It can be seen that the knee in the diagram corresponds to the regression expression with 8 terms. Eliminating the eight term from the regression expression, the correlation of the approximating function decreases significantly $c = 90.0\%$. For this reason the approximating function with eight terms was selected. It should be noted that polynomial terms are not selected a priori but are obtained in the process of building the model.

Similar, approximations of the original functions for the behaviour constrains were obtained using low order polynomials with some eliminated points. They were determined with the correlation coefficients higher than 90%. These response surfaces are verified by the finite element solutions in the points different from the points taken in the plan of experiments

Examples of finite element verification of the response surfaces for the approach 1 and approach 2 of helicopter rotor blade with C-spar are presented in Figure 5.4 and Figure 5.5,.

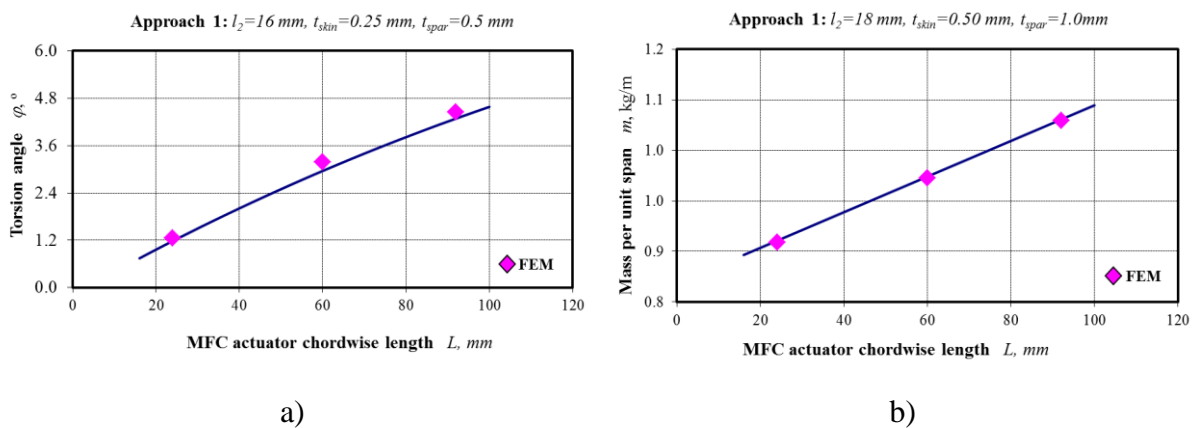
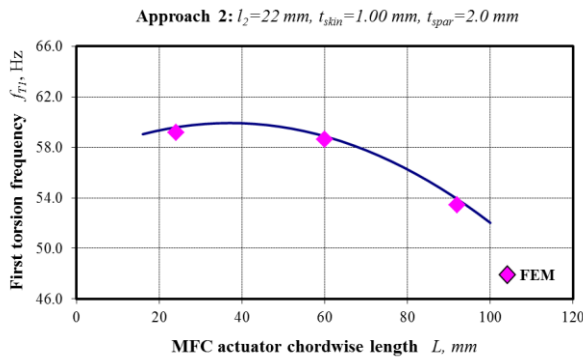
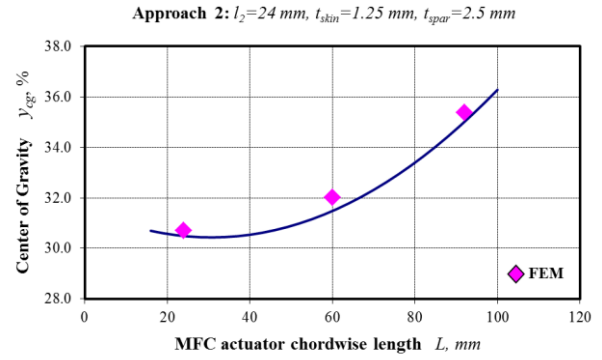


Figure 5.4. Verification of the response surfaces for rotor blade with C-spar and approach 1: the torsion angle (a) and blade mass per unit span length (b) dependence on the MFC actuators chordwise length

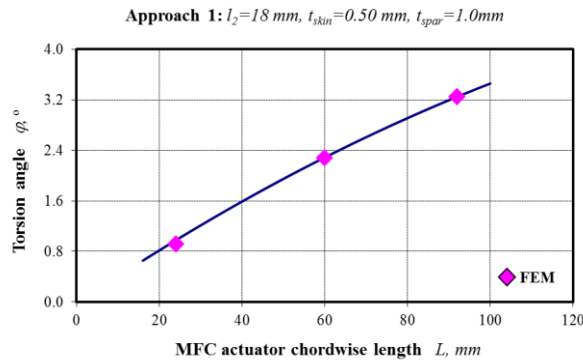


a)

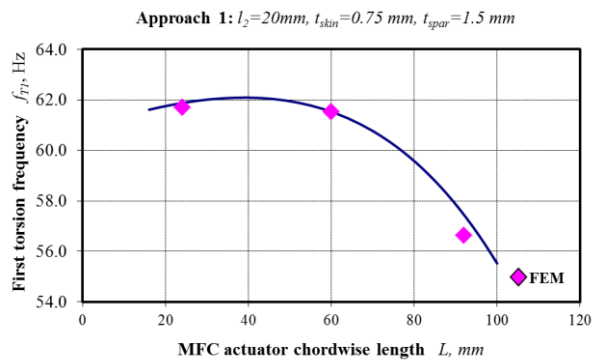


b)

Figure 5.5. Verification of the response surfaces for rotor blade with C-spar and approach 2: the first torsion frequency (a) and centre of gravity (b) dependence on the MFC actuators chordwise length

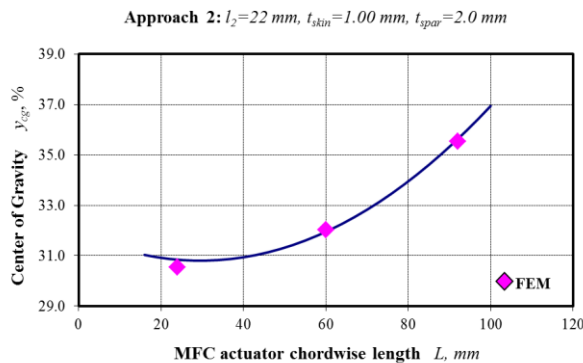


a)

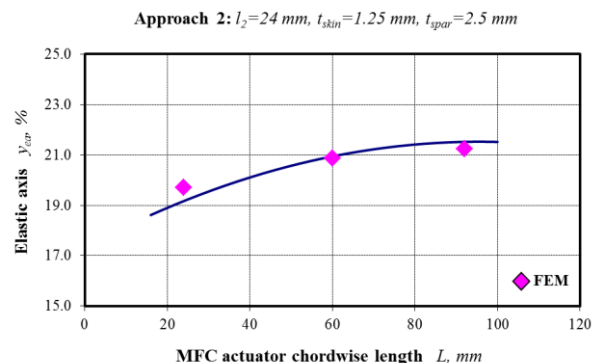


b)

Figure 5.6. Verification of the response surfaces for rotor blade with D-spar and approach 1: the torsion angle (a) and first torsion frequency (b) dependence on the MFC actuators chordwise length



a)



b)

Figure 5.7. Verification of the response surfaces for rotor blade with D-spar and approach 2: the first torsion frequency (a) and centre of gravity (b) dependence on the MFC actuators chordwise length

where a very good correlation is observed for the approximations and finite element solutions in the control points. Examples of finite element verification of the response surfaces for the approach 1 and approach 2 of helicopter rotor blade with D-spar are presented in Figure 5.6 and Figure 5.7 respectively.

Non-linear optimisation problem was solved by the random search method using the response surfaces obtained in the corresponding program EdaOpt. The results obtained were verified by the comparing the optimal solution with the numerical ones obtained by FEM at the point of optima.

5.1.2. Rotor blade with C-spar

The optimisation results obtained for the rotor blade with C-spar are listed in Table 5.2 and Table 5.3. The maximum torsion angle reaches 3.91° and 5.52° for approach 1 and approach 2 respectively; when voltage is 1000 V. Using a linear interpolation of twist deflection with a maximum voltage $2000V_{pp}$, the maximum torsion angles reaches 7.82° peak-to-peak (pp) and 11.04° peak-to-peak (pp).

The optimal results obtained with the response surface model (RSM) are compared with the finite element solutions (FEM). It is seen that differences between the optimal and numerical results using geometrical data obtained by the optimisation are very small. Mostly residuals do not exceed 2%, which show good correlation of the approximating functions.

Table 5.2.

Optimisation results of rotor blade with C-spar (Approach 1)

| | Title | Symbol | Units | RSM | FEM | Δ , % |
|--------------------|---------------------------------|------------|----------------|-------|-------|--------------|
| Design variables | Spar circular fitting | l | [mm] | 24.00 | 24.00 | – |
| | Skin thickness | t_{skin} | [mm] | 0.25 | 0.25 | – |
| | Spar thickness | t_{spar} | [mm] | 0.50 | 0.50 | – |
| | MFC chordwise length | L | [mm] | 91.00 | 90.00 | – |
| Constraints | Centre of gravity location | y_{cg} | [%c] | 26.50 | 26.70 | 0.7 |
| | Elastic axis location | y_{ea} | [%c] | 16.30 | 16.60 | 1.8 |
| | Blade mass per unit span length | m | [kg/m] | 0.99 | 0.99 | 0 |
| | First torsional frequency | f_{T1} | [Hz] | 59.15 | 57.90 | 2.1 |
| Objective function | Torsion angle | φ | [$^\circ$] | 3.91 | 3.88 | 0.7 |
| | Torsion angle | φ | [$^\circ$ pp] | 7.82 | 7.76 | 0.7 |

Table 5.3.

Optimisation results of rotor blade with C– spar (Approach 2)

| | Title | Symbol | Units | RSM | FEM | Δ , % |
|--------------------|---------------------------------|------------|--------|-------|-------|--------------|
| Design variables | Spar circular fitting | l | [mm] | 16.00 | 16.00 | – |
| | Skin thickness | t_{skin} | [mm] | 0.25 | 0.25 | – |
| | Spar thickness | t_{spar} | [mm] | 1.50 | 1.50 | – |
| | MFC chordwise length | L | [mm] | 77.00 | 76.00 | – |
| Constraints | Centre of gravity location | y_{cg} | [%c] | 28.90 | 29.20 | 1.0 |
| | Elastic axis location | y_{ea} | [%c] | 15.70 | 16.00 | 1.8 |
| | Blade mass per unit span length | m | [kg/m] | 1.16 | 1.14 | 1.7 |
| | First torsional frequency | f_{T1} | [Hz] | 59.30 | 59.82 | 0.9 |
| Objective function | Torsion angle | φ | [°] | 5.52 | 5.56 | 0.7 |
| | Torsion angle | φ | [°pp] | 11.04 | 11.12 | 0.7 |

The results show that the differences of the maximal torsion angles between two approaches achieve 29.1%. The minimal distance between location of the centre of gravity and elastic axis is 10.2% for approach 1 and 13.2% for approach 2. In this case, approach 1 is effective on 22.7%. The mass of optimal rotor blade is 1.54 kg for approach 1 and 1.81 kg for approach 2. Difference between two approaches is 14.9%. Another important observation from the analysis is that the first torsion frequencies for the optimized cases are close to the lower bounds of constraints.

5.1.3. Rotor blade with D–spar

Optimisation results of the rotor blade with D – spar are given in Table 5.4 and Table 5.5, respectively. The maximum torsion angle reaches 4.01° and 5.39° for approach 1 and approach 2 respectively; when voltage is 1000 V. The differences between the optimal and numerical results do not exceed 3%, which show good correlation of the approximating functions.

The results show that the differences of the maximal torsion angles between two approaches achieve 25.6%. The minimal distance between location of the centre of gravity and elastic axis is 7.6% for approach 1 and 11.3% for approach 2. In this case, approach 1 is effective on 32.7%. The mass of optimal rotor blade 1.50 kg for approach 1 is and 1.87 kg for approach 2. Difference between two approaches is 19.8%. The first torsion frequencies are closer to the lower bounds of constraints.

Table 5.4.

Optimisation results of the rotor blade with D– spar (Approach 1)

| | Title | Symbol | Units | RSM | FEM | Δ , % |
|--------------------|---------------------------------|------------|--------|-------|-------|--------------|
| Design variables | Spar circular fitting | l | [mm] | 16.00 | 16.00 | – |
| | Skin thickness | t_{skin} | [mm] | 0.25 | 0.25 | – |
| | Spar thickness | t_{spar} | [mm] | 1.00 | 1.00 | – |
| | MFC chordwise length | L | [mm] | 89.00 | 88.00 | – |
| Constraints | Centre of gravity location | y_{cg} | [%c] | 29.70 | 29.40 | 1.0 |
| | Elastic axis location | y_{ea} | [%c] | 22.10 | 21.90 | 0.9 |
| | Blade mass per unit span length | m | [kg/m] | 0.96 | 0.95 | 1.0 |
| | First torsional frequency | f_{T1} | [Hz] | 59.15 | 58.10 | 1.8 |
| Objective function | Torsion angle | φ | [°] | 4.01 | 4.04 | 0.7 |
| | Torsion angle | φ | [°pp] | 8.02 | 8.08 | 0.7 |

Table 5.5.

Optimisation results of the rotor blade with D– spar (Approach 2)

| | Title | Symbol | Units | RSM | FEM | Δ , % |
|--------------------|---------------------------------|------------|--------|-------|-------|--------------|
| Design variables | Spar circular fitting | l | [mm] | 22.00 | 22.00 | – |
| | Skin thickness | t_{skin} | [mm] | 0.25 | 0.25 | – |
| | Spar thickness | t_{spar} | [mm] | 0.50 | 0.50 | – |
| | MFC chordwise length | L | [mm] | 82.00 | 82.00 | – |
| Constraints | Centre of gravity location | y_{cg} | [%c] | 29.40 | 29.00 | 1.4 |
| | Elastic axis location | y_{ea} | [%c] | 18.10 | 17.70 | 2.3 |
| | Blade mass per unit span length | m | [kg/m] | 1.20 | 1.23 | 2.5 |
| | First torsional frequency | f_{T1} | [Hz] | 59.77 | 58.88 | 1.5 |
| Objective function | Torsion angle | φ | [°] | 5.39 | 5.39 | 0.0 |
| | Torsion angle | φ | [°pp] | 10.78 | 10.78 | 0.0 |

5.2. Comparative study

Optimisation results for the first approach of C– and D–spar design are given in Tables 5.2 and 5.4, showing that the results for C– and D–spar designs almost are the same. Difference between results is 2.5 %. But the minimal distance between location of the centre of gravity and elastic axis is 10.2% for C–spar and 7.6% for D–spar. In this case, the D–spar is effective on 25.5%. Optimisation results for the second approach are presented in Tables

5.3 and 5.5. Difference between the results of torsion angles for the second approach are 2.4%. However, the minimal distance between the location of centre of gravity and elastic axis is 13.2% for C–spar and 11.3 % for D–spar. In the second approach, the D–spar is effective on 14.4%.

From the optimisation results, it is seen that the D– and C–spar have approximately the same results of maximal torsion angle for two approaches. However, the minimal distance between the centre of gravity and elastic axis demonstrates that D–spar is more effective, especially for the first approach.

5.3. Parametric study by response surfaces

Parametric study by the response surfaces were carried out additionally for a designer convenience to investigate an influence of different design parameters on the behaviour functions. Analysis was performed for the helicopter rotor blade with C–spar and approach 1.

The view of the response surfaces is shown in Figures 5.8 – 5.12. In these figures, two design variables are kept fixed and the other two are varied between the maximum and minimum design bounds.

Figure 5.8 shows the torsion angle dependency on the design variables. It can be seen that the value of torsion angle significantly increases with an increase of MFC actuator chordwise length. In other cases, an increase of spar circular fitting and thickness of spar and skin reduces the value of torsion angle.

When the spar “moustaches” thickness and spar circular fitting begins to increase, as shown Figure 5.9, the center of gravity location is moved insignificantly along the chord to

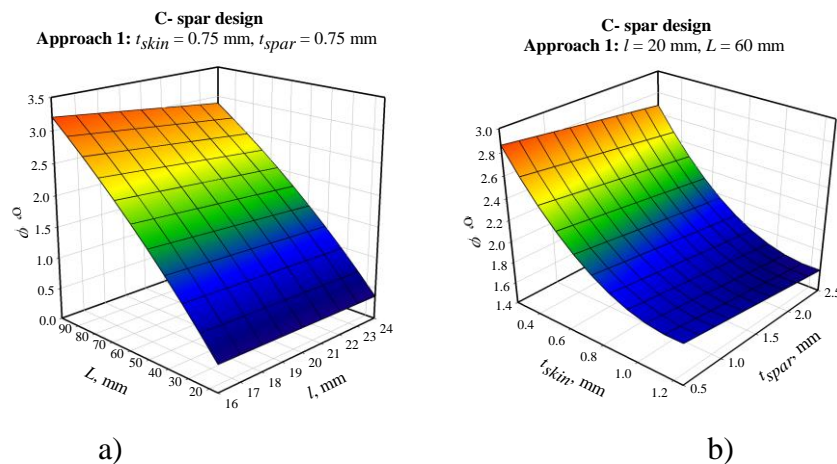
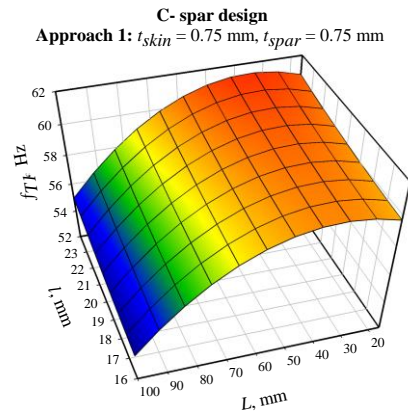
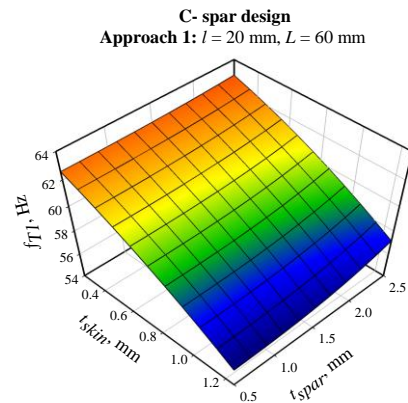


Figure 5.8. The torsion angle dependency on the design variables

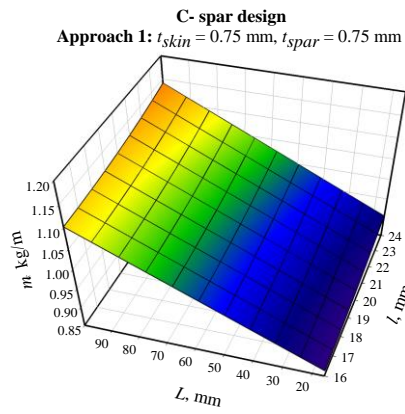


a)

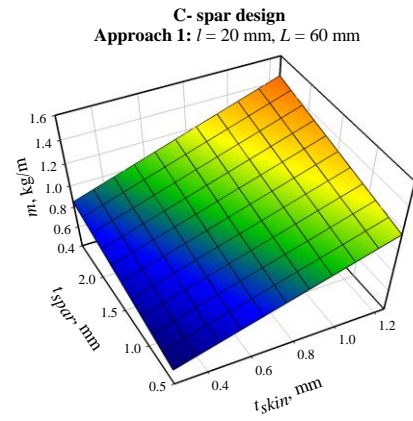


b)

Figure 5.11. The first torsional frequency dependency on the design variables

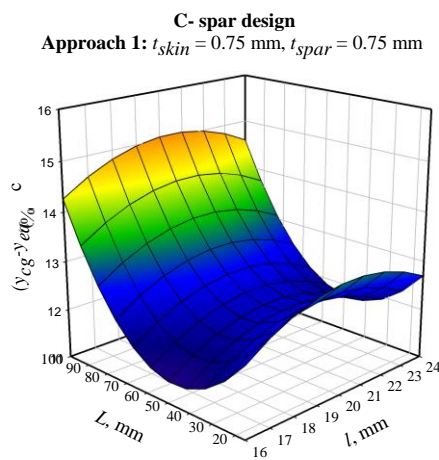


a)

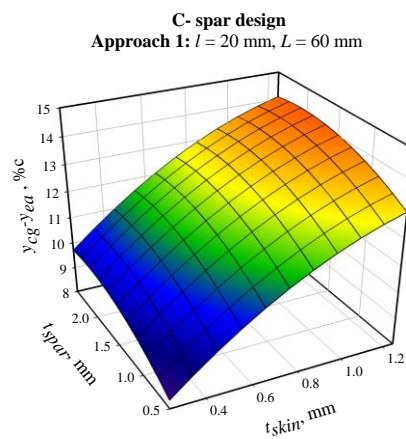


b)

Figure 5.12. The mass per unit span dependency on the design variables



a)



b)

Figure 5.13. The minimal distance between location of the centre of gravity and elastic axis dependency on the design variables

minimal distance increases with an increase of spar “moustaches” and skin thickness. An increase of MFC actuators chordwise length decreases the minimal distance upto a certain point, but then significantly increases. When the spar circular fitting begins to increase, the minimal distance between location of the centre of gravity and elastic axis initially increase upto a certain point and then decreases slightly.

5.4. Experimental verification

Comparison of torsion angles for the 3D numerical simulation and experimental test of demonstrator blade was made to confirm the modelling accuracy. The demonstrator blade were designed and manufactured in DLR [113].

The main characteristics of this demonstrator were taken from the BO 105 model rotor blade. The chord length of 121 mm is in agreement with the original, whereas the profile was slightly changed into a symmetrical NACA 0012 due to the manufacturing reasons, which did not really change the blade from a structural point of view. The demonstrator is not pretwisted and the radius of this rotor blade R_b is 1.74 m. The material properties of the rotor blade and MFC actuator are given in the Tables 2.2, 2.3 and 2.4. In the demonstrator blade, wolfram was used as a balance weight. Material properties of wolfram are given in Table 5.6.

The actuator angle chosen for the present demonstrator is $+40^\circ$, whereas the skin is made of unidirectional glass layers at an angle of -30° (Figure 5.14). To provide a good coverage with active material and to realize the desired actuation direction of $+40^\circ$, special shaped MFC actuators were designed for the demonstrator blade. In total, six MFC actuators per skin were implemented, resulting in a total active area of approximately 1600 cm² (Figure 5.15).

The blade was equipped with the sets of strain gauges. Nine sets of strain gauges are implemented into the demonstrator blade. Six sets were implemented for measurement of

Table 5.6.

Material properties: balance weight

| | Symbol | Units | Wolfram |
|-----------------|--------|----------------------|---------|
| Young’s modulus | E | [GPa] | 13.79 |
| Shear modulus | G | [GPa] | 2.00 |
| Poisson’s ratio | ν | – | 0.44 |
| Density | ρ | [kg/m ³] | 11300 |

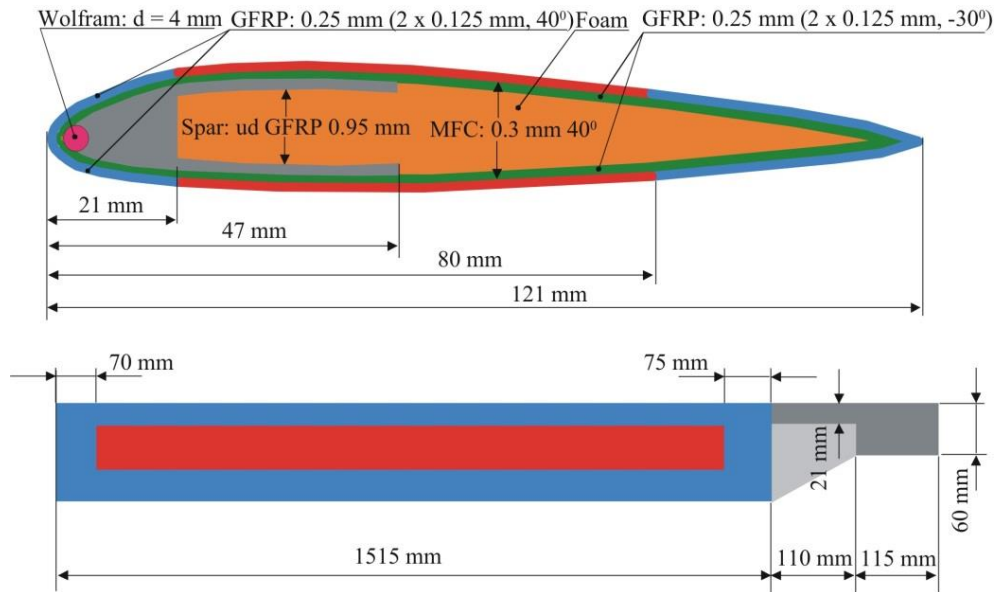


Figure 5.14. Cross section and planform of the demonstrator blade

torsion and 3 for flapping.

The strain gauges and the necessary wiring were embedded into the blade skin during the manufacturing process. For each torsion measurement point, two strain gauges were arranged on the opposite sides of the blade at angle of $\pm 45^\circ$ to measure the torsional deformation of the blade. The individual strain gauges were wired to a full bridge to compensate for any bending deformation of the blade, so that only torsional deformations were measured. As backup and to doublecheck the results of the strain gauge measurements, a complementary optical measurement system was installed. The system consists of two LED's attached at the leading- and trailing edge of the rotor blade tip and a stationary camera system with short exposure times (Figure 5.16).

Two additional acceleration sensors, mounted at the leading and trailing edges of the blade tip respectively, are used to directly measure the torsion angle because this information is not available from the strain gages measurements. Furthermore, a supplementary optical measurement system was installed as backup and to check the recordings from both the strain gages and the acceleration sensors. This system consists of a stationary high speed camera synchronized with two LEDs attached at the leading and trailing edges of the rotor blade tip.



Figure 5.15. Demonstrator blade using MFC actuators



Figure 5.16. LEDs position demonstrator blade

This system allows the visualization of the twisting movement of the blade identifying the spatial positions of the two light spots of the LEDs by properly triggering the camera.

For measurements of active twist, the demonstrator blade was mounted on the test bed in a single cantilevered condition. The actuators were driven within a voltage range of -500V to $+1300\text{V}$ with a quasi-static excitation of 0.15 Hz . Though a maximum of $+1500\text{V}$ is allowed for the MFC actuators the actuation voltage was reduced to 1300V to avoid any electrical overload. The actuators were driven with a limited voltage of 1800 V_{pp} . The tip twist is in the order of 3.93° pp . The calculated twist rate, using piezoelectric actuation model developed here, is 2.94°pp/m over the length of the MFC actuators coverage R_a .

Table 5.7 compares results of a finite element simulation developed by DLR and RTU (Riga Technical University) with experimental test. The main differences of these models are given in Table 5.8. The approach followed by DLR is based on 3D FEM modelling of a blade section using ANSYS. Foam, spar, skin and MFC actuator were modelled with SOLID45 elements. Additional balancing weight was introduced as point masses MASS21 in the spar. The piezo effect is modelled by the thermal analogy.

From Table 5.7 it can be seen that the torsion angle of the experimental result is situated between the numerical results of RTU and DLR. Difference between the experiment

Table 5.7.

Comparison of measured and calculated data

| Title | Symbol | Units | Experimental result | Numerical simulation | |
|---------------|---------------|-----------------|---------------------|----------------------|--------|
| | | | | by DLR | by RTU |
| Torsion angle | φ | $[\text{pp}]$ | 3.93 | 3.70 | 4.06 |
| Twist rate | φ/R_a | $[\text{pp/m}]$ | 2.87 | 2.70 | 2.94 |

Table 5.8.

Differences of models

| | Model by RTU | Model by DLR |
|---------------------------|------------------|----------------|
| Modelling tool | ANSYS | ANSYS |
| Model of balancing weight | Volume Modelling | Point Mass |
| Skin Modelling | Shell Elements | Solid Elements |

and simulation results of torsion angles is 5.9% for DLR and 3.2% for RTU.

The comparison of the torsion angles between the experimental test and numerical result of RTU shows that the piezoelectric actuation model adequately predicts the static actuation performance by using the thermal analogy and confirms the modelling accuracy developed by RTU.

5.5. Design Tool

Present section describes Design Tool that was produced using the methodology developed for the optimum placement of MFC actuators in the helicopter rotor blades. Four design solutions for an application of MFC actuators were used in Design Tool (Figure 5.17):

- Approach A – application of MFC actuator on the top of skin;
- Approach B – application of MFC actuator on the bottom of skin;
- Approach C – application of MFC actuator in the skin;
- Approach D – application of MFC actuator on the top and bottom of skin.

Design Tool includes four general blocks: one for the data description (Figure 5.18), two solution blocks for the analysis and optimisation (Figure 5.19 and 5.20) and one for the

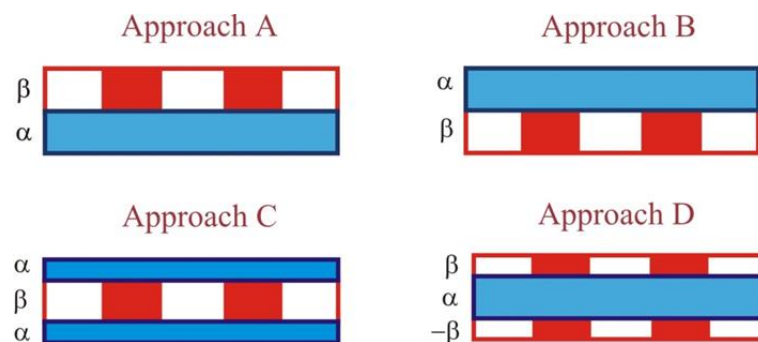


Figure 5.17. Application of MFC actuators in the Design Tool

analysis and optimisation result presentation (Figure 5.21). Data block in the Design Tool (Figure 5.18) shows geometry of helicopter rotor blade in model scale and material properties.

In the Analysis Block (Figure 5.19), user can choose one approach for an application of MFC actuators (Select approach) and can input any value from the ranges indicated by MIN MAX in the edit fields of the design parameters (Design parameters). By clicking of

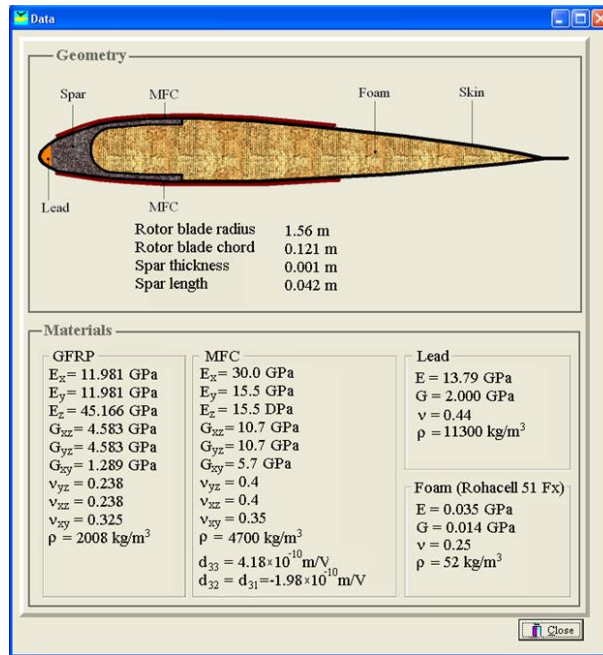


Figure 5.18. Data block in the Design Tool

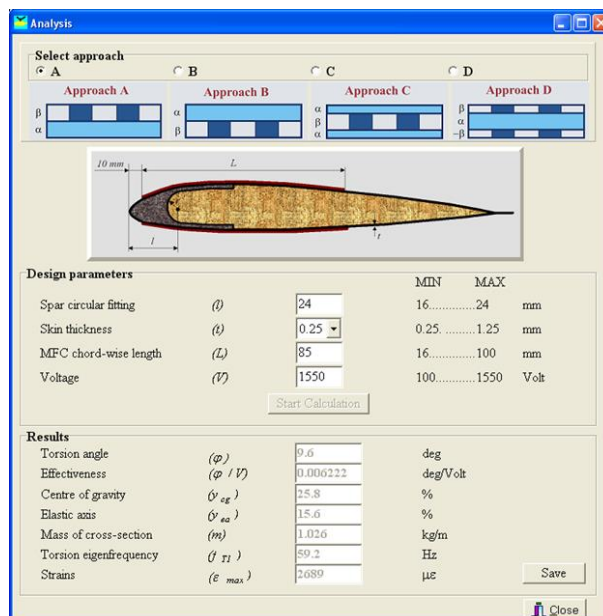


Figure 5.19. Analysis block in the Design Tool

“Start Calculation” button the appropriate characteristics are calculated and indicated in the result fields (Results). They can be written together with the chosen design parameters in the “Analysis Results Table” (Figure 5.21a) by clicking of “Save” button.

In the Optimisation Block (Figure 5.20) user can choose one approach for an application of MFC actuators and can solve an optimisation problem formulated in the left hand part of the Optimisation Block introducing the borders for the design parameters and constraints in the frames of the proposed values. “Reset” button gives the possibility to reset the design parameter and constraint ranges to their initial values.

In the right hand part of the Optimisation Block, the graphs (blue colour) of the objective function in dependence on the design parameters are given. The optimum solution obtained is indicated in the graphs by the red point. By clicking on the constraint box user can see the active constraint zone on the graphs which is coloured in appropriate colour. By positioning cursor on the graph and holding left/right mouse button, user can turn/move the image and by clicking “Copy” button user can copy last clicked graph to a clipboard. By clicking of “Reset” button user can reset the initial angles of isometric view for all graphs. Additionally, user can change the grid size in all graphs using “Grid Size” button. Sometimes for rough grid sizes, incorrect visualization of active constraints is observed. In this case, it is necessary to increase the grid size or to narrow the design space for design parameters.

The results of analysis and optimisation are written in the appropriate tables (Figure

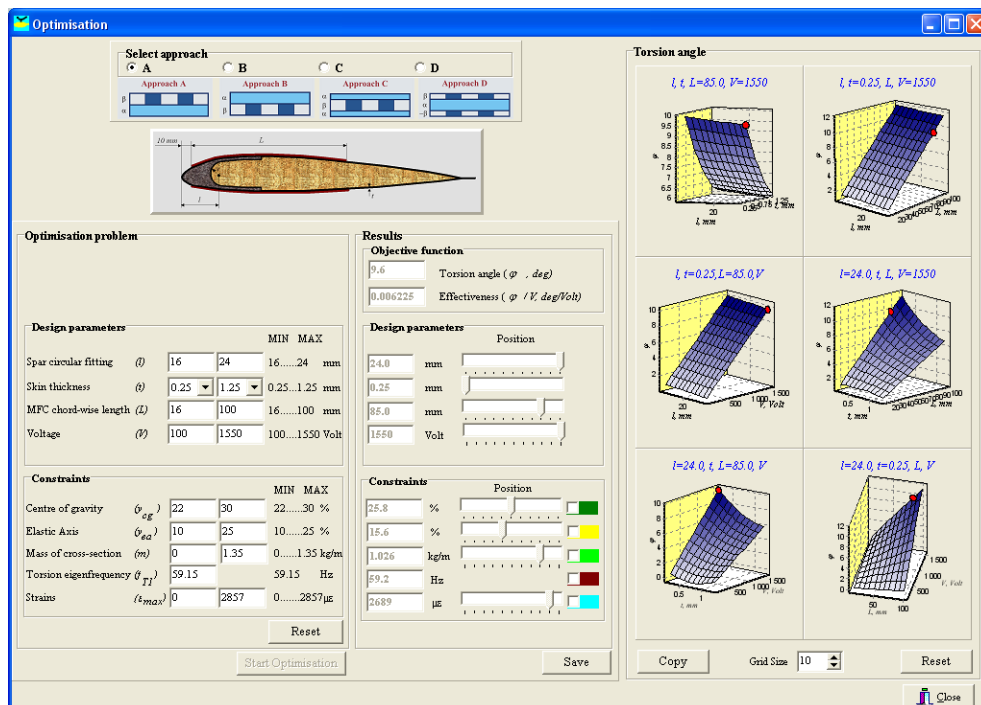


Figure 5.20. Optimisation block in the Design Tool

| Analysis # | 1 | 2 | 3 | 4 |
|-----------------------------|----------|----------|----------|----------|
| Approach | A | B | C | D |
| Spar circular fitting, mm | 240 | 16.0 | 21.9 | 240 |
| Skin thickness, mm | 0.25 | 0.25 | 0.25 | 0.25 |
| MFC chord-wise length, mm | 85.0 | 83.5 | 85.2 | 86.6 |
| Voltage, Volt | 1550 | 1414 | 1550 | 942 |
| Torsion angle, deg | 9.6 | 7.3 | 8.5 | 12.3 |
| Effectiveness, deg/Volt | 0.006222 | 0.005182 | 0.005472 | 0.013030 |
| Centre of gravity, % | 25.8 | 27.9 | 26.4 | 26.0 |
| Elastic axis, % | 15.6 | 17.5 | 15.9 | 15.9 |
| Mass of cross-section, kg/m | 1.026 | 0.861 | 0.984 | 1.031 |
| Torsion eigenfrequency, Hz | 59.2 | 59.2 | 59.2 | 59.2 |
| Stresses | 2689 | 2857 | 2837 | 2857 |

(a)

| Optimisation # | 1 | 2 | 3 | 4 |
|-----------------------------|----------|----------|----------|----------|
| Approach | A | B | C | D |
| Torsion angle, deg | 9.6 | 7.3 | 8.5 | 12.3 |
| Effectiveness, deg/Volt | 0.006225 | 0.005184 | 0.005473 | 0.013024 |
| Spar circular fitting, mm | 240 | 16.0 | 21.9 | 240 |
| Skin thickness, mm | 0.25 | 0.25 | 0.25 | 0.25 |
| MFC chord-wise length, mm | 85.0 | 83.5 | 85.2 | 86.6 |
| Voltage, Volt | 1550 | 1414 | 1550 | 942 |
| Centre of gravity, % | 25.8 | 27.9 | 26.4 | 26.0 |
| Elastic axis, % | 15.6 | 17.5 | 15.9 | 15.9 |
| Mass of cross-section, kg/m | 1.026 | 0.861 | 0.985 | 1.030 |
| Torsion eigenfrequency, Hz | 59.2 | 59.2 | 59.2 | 59.2 |
| Stresses | 2689 | 2857 | 2840 | 2857 |

(b)

Figure 5.21. Results block in the Design Tool

5.21). User can delete data of the currently selected column using "Delete Column" button or can delete all data in the table using "Clear Table" button. By clicking of "Copy to Clipboard" button user can copy result tables to Clipboard and can use them later in a Text Editor.

6. OPTIMAL DESIGN OF FULL SCALE ROTOR BLADE

This chapter presents the optimal design of the full scale rotor blade with C– spar. This blade was chosen to show further capabilities of the optimization process. The optimization results are obtained for two possible applications of MFC actuators. Before the obtaining of optimal results, the numerical upscaling problem is investigated.

6.1. Upscaling problem

Before optimisation of the full scale rotor blade, the upscaling of optimisation problem was made for the optimum placement of actuators in the model and full scale rotor blade with C– spar without root. For this purpose, some design parameters of the model scale blade, namely spar circular fitting, spar “moustaches” thickness and MFC chordwise length, are multiplied by the scale coefficient 2.67 (Table 6.1). In this connection some constraints are changed also according to the designer requirements as presented in Table 6.2. Dimensions of

Table 6.1.

Domain of interest for optimisation: model and full scale

| Title | Symbol | Units | Bounds | |
|-----------------------|------------|-------|--------------------------------|--------------------------------|
| | | | Model scale | Full scale |
| Spar circular fitting | l | [mm] | $16 \leq l \leq 24$ | $42.7 \leq l \leq 64.1$ |
| Skin thickness | t_{skin} | [mm] | $0.25 \leq t_{skin} \leq 1.25$ | $0.25 \leq t_{skin} \leq 1.25$ |
| Spar thickness | t_{spar} | [mm] | $0.50 \leq t_{spar} \leq 2.50$ | $1.34 \leq t_{spar} \leq 6.68$ |
| MFC chord–wise length | L | [mm] | $16 \leq L \leq 100$ | $42.7 \leq L \leq 267.0$ |

Table 6.2.

Minimum and maximum bounds of the constraints: model and full scale

| Title | Symbol | Units | Bounds | |
|----------------------------|----------|--------|--------------------------|--|
| | | | Model scale | Full scale |
| Centre of gravity location | y_{cg} | [%c] | $22 \leq y_{cg} \leq 30$ | $27.5 \leq y_{cg} \leq 32.5$ or $y_{cg} = 30$ |
| Elastic axis location | y_{ea} | [%c] | $10 \leq y_{ea} \leq 25$ | $10 \leq y_{ea} \leq 25$ |
| Mass per unit span length | m | [kg/m] | $m \leq 1.35$ | $m \leq 11$ |
| First torsional frequency | f_{T1} | [Hz] | $f_{T1} \geq 59.1$ | $f_{T1} \geq$ is absent or $f_{T1} \geq 21$ |

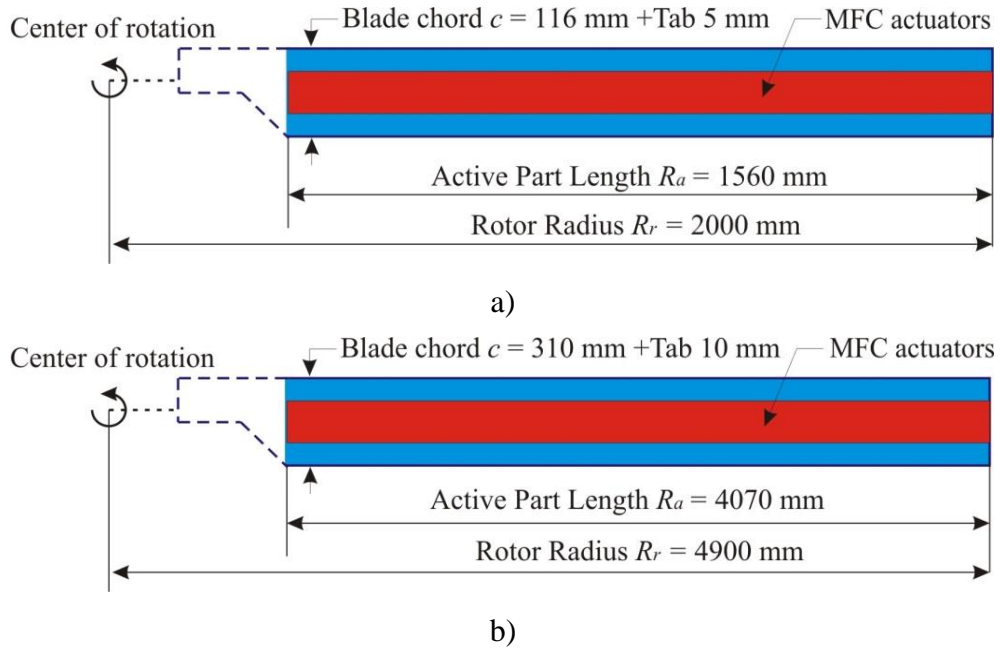


Figure 6.1. Planform of the rotor blades: (a) model scale blade, (b) full scale blade

the model scale and full scale rotor blade planforms are showed in Figure 6.1. An approach 1 was chosen for solution of upscaling problem.

The plan of experiments is formulated for 4 design parameters, namely, t_{spar} , l , t_{skin} , L and 30 experiment points. The finite element model of each blade was built, and finite element analyses were performed in 30 experiment points for each blade. The numerical results were employed to determine the approximating functions. Response surfaces for all behaviour functions were obtained with the correlation coefficients around 90% and higher. They were verified by the finite element solutions in the points different from the points taken in the plan of experiments. Non-linear optimisation problem is executed by the random search method using the determined response surfaces.

The optimal results obtained with the response surface model (RSM) for the full scale rotor blade without root and model scale are listed in Table 6.3. The actuation voltage is 1000V.

Four combinations of constraints for the full scale rotor blade were analysed. In the first optimisation case, the location of the centre of gravity was taken within the range $y_{cg} = 27.5...32.5\%c$. There was no any frequency limitation. In the second case of optimisation, the location of the centre of gravity y_{cg} is $30\%c$ and without any frequency limitation. In the third case, the location of the centre of gravity $y_{cg} = 27.5...32.5\%c$ and the first torsion frequency is more than 21.0 Hz. In the last case, the location of the centre of gravity y_{cg} is $30\%c$ and the first torsion frequency is more than 21.0 Hz. This case leads to the minimal

Table 6.3.

Optimisation results of full scale and model scale rotor blades

| Symbol/Units | Design variables | | | | Constraints | | | | Objective function |
|---|------------------|------------------|------------------|-----------|----------------|----------------|-------------|----------------|--------------------|
| | l mm | t_{skin} mm | t_{spar} mm | L mm | y_{cg} %c | y_{ea} %c | m kg/m | f_{T1} Hz | ϕ ° |
| Model scale blade | | | | | | | | | |
| $22 \leq y_{cg} \leq 30$ %c $f_{T1} \geq 59.15$ Hz | 24.0 | 0.25 | 0.50 | 91 | 26.5 | 16.3 | 0.99 | 59.2 | 3.91 |
| Full scale blade | | | | | | | | | |
| 1) $27.5 \leq y_{cg} \leq 32.5$ %c | 42.7 | 0.50 | 1.34 | 267 | 28.9 | 17.8 | 4.46 | 21.5 | 2.68 |
| 2) $y_{cg} = 30$ %c | 46.2 | 0.75 | 1.34 | 267 | 30.0 | 17.9 | 4.98 | 22.4 | 2.16 |
| 3) $27.5 \leq y_{cg} \leq 32.5$ %c $f_{T1} \geq 21.0$ Hz | 64.1 | 0.75 | 5.56 | 263 | 28.2 | 15.5 | 6.75 | 23.5 | 1.94 |
| 4) $y_{cg} = 30$ %c $f_{T1} \geq 21.0$ Hz | 52.1 | 1.00 | 3.75 | 252 | 30.0 | 17.0 | 6.20 | 23.5 | 1.70 |

value of the torsion angle for the full scale rotor blade.

From optimisation results it is seen that only the set with all constraints can be used for the upscaling of optimization problem, since only in this case the rotor blade torsion angle decreases with the coefficient of 2.3 in time, when its design parameters increases with the coefficient 2.67.

6.2. Optimisation results of full scale rotor blade

In this section, optimisation results are presented for the full scale rotor blade with two possible applications of the piezoelectric actuators.

6.2.1. Solution of optimisation problem

For a solution of the optimization problem, the plan of experiment with four parameters ($n=4$), namely, $(x) = [l, t_{skin}, t_{spar}, L]^T$ and 30 experiment points ($k=30$) were selected. Numerical values of the experimental plan for the full scale rotor blade were taken from Table 5.1 with the scale coefficient 2.67. The plans of experiments in 3D view are presented in Figure 6.2.

For an improvement of the twist actuation performance of rotor blades, two design solutions for an application of MFC actuators were used in this study (Figure 5.2): application of MFC actuator on the top of skin (approach 1) and application of MFC actuator on the top and bottom of skin (approach 2).

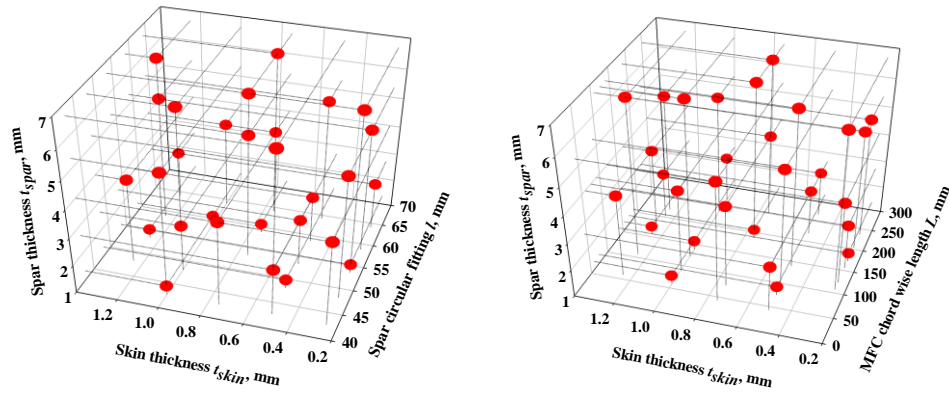


Figure 6.2. Plans of experiments: 3D-view

The finite element solutions were performed in the reference points of the plan of experiments. The numerical results were employed to obtain approximating functions. Response surfaces for all behaviour functions were obtained with the correlation coefficients around 90% and higher. The results of verification are presented in Figure 6.3, where a very good correlation is observed for the approximations and finite element solutions. Non-linear

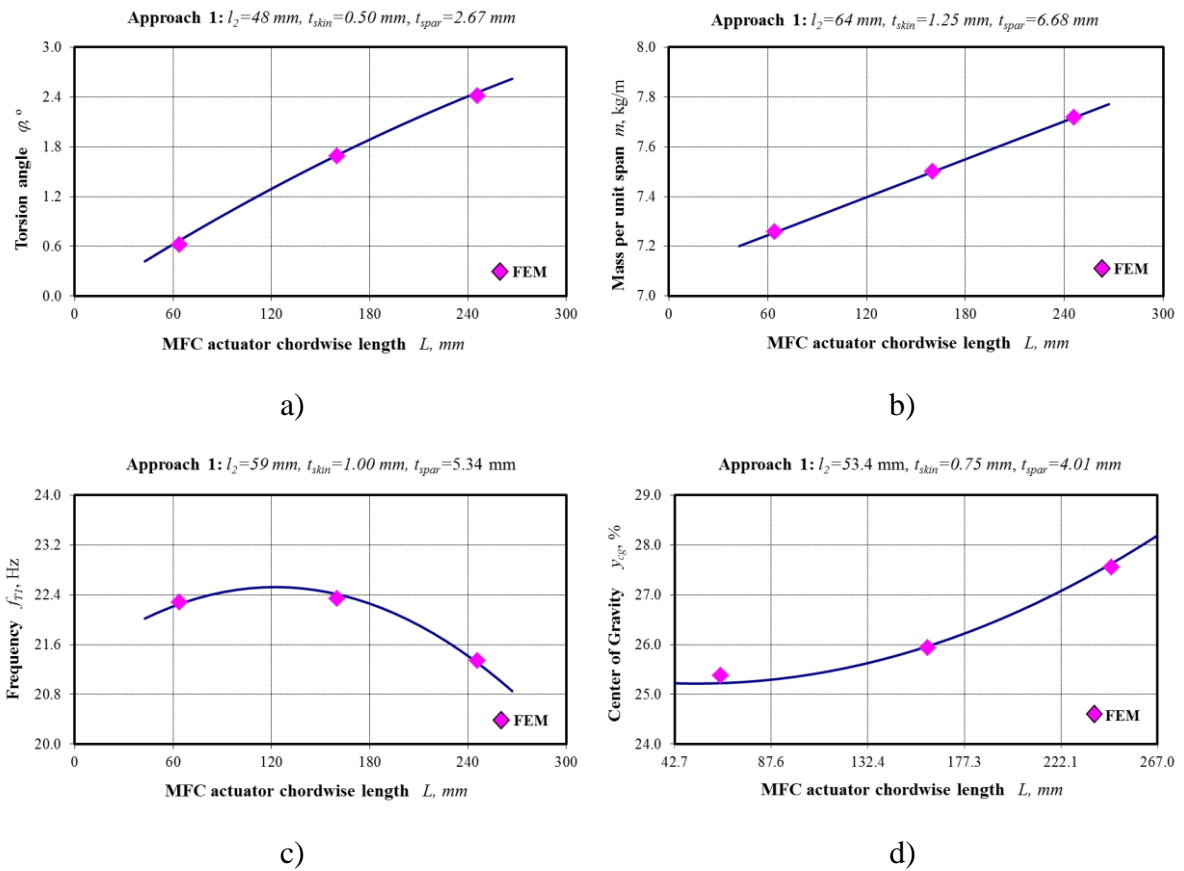


Figure 6.3. Verification of the response surfaces: (a) torsion angle, (b) mass per unit blade, (c) first torsion frequency, (d) center of gravity

optimisation problem is executed by the random search method using the obtained response surfaces.

The optimisation results obtained for the full scale rotor blade and two approaches are listed in Tables 6.4 and 6.5. The maximum torsion angle is 1.78° and 3.31° for approach 1 and approach 2 respectively, when the applied voltage is 1000 V. Using the linear interpolation of the twist angle and taking the maximum voltage of $2000V_{pp}$, the maximum torsion angles

Table 6.4.

Optimisation results of full scale rotor blade: approach 1

| | Title | Symbol | Units | RSM | FEM | Δ , % |
|--------------------|---------------------------------|------------|-----------------|-------|-------|--------------|
| Design variables | Spar circular fitting | l | [mm] | 47.7 | 47.7 | – |
| | Skin thickness | t_{skin} | [mm] | 1.0 | 1.0 | – |
| | Spar thickness | t_{spar} | [mm] | 3.7 | 3.7 | – |
| | MFC chord-wise length | L | [mm] | 258.0 | 262.0 | 1.5 |
| Constraints | Centre of gravity location | y_{cg} | [%] | 30.0 | 29.9 | 0.3 |
| | Elastic axis location | y_{ea} | [%] | 23.8 | 23.6 | 0.8 |
| | Blade mass per unit span length | m | [kg/m] | 6.1 | 6.1 | 0 |
| | First torsional frequency | f_{r1} | [Hz] | 21.1 | 21.0 | 0.5 |
| Objective function | Torsion angle | φ | [$^\circ$] | 1.78 | 1.81 | 1.7 |
| | Torsion angle | φ | [$^\circ pp$] | 3.56 | 3.62 | 1.7 |

Table 6.5.

Optimisation results of full scale rotor blade: approach 2

| | Title | Symbol | Units | RSM | FEM | Δ , % |
|--------------------|---------------------------------|------------|-----------------|------|------|--------------|
| Design variables | Spar circular fitting | l | [mm] | 42.8 | 42.8 | – |
| | Skin thickness | t_{skin} | [mm] | 0.75 | 0.75 | – |
| | Spar thickness | t_{spar} | [mm] | 4.9 | 4.9 | – |
| | MFC chord-wise length | L | [mm] | 244 | 246 | 1.5 |
| Constraints | Centre of gravity location | y_{cg} | [%] | 30.0 | 30.2 | 0.3 |
| | Elastic axis location | y_{ea} | [%] | 21.6 | 21.9 | 0.8 |
| | Blade mass per unit span length | m | [kg/m] | 6.7 | 6.7 | 0 |
| | First torsional frequency | f_{r1} | [Hz] | 21.1 | 20.9 | 0.5 |
| Objective function | Torsion angle | φ | [$^\circ$] | 3.31 | 3.35 | 1.2 |
| | Torsion angle | φ | [$^\circ pp$] | 6.62 | 6.70 | 1.2 |

reach the maximum torsion angles reach 3.56°pp and 6.62°pp .

The optimal results obtained with the response surface model (RSM) are verified by the finite element solutions (FEM). It is seen that these differences are very small. Mostly residuals do not exceed 2% that speaks about good correlation of the approximating functions.

The results show that the differences on the maximal torsion angles between two approaches achieve 46.2%. The minimal distance between location of the centre of gravity and elastic axis for the approach 1 is 6.2% and for the approach 2 is 8.4%. In this case the approach 1 is more effective than the approach 2. The blade mass per unit span length obtained for the optimal rotor blade is 6.1 kg/m for the approach 1 and is 6.7 kg/m for the approach 2. Difference between two approaches is 8.9%. It is necessary to note that the first torsion frequencies are closer to the lower bounds of constraints for both approaches.

6.2.2. Influence of the location of centre of gravity

During the upscaling problem it was observed that the torsion angle obtained with the constraint “the location of centre of gravity $30\%c$ ” is consistently lower than obtained with the constraint “the location of centre of gravity $y_{cg}=27.5\dots32.5\%$ ”. With the purpose to maximize a torsion angle, new constraints of the location of centre of gravity were studied additionally.

Optimisation results with the new constraints are given in Table 6.6 and Table 6.7. The maximum torsion angle is 2.09° and 3.92° for the approach 1 and 2 respectively. The

Table 6.6.

Optimisation results with new constraints: approach 1

| | Title | Symbol | Units | RSM | FEM | Δ , % |
|--------------------|---------------------------------|------------|--------|-------|-------|--------------|
| Design variables | Spar circular fitting | l | [mm] | 47.7 | 47.7 | – |
| | Skin thickness | t_{skin} | [mm] | 0.75 | 0.75 | – |
| | Spar thickness | t_{spar} | [mm] | 3.6 | 3.6 | – |
| | MFC chord-wise length | L | [mm] | 258.0 | 262.0 | 1.5 |
| Constraints | Centre of gravity location | y_{cg} | [%] | 28.9 | 28.8 | 0.4 |
| | Elastic axis location | y_{ea} | [%] | 22.7 | 22.3 | 1.8 |
| | Blade mass per unit span length | m | [kg/m] | 5.7 | 5.7 | 0 |
| | First torsional frequency | f_{T1} | [Hz] | 21.1 | 20.8 | 1.4 |
| Objective function | Torsion angle | φ | [°] | 2.09 | 2.09 | 0 |
| | Torsion angle | φ | [°pp] | 4.18 | 4.18 | 0 |

Table 6.7.

Optimisation results with new constraints: approach 2

| | Title | Symbol | Units | RSM | FEM | Δ , % |
|--------------------|---------------------------------|------------|--------|-------|-------|--------------|
| | Spar circular fitting | l | [mm] | 42.7 | 42.7 | – |
| Design variables | Skin thickness | t_{skin} | [mm] | 0.5 | 0.5 | – |
| | Spar thickness | t_{spar} | [mm] | 1.3 | 1.3 | – |
| | MFC chord-wise length | L | [mm] | 227.0 | 225.0 | 0.9 |
| Constraints | Centre of gravity location | y_{cg} | [%] | 28.4 | 28.5 | 0.4 |
| | Elastic axis location | y_{ea} | [%] | 22.0 | 22.8 | 3.5 |
| | Blade mass per unit span length | m | [kg/m] | 5.3 | 5.3 | 0 |
| | First torsional frequency | f_{T1} | [Hz] | 21.1 | 20.1 | 0.8 |
| Objective function | Torsion angle | φ | [°] | 3.92 | 3.97 | 1.3 |
| | Torsion angle | φ | [°pp] | 7.84 | 7.94 | 1.3 |

applied voltage is 1000 V. The differences between the optimal and numerical results do not exceed 3.5% that shows a good correlation of the approximating functions.

The optimal results with new constraints show that the difference on the maximal torsion angle between two approaches is 46.7%. The minimal distance between location of the centre of gravity and elastic axis is approximately the same for both approaches. The blade mass per unit span length is 5.7 kg/m for the approach 1 and 5.3 kg/m for the approach 2. Difference between two approaches in this case is 7.0%.

The comparative study of optimal results obtained for the full scale rotor blade with different constraints shows that the new constraints on the location of centre of gravity increases the torsion angle (14.8% for the approach 1 and 15.6% for the approach 2) and decreases the blade mass per unit span length (6.6% for the approach 1 and 20.8% for the approach 2). The minimal distance between the location of the centre of gravity and elastic axis saves the same for both approaches. The obtained results demonstrate that the new constraints are more effective.

6.2.3. Optimal operating voltage

For an individual blade control, the twist actuation amplitude of approximately $\pm 2^\circ$ is generally required as the minimum level of performance needed from the piezoelectric actuation. This level of actuation shows a good possibility for a vibration reduction [119].

Figure 6.4 shows the relationship between the torsion angle and the required input voltage. As one can see, to obtain the target actuation of $\pm 2^\circ$, the optimal rotor blades require different voltage for different approaches (Table 6.8). It is seen that the approach 2 has more capability to reduce the vibration of helicopter with a much lower input voltage than the approach 1.

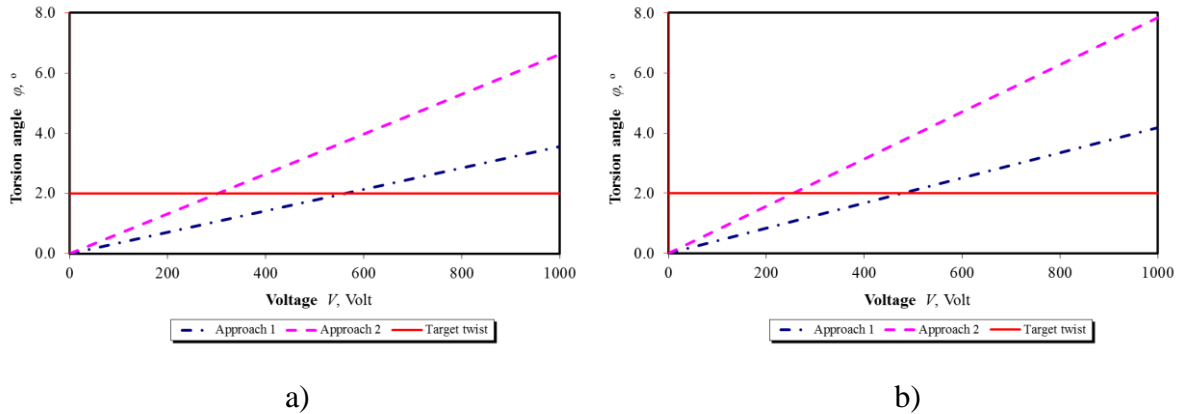


Figure 6.4. Minimized input voltage for the Approach 1 and Approach 2:
 (a) $y_{cg} = 30\%c$, (b) $27.5\% \leq y_{cg} \leq 32.5\%c$

Table 6.8.

Piezoelectric actuation

| Title | | φ , °pp | V, Volt |
|-----------------------------------|------------|-----------------|---------|
| $y_{cg} = 30\%c$ | Approach 1 | 3.56 | 555 |
| | Approach 2 | 6.62 | 303 |
| $27.5\% \leq y_{cg} \leq 32.5\%c$ | Approach 1 | 4.18 | 476 |
| | Approach 2 | 7.84 | 256 |

7. CONCLUSIONS

The present investigations were carried out to develop new modelling and optimisation methodology for the design of helicopter rotor blades with an active twist to enhance its capability for the vibration and noise reduction. 3D finite element models of the helicopter rotor blades in the model and full scales were built according to the producer's requirements. The finite element model of helicopter rotor blade was validated by using the results of static twist experiment. New optimal solutions were performed for the rotor blades with C- and D-spars in the model and full scales and two possible applications of the piezoelectric actuators. The following general conclusions can be drawn based on the results presented in the thesis:

1. To perform the finite element analysis, new realistic 3D finite element model of the helicopter rotor blades with skin of the rotor blade and Macro Fibre Composite actuators modelled by the linear layered structural shell elements was created. To activate a piezoelectric effect in this model, the thermal analogy was used. This simplification gave the possibility to decrease the dimension of the finite element model and considerably reduce the time of calculations. Preliminary work was done to demonstrate an application of the thermal analogy for the modelling of static and dynamic behaviour of simple piezoelectric structures. To start calculations, more attention was paid to a convergence of the finite element results due to the complexity of structure analyzed and large differences (factors greater than 1000) between Young and shear moduli of different rotor blade components.
2. To formulate an optimisation problem, the parametric study of the rotor blades with C- and D-spars in the model scale was carried out with the purpose to decrease the number of design parameters and by this way to increase the accuracy of the optimal results obtained. The influence of spar geometry, skin lay-up, position and size of actuators on the torsion angle, location of centre of gravity and elastic axis, blade mass per unit span, first torsion eigenfrequency and strains were studied. The parametric study shown that the spar "moustaches" length has the smallest influence on the torsion angle for the rotor blade with C-spar (less than 5%), and that the spar "moustaches" length and web thickness has the smallest influence on the torsion angle for the rotor blade with D-spar (less than 5%). The largest influence on the torsion angle in comparison with other design parameters was demonstrated by the skin

thickness and MFC actuator chordwise length. Moreover, it was established that the calculated strains are considerably lower than permissible value.

3. According to the results of the parametric study, four design variables were chosen for the solution of optimisation problems in the rotor blades with C- and D- spars in the model scale. The constraints on the chordwise locations of the cross-sectional center of gravity and elastic axis were taken into account for an aeroelastic stability. To improve an active control of the rotor blades, the minimal distance between the center of gravity and elastic axis becomes an important parameter also in the design. The constraints on the blade mass per unit span length and first torsional frequency of the blade are accounted for a desirable blade dynamics. For an improvement of the twist actuation performance of the rotor blades with C- and D- spars, two design solutions for an application of MFC actuators were used in this study: an application of MFC actuators on the top of skin (approach 1), and on the top and bottom of skin (approach 2). From the optimisation results, it was found that the D- and C-spars have approximately the same results on maximal torsion angle for two approaches. However, the minimal distance between the centre of gravity and elastic axis demonstrates that D-spar is more effective, especially for the first approach. Parametric study by the response surfaces were carried out additionally for a designer convenience to investigate an influence of different design parameters on the behaviour functions.
4. To confirm the modelling accuracy, a comparison of the torsion angles between 3D numerical simulation and experimental test of the demonstrator blade was made. The demonstrator blade was designed and manufactured in DLR. The results of validation study show that the developed 3D finite element model based on the thermal analogy with a high accuracy predicts the static actuation performance of the helicopter rotor blades.
5. Taking into account the present design methodology, the Design Tool for the optimum placement of MFC actuators in the helicopter rotor blades was developed for the aerospace engineers. Four design solutions for an application of MFC actuators were implemented into Design Tool.
6. The optimal design of the full scale rotor blade with C- spar was executed additionally to show the further capabilities of the developed optimization methodology. Before the obtaining of optimal results, the numerical upscaling problem with four combinations of the constraints for the full scale rotor blade was investigated. The optimisation

results show that an upscaling can be applied only when all the constraints in the optimisation problem for the full scale helicopter rotor blade are taken into consideration. For an improvement of the twist actuation performance of the rotor blades, two design solutions for an application of MFC actuators were analysed. The optimal configuration of the full scale rotor blade was found for the twist actuation amplitude of $\pm 2^\circ$ required for an effective noise and vibration reduction in the future helicopters.

The results of this thesis are the part of the collaborative European project “Integration of technologies in support of a passenger and environmentally friendly helicopter” (FRIENDCOPTER) under FRAMEWORK 6 program. The main aim of the project was to obtain environmentally friendly helicopters with the lowering of impulsive exterior noise, of excessive cabin vibrations and of high fuel consumption by an active blade control. The researcher data obtained from the investigations are intended for the most experienced European companies, research institutes and academic institutions working in the field of helicopter rotor blade design. The development of new modelling and optimisation methodologies for the design of rotor blades with an active twist will allow a further expansion of investigations in this field.

For the future research and design studies, the number of the design variables accounting for the optimisation problem could be increased according to the future design requirements as well as new engineering approaches developed for an active control of helicopter rotor blades could be analysed and optimised.

REFERENCES

- [1] Alik H. and Hughes T. J. R. *Finite element method for piezoelectric vibration // International Journal for Numerical methods in Engineering.* – 1970. – Vol.2. – pp. 151–157.
- [2] Altmikus A. A. and Bailly B. J. *Reference Rotor, Deliverable No. D5.1–2, 20.07.07*
- [3] Antony J. *Design of experiments for engineers and scientists.* – Butterworth–Heinemann, United Kingdom, 2003. – 190 p.
- [4] ANSYS, Inc. (2004). *ANSYS User’s Manual*
- [5] Audze P., Eglais V. *New approach to planning out of experiments // Problems of dynamics and strength.* – 1977. – Vol.35. – pp. 104–107. (in Russian)
- [6] Auzins, J. *Direct Optimisation of Experimental Designs // Proceedings of the 10th AIAA/ISSMO Multidisciplinary Analysis and Optimisation.* – Albany, USA. – 2004. – Vol.274578. – 12 P.
- [7] Bent A.A. and Hagood N.W. *Anisotropic actuation with piezoelectric fiber composites // Journal of Intelligent Material Systems and Structures.* – 1995. – Vol.6(3). – pp. 338 – 349.
- [8] Booker A.J. *Design and Analysis of Computer Experiment // Proceedings of the 7AIAA/USAF/NASA/ISSMO Symposium on Multidisciplinary Analysis & Optimisation.* – St. Louis, USA, 1998. – pp. 239–245.
- [9] Box G.E.P., Draper N.R. *On minimum–point second–order designs// Technometrics.* – 1974. – Vol.16. – pp. 613–616.
- [10] Brockmann T. H. and Lammering R. *Beam Finite Elements for Rotating Piezoelectric Fiber Composite Structures // Journal of Intelligent Material Systems and Structures.* – 2006. – Vol.17. – pp. 431–448.
- [11] Buter A. and Breitbach E. *Adaptive Blade Twist –Calculations and Experimental Results // Aerospace Science and Technology.* – 2000. – Vol.4(5). – pp. 309–319.
- [12] Carrera E., Brischetto S., Nali P. *Plates and Shells for Smart Structures Classical and Advanced Theories for Modelling and Analysis.* – John Wiley & Sons, West Sussex, 2011. – 322 p.
- [13] Celi R. *Recent Applications of Design Optimisation to Rotorcraft – A survey // Journal of Aircraft.* – 1999. – Vol.36(1). – pp. 176 – 189.
- [14] Cesnik C.E.S. and Shin S.J. *On the Twist Performnce of a Multiple–Cell Active Helicopter Blade // Smart Materials and Structures.* – 2001. – Vol.10(1). – pp. 53 – 61.
- [15] Cesnik C.E.S. and Shin S.J. *On the Modelling of Integrally Actuated Helicopter Blades // International Journal Solids Structures.* – 2001. – Vol.38(10–13). – pp. 1765 – 1789.
- [16] Cesnik C.E.S. and Shin S.J. *Control of integral twist–actuated helicopter blades for vibration reduction // Proceedings of the 58th Annual Forum of the American Helicopter Society, Montreal: Canada, 2002.* – 12 P.
- [17] Cesnik C.E.S., Shin S. *Dynamic Response of Active Twist Rotor Blades // Smart Materials and Structures.* – 2001. – Vol.10(1). – pp. 62 – 76.

- [18] Cesnik C.E.S., Mok J., Parekh A. and Shin S. *Optimisation Design Framework for Integrally Twisted Helicopter Blades // Proceedings of the 45th AIAA/ASME/ASCE/ASC Structures, Structural Dynamics and Materials Conference. – Palm Springs, USA, 2004. – 10P.*
- [19] Cesnik C.E.S., Mok J., Morillo J.A. and Parikh A.S. *Design Optimisation of Active Twist Rotor Blades // Proceedings of the 30th European Rotorcraft Forum. – Marseille, France, 2004. – 14 P.*
- [20] Cesnik C.E.S., Park R.S. and Palacios R. *Effective Cross section Distribution of Anisotropic Piezocomposite Actuators for Wing twist // Proceedings of the Smart Structures and Materials: Smart Structures and Integrated Systems, SPIE. – San Diego, USA, 2003. – Vol. 5056. – pp. 21–32.*
- [21] Chattopadhyay A., Lin Q. and Gu H. *Vibration Reduction in Rotor Blades Using Active Composite Box Beam // Journal of American Institute of Aeronautics and Astronautics. – 2000. – Vol.38(7). – pp. 1125 – 1131.*
- [22] Chattopadhyay A., Lin Q. and Gu H. *Modelling of Smart Composite Box Beams with Nonlinear Induced Strain // Composite Part B: Engineering. – 1999. – Vol.30(6). – pp. 603 – 612.*
- [23] Chen P. *Development of a smart rotor with induced–strain actuation of blade twist. PhD thesis. – Baltimore: University of Maryland, 1996.*
- [24] Chen P. and Chopra I. *Induced Strain Actuation of Composite Beams and Rotor Blades with Embedded Piezoceramic Elements // Smart Materials and Structures. – 1996. – Vol.5(1). – pp. 35 – 48.*
- [25] Chen P.C., Baeder J.D., Evans R.A.D. and Niemczuk, J. *Blade–Vortex Interaction Noise Reduction with Active Twist Smart Rotor Technology // Smart Materials and Structures. – 2001. – Vol.10(1). – pp.77–85.*
- [26] Chen P. and Chopra I. *Hover Testing of Smart rotor with Induced–Strain Actuation of Blade Twist // Journal of American Institute of Aeronautics and Astronautics. – 1997. – Vol.35(1). – pp. 6 – 16.*
- [27] Chen P. and Chopra I. *Wind Tunnel Test of a Smart Rotor Model with Individual Blade Twist Control // Journal of Intelligent Material Systems and Structures. – 1997. – Vol.8(5). – pp. 414 – 423.*
- [28] Chopra I. *Review of State of Art of Smart Structures and Integrated Systems // AIAA Journal. – 2002. – Vol.40(11). –pp. 2145–2187.*
- [29] Chopra I. *Status of application of smart structures technology to rotorcraft systems // Journal of the American Helicopter Society. – 2000. – Vol.45(4). – pp. 228 – 252.*
- [30] Chopra I. and Sirohi J. *Smart Structures Theory. – Cambridge, New York, 2013. – 905 p.*
- [31] Cook R.D. and others. *Concepts and Applications of Finite Element Analysis. – John Wiley & Sons, New York, 2002. – 733 p.*
- [32] Deb K. *Optimisation for Engineering Design: Algorithms and Examples. – PHI PHI Learning Pvt. Ltd, 2012. – 440 p.*
- [33] Edgar F.T. Himmelblau D.M. and Lasdon L.S. *Optimisation of chemical processes. – McGraw-Hill, New York, 2001. – 651 p.*

- [34] *Eglais V. Approximation of data by multi-dimensional equation of regression// Problems of dynamics and strength. – 1981. – Vol.39. – pp. 120–125. (in Russian)*
- [35] *Eenkl B., Kloppel V. and Preibler D. Full Scale Rotor with Piezoelectric Actuated Blade Flaps // Proceedings of the 28th European Rotorcraft Forum. – Bristol, United Kingdom, 2002. – 18 P.*
- [36] *Friedmann P.P. Helicopter Vibration Reduction Using Structural Optimisation with Aeroelastic/Multidisciplinary Constraints // Journal of Aircraft. – 1991. – Vol.28(1). – pp. 8 – 21.*
- [37] *FRIENDCOPTER – Integration of technologies in support of a passenger and environmentally friendly helicopter.*
- [38] *Fulton M.V. and Ormiston R. Hover Testing of a Small Scale Rotor with On-blade Elevons // Journal of American Helicopter Society. – 2001. – Vol.46(2). – pp. 96 – 106.*
- [39] *Ganguli R. Survey of Recent Developments in Rotorcraft Design Optimisation // Journal of Aircraft. – 2004. – Vol.41(3). – pp. 493 – 507.*
- [40] *Ghiringhelli G.L., Masarati P. and Mantegazza P. Analysis of an Actively Twisted Rotor by Multi-body Global Modelling // Composite Structures. – 2001. – Vol.52(1). – pp. 113–122.*
- [41] *Ghiringhelli G. L., Masarati P. and Mantegazza P. Characterisation of Anisotropic, Non-Homogeneous Beam Sections with Embedded Piezo-Electric Materials // Journal of Intelligent Material Systems and Structures. – 1997. – Vol.8(10). – pp. 842–858.*
- [42] *Giurgiutiu V. Review of Smart-Materials Actuation Solutions for Aeroelastic and Vibration Control Journal of Intelligent Material Systems and Structures. – 2000. – Vol.11. – pp. 525–544.*
- [43] *Ham N.D. A Simple System for Helicopter Individual Blade Control Using Modal Decomposition // Vertica. – 1980. – Vol.4. – pp. 23 – 28.*
- [44] *Ham N.D. Helicopter Individual-Blade-Control and Its Applications // Proceedings of the 39th AHS Forum. – St. Louis, USA, 1983. – pp. 613–623.*
- [45] *Ham N.D. Helicopter Individual-Blade-Control Research at MIT 1977–1985 // Vertica. – 1987. – Vol.11(1/2). – pp. 109 – 122.*
- [46] *Hammond C.E. Wind Tunnel Results Showing Rotor Vibratory Loads Reduction Using Higher Harmonic Blade Pitch // Journal of the American Helicopter Society. – 1983. – Vol.28(1). – pp. 10 – 15.*
- [47] *Hagood N., Kindel R., Ghandi K. and Gaudenzi P. Improving Transverse Actuation of Piezoceramics Using Interdigitated Surface Electrodes // Proceedings of the Smart Structures and Materials: Smart Structures and Intelligent Systems, SPIE. – Bellingham, USA: 1993. – Vol.1917. – pp. 341 – 351.*
- [48] *Hardin R.H., Sloane N.J.A. A new approach to the construction of optimal designs// Journal of statistical planning and inference. – 1993. – Vol.37. – pp. 339–369.*
- [49] *IEEE Standard on Piezoelectricity. – New York, 1988 – 54 p.*
- [50] *Jacklin S.A., Nguyen K.Q., Blass A. and Richter P. Full-Scale Wind Tunnel Test of a Helicopter Individual Blade Control System // Proceedings of the 50th Annual Forum of the American Helicopter Society. – Washington, USA, 1994. – pp. 579–596.*

- [51] Jacklin S.A., Blass A., Teves D. and Kube R. *Reduction of Helicopter BVI Noise, Vibration and Power Consumption through Individual Blade Control // Proceedings of the 51st Annual Forum of the American Helicopter Society. – Fort Worth, USA, 1995. – pp. 662–680.*
- [52] Jacklin S.A., Blass A., Swanson S.M. and Teves D. *Second Test of a Helicopter Individual Blade Control System in the NASA Ames 40– by 80–foot Wind Tunnel // Proceedings of the International Aeromechanics Specialists' Conference. – Bridgeport, USA, 1995. – pp. 7.9–7.26.*
- [53] Janushevskis A., Akinfiyev T., Auzins J. and Boyko A. *A Comparative Analysis of Global Search Procedures // Proceedings of the Estonian Academy of Sciences, Engineering. – 2004. – Vol.10(4). – pp. 236–250.*
- [54] Jin R., Chen W. and Simpson T. W. *Comparative Studies of Metamodelling Techniques under Multiple Modelling Criteria // Structural and Multidisciplinary. – 2001. – Vol.23. – 13P.*
- [55] Johnson W. // *Helicopter Theory. – Dover Publications, New Jersey, 1994. – 1089 p.*
- [56] Johnson W. // *CAMRAD-II Comprehensive Analytical Model of Rotor Aerodynamics and Dynamics. – Johnson Aeronautics, Volume II: User's Manual.*
- [57] Kessler C. *Active Rotor Control for Helicopters: Individual Blade Control and Swashplateless Rotor Designs // CEAS Aeronautical Journal. – 2011. – Vol. 1(1–4). – pp. 23 – 54.*
- [58] Kim J.S. *Design and Analysis of Rotor Systems with Multiple Trailing Edge Flaps and Resonant Actuators. PhD thesis. – Pennsylvania: Pennsylvania State University, 2005.*
- [59] Koratkar N. and Chopra I. *Closed-loop wind tunnel testing of a smart rotor model with trailing edge flaps // Journal of American Helicopter Society. – 2002. – Vol.47(4). – pp. 263 – 272.*
- [60] Kovalovs A., Gluhihs S. *Reduction of the vibration in helicopter blade due to piezoelectric actuators // Aviation. – 2006. – Vol. 10(2). – pp. 3 – 6.*
- [61] Kovalovs A., Barkanov E., Gluhihs S. *Active vibration control of plate with piezoelectric actuators // Latvian Journal of Physics and Technical Science. – 2006. – Vol. 4. – pp. 49 – 54.*
- [62] Kovalovs A., Barkanov E., Gluhihs S. *Active control of structures using Macro-Fiber Composite (MFC) // Journal of Physics: Conference Series. – 2007. – Vol. 93(1). – pp. 3 – 9.*
- [63] Kovalovs A., Wesolowski M., Barkanov E., Gluhihs S. *Application of Macro-fiber composite (MFC) as piezoelectric actuator // Journal of Vibroengineering. – 2009. – Vol. 11(1). – pp. 105 – 112.*
- [64] Kube R., Van Der Wall B.G. *IBC Effects on BVI noise and Vibrations –A Combined numerical and Experimental Investigation // Proceedings of the 55th International Annual Forum of the American Helicopter Society. – Montreal, Canada, 1999. – pp. 2282–2291.*
- [65] Kumar D. *Design and Analysis of Composite Rotor Blades for Active/Passive Vibration Reduction. PhD thesis. – Ann Arbor: University of Michigan, 2013.*
- [66] Loewy R.G. *Helicopter Vibrations: A Technological Perspective // Journal of American Helicopter Society. – 1984. – Vol.29(4). – pp. 4 – 30.*

- [67] Masarati P., Morandini M., Riemenschneider J., Wierach P., Gluhik S., Barkanov E. *Optimal design of an active twist 1:2.5 scale rotor blade // Proceeding of the 31st European Rotorcraft Forum.* – Florence, Italy, 2005. – 14 P.
- [68] Milgram J.H., Chopra I. and Straub F.K. *Rotors with Trailing Edge Flap: Analysis and Comparison with Experimental Data // Journal of American Helicopter Society.* – 1998. – Vol.43(4). – pp. 319 – 332.
- [69] Monner H. P., Opitz S., Riemenschneider J. and Wierach P. *Evolution of Active Twist Rotor Designs at DLR // Proceeding of the 49th AIAA/ASME/ASCE/AHS/ASC Structures, Structural Dynamics and Materials Conference.* – Schaumburg, USA, 2008. – 10 P.
- [70] Monner H.P., Wierach P. *Overview of smart-structures technology at the German Aerospace Center // Proceedings of the 10th German-American Frontiers of Engineering Symposium.* – Hamburg, Germany, 2007. – 19 P.
- [71] Myers R.H., Montgomery D.C. *Response surface methodology: Process and product optimisation using designed experiments.* – John Wiley & Sons, New York, 1976. – 714 p.
- [72] Narjan S.Rau *Optimisation Principles: Practical Applications to the Operation and Markets of the Electric Power Industry.* – John Wiley & Sons, New York, 2003. – 360 p.
- [73] Nguyen K., Betzina M. and Kitaplioglu C. *Full-Scale Demonstration of Higher Harmonic Control for Noise and Vibration Reduction on the XV-15 Rotor // Journal of the American Helicopter Society.* – 2001. – Vol.46(3). – pp. 182 – 191.
- [74] Nguyen K. and Chopra I. *Application of Higher Harmonic Control to Rotors Operating at High Speed and Thrust // Journal of the American Helicopter Society.* – 1990. – Vol.35(3). – pp. 78 – 79.
- [75] Nguyen K. and Chopra I. *Effects of Higher Harmonic Control (HHC) on performance and control loads // Journal of Aircraft.* – 1999. – Vol.29(3). – pp. 336 – 342.
- [76] Park J.S. *Optimal Latin-hypercube designs for computer experiments// Journal of statistical planning and inference.* – 1994. – Vol.39(1). – pp. 95–111.
- [77] Park J.S. and Shin S.J. *A preliminary design on the second generation integral twist-actuated blade // Proceedings of the International Conference on Computational & Experimental Engineering and Sciences.* – 2007. – Vol.4(4). – pp. 265–269.
- [78] Park J.S., Shin S.J. and Kim D.K. *Design and vibratory loads reduction analysis of advanced active twist rotor blades incorporating single crystal piezoelectric fiber composites // International Journal Aeronautical and Space Sciences.* – 2008. – Vol.9(2). – pp. 18–33.
- [79] Payne P.R. *Higher Harmonic Control // Aircraft Engineering.* – 1958. – Vol.30(354). – pp. 222 – 226.
- [80] Reichert G. *Helicopter Vibration Control: A survey // Vertica.* – 1981. – Vol.5(1). – pp. 1 – 20.
- [81] Riemenschneider J., Keye S., Wierach P. and Mercier des Rochettes H. *Overview of the Common DLR/ONERA Project 'Active Twist Blade' // Proceeding of the 30th European Rotorcraft Forum.* – Marseille, France, 2004. – 9 P.
- [82] Riemenschneider J. and Opitz S. *Measurement of twist deflection in active twist rotor // Aerospace Science and Technology.* – 2011. – Vol.15(3). – pp. 216 – 223.

- [83] Riemenschneider J., Opitz S., Schulz M. and Plaßmeier V. *Active Twist Rotor for Wind Tunnel Investigations // Proceeding of the Conference on Smart Materials, Adaptive Structures and Intelligent Systems.* – 2010. – Vol.2. – pp. 371 – 378.
- [84] Riemenschneider J., Wierach P. and Keye S. *Preliminary Study on Structural properties of Active Twist Blades // Proceeding of the 29th European Rotorcraft Forum.* – Friedrichshafen, Germany, 2003. – 12 P.
- [85] Rikards R, A. K. Bledzki, V. Eglajs, A. Cate, K. Kurek. *Elaboration of optimal design models for composite materials from data of experiments // Mechanics of Composite Materials.* – 1992. – Vol.28(4). – pp. 295 – 304.
- [86] Rikards R. *Elaboration of optimal design models for objects from data of experiments // Proceedings of the IUTAM Symposium: Optimal design with advanced materials.* – Lungby: Denmark, 1993. – pp. 148–162.
- [87] Rikards R., Chate A., Bäcklund J. *Optimal design of sandwich plates based on planning of experiments// Proceedings of the 1st World congress of structural and multidisciplinary optimisation.* – Goslar, Germany, 1995. – pp. 569–574.
- [88] Rikards R., Chate A., *Optimal design of sandwich and laminated composite plates based on planing of experiments// Structural optimisation.* – 1995. – Vol.10(1). – pp. 46–53.
- [89] Rodgers J. *Development of an integral twist actuated rotor blade for individual blade control. PhD thesis.* – Cambridge: Massachusetts Institute of Technology, 1998
- [90] Rodgers J.P. and Hagood N.W. *Design, Manufacture, and Testing of an Integral Twist–Actuated Rotor Blade // 8th International Conference on Adaptive Structures and Technology.* – Wakayama, Japan, 1997. – 13 P.
- [91] Rodgers J.P. and Hagood N.W. *Preliminary Mach–scale hover testing of an integral twist–actuated rotor blade // Proceedings of the SPIE North American Symposium on Smart Structures and Materials.* – San Diego, USA, 1998. – 16 P.
- [92] Rodgers J. and Hagood N. *Hover Testing of a 1/6th Mach–Scaled CH–47D Blade with Integrated Twist Actuation // Proceedings of the 9th International Conference on Adaptive Structures and Technology.* – Cambridge, USA, 1998. – 13 P.
- [93] Sacks J., Welch W.J., Mitchell T.J., Wynn H.P. *Design and analysis of computer experiments// Statistical science.* – 1989. – Vol.4(4). – pp. 409–435.
- [94] Sekula M.K, Wilbur M.L. *Optimisation of an Active Twist Rotor Blade Planform for Improved Active Response and Forward Flight Performance // NASA Technical Reports Server (NTRS).* – 2014. – 13 P.
- [95] Sekula M.K, Wilbur M.L. and Yeager W. T. *Aerodynamic Design Study of an Advanced Active Twist Rotor // Proceedings of the American Helicopter Society 4th Decennial Specialist Conference on Aeromechanics.* – California, USA, 2004. – 12P.
- [96] Sekula M.K, Wilbur M.L. and Yeager W. T. *A Parametric Study of the Structural design of an Advanced Active Twist Rotor // Proceedings of the 61st International Annual Forum of the American Helicopter Society.* – Grapevine, USA, 2005. – 14P.
- [97] Shaw J., Albion N., Hanker E.J. and Teal R.S. *Higher Harmonic Control: Wind Tunnel Demonstration of Fully Effective Vibratory Hub Forces Suppression // Journal of the American Helicopter Society.* – 1989. – Vol.34(1). – pp. 14 – 25.

- [98] Shin S. J. *Integral Twisted Actuation of Helicopter Rotor Blades for Vibration Reduction*. PhD thesis. – Cambridge: Massachusetts Institute of Technology, 2001.
- [99] Shin S., Cesnik C.E.S. and Hall S.R. *Design and Simulation of Integral Twist Control for Helicopter Vibration Reduction // International Journal of Control, Automation, and Systems*. – 2007. – Vol.5(1). – pp. 24 – 34.
- [100] Shin S., Cesnik C.E.S., Wilkie W.K. and Wilbur M.L. *Design and Manufacturing of a Model-scale Active Twist Rotor Prototype Blade // Journal of Intelligent Material Systems and Structures*. – 2008. – Vol.19(12). –pp. 1443–1456.
- [101] Shin S, Cesnik C.E.S. and Hall S.R. *Closed Loop Control Test of the NASA/Army/MIT Active Twist Rotor for Vibration Reduction // Journal of American Helicopter Society*. – 2005. – Vol.50(2). – pp. 178 – 194.
- [102] Straub F.K. and Byrns E.V. *Application of Higher Harmonic Blade Feathering on the OH-6A Helicopter for Vibration Reduction // NASA Technical report*. – 1986. – 190 P.
- [103] Straub F. *Whirl Tower Test of the SMART Active Flap Rotor // AHS 4th Decennial Specialist's Conference on Aeromechanics*. – San-Francisko, USA, 2004. – 20 P.
- [104] Straub F.K. and Hassan A.A. *Aeromechanic Considerations in the Design of a Rotor with Smart Material actuated Trailing Edge Flaps // Proceedings of the 52nd International Annual Forum of the American Helicopter Society*. – Washington, USA, 1996. – pp. 704–714.
- [105] Straub F. K. and Charles B. D. *Aeroelastic Analysis Of Rotors With Trailing Edge Flaps Using Comprehensive Codes // Journal of the American Helicopter Society*. – 2001. – Vol.46(3). – pp. 192 – 199.
- [106] Strehlow H., Mehlhose R., Znika P. *Passive and Active Vibration Control Activities in the German Helicopter Industry // Proceedings of the Aerospace technology exhibition and conference (AEROTECH)*. – Muenchen, Germany, 1992. – 18 P.
- [107] Tang B. *Orthogonal array-based Latin hypercubes // Journal of the American statistical association*. – 1993. – Vol.88. – pp. 1392–1397.
- [108] Thakkar D, Ganguli R. *Active Twist Control of Smart Helicopter Rotor – a Survey // Journal of Aerospace Sciences and Technologies*. – 2005. – Vol.57(4). – pp. 429 – 448.
- [109] Walsh D.M. *Flight Tests of an Open Loop Higher Harmonic Control system of an S-76A Helicopter // Proceedings of the 42nd Annual Forum of the American Helicopter Society*. – Alexandria, USA, 1986. – pp. 831–843.
- [110] Weems D.B., Anderson D.M, Mathew M.B, Bussom R.C. *A Large-Scale Active-Twist Rotor // Proceedings of the 60th Annual Forum of the American Helicopter Society*. – Baltimore, USA, 2004. – 12 P.
- [111] Wierach P., Riemenschneider J. and Keye S. *Development of an Active Twist Rotor Blade with Distributed Actuation and Orthotropic Material // Proceeding of the Smart Structures and Materials: Smart Structures and Integrated Systems*. – 2005. – Vol.5764. – pp. 178 – 194.
- [112] Wierach P., Riemenschneider J., Opitz S. and Hoffmann F. *Testing and simulation of an active twist rotor blade // Proceeding of the Adaptronic Congress*. – Gottingen, Germany, 2007. – 9 P.

- [113] Wierach P., Riemenschneider J., Opitz S. and Hoffmann F. *Experimental Investigation of an Active Twist Rotor under Centrifugal Loads // Adaptive, tolerant and efficient composite structures.* – Springer–Verlag Berlin Heidelberg, 2013. – pp. 391–407.
- [114] Wickramasinghe V. and Hagood N. *Material characterization of active fiber composites for integral twist–actuated rotor blade application // Smart Material Structure .* – 2004. – Vol.13. – pp. 1155 – 1165.
- [115] Wilbur M.L., Yeager W.T., Wilkie W.K., Cesnik C. E. S. and Shin S. *Hover Testing of the NASA/ARMY/MIT Active Twist Rotor Prototype blade // Proceedings of the 56th Annual Forum of the American Helicopter Society.* – Virginia Beach USA, 2000. – 14 P.
- [116] Wilbur M.L., Mirick P., Yeager W.E.A., Langston C.W., Cesnik C.E.S. and Shin, S.J. *Vibratory Loads Reduction Testing of the Nasa/Army/MIT Active Twist Rotor // Journal of the American Helicopter Society.* – 2004. – Vol.47(2). – pp. 123 – 133.
- [117] Wilbur M.L., Sekula M.K. *The Effect of Tip Geometry on Active-Twist Rotor Response // Proceedings of the 61st International Annual Forum of the American Helicopter Society.* – Grapevine, USA, 2005. – 14P.
- [118] Wilkie W.K. *Anisotropic Piezoelectric Twist Actuation of Helicopter Rotor Blades: Aeroelastic Analysis and Design Optimisation. PhD thesis.* – Boulder: University of Colorado, 1997.
- [119] Wilkie W.K., Wilbur M. L., Mirick P.H., Cesnik C. E. S., Shin S. *Aeroelastic Analysis of the NASA/ARMY/MIT Active Twist Rotor // Proceedings of the 55th Annual Forum of the American Helicopter Society.* – Montreal, Canada, 1999. – 13 P.
- [120] Wood E.R., Powers R.W., Cline C.H. and Hammond C.E. *On Developing and Flight Testing a Higher Harmonic Control System // Journal of the American Helicopter Society.* – 1985. – Vol.30(1). – pp. 3 – 20.
- [121] Ye K.Q. *Column orthogonal Latin hypercubes and their application in computer experiments// Journal of the American statistical association.* – 1998. – Vol.93. – pp. 1430–1439.
- [122] http://commons.wikimedia.org/wiki/File:Fig._6_stalling.jpg.

APPENDIX A. Parametric study of rotor blade with C- spar

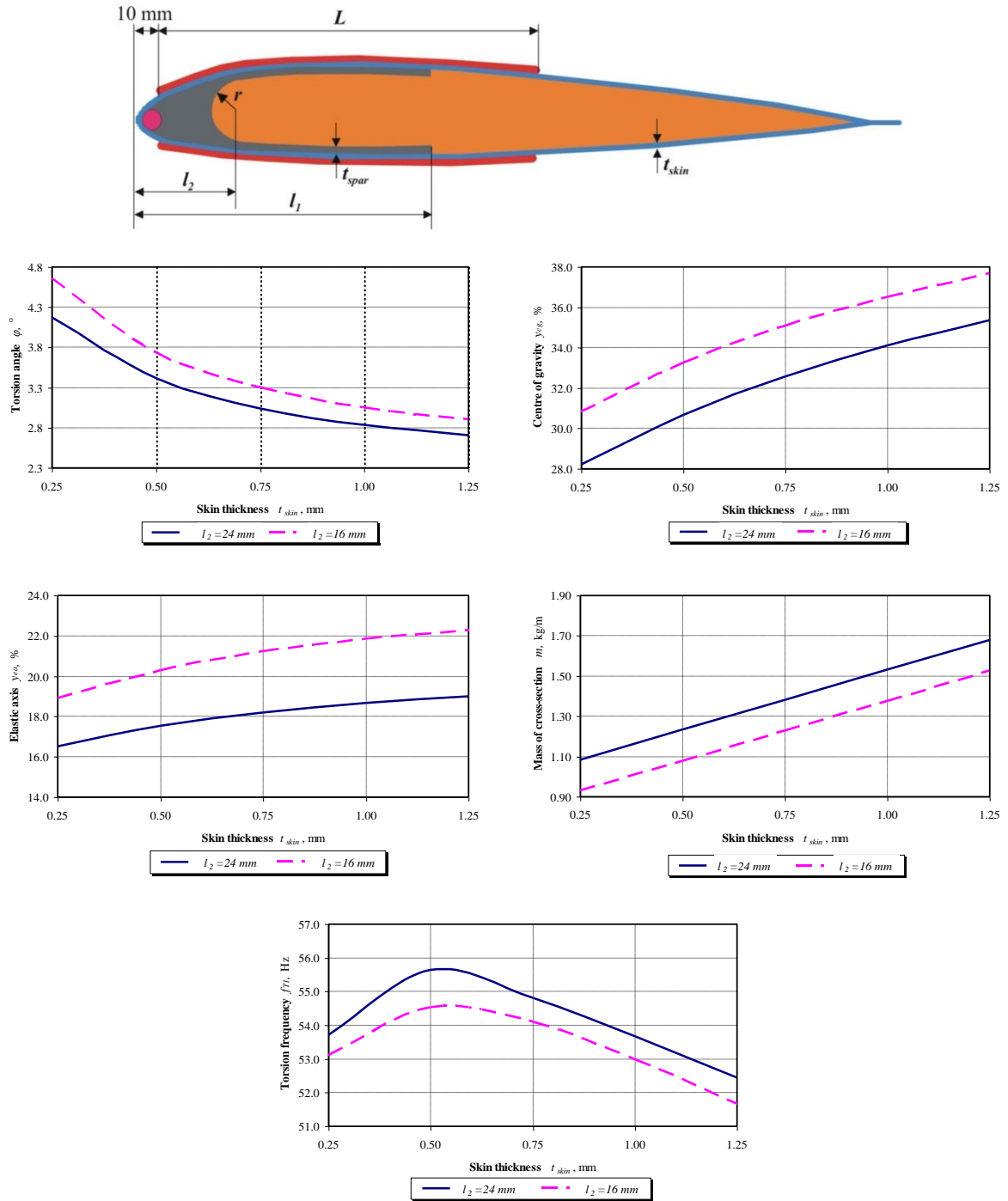


Figure A.1. Influence of the skin thickness t_{skin} on behaviour functions (Constant values: $l_1=48$ mm, $t_{spar}=1$ mm, $L=100$ mm)

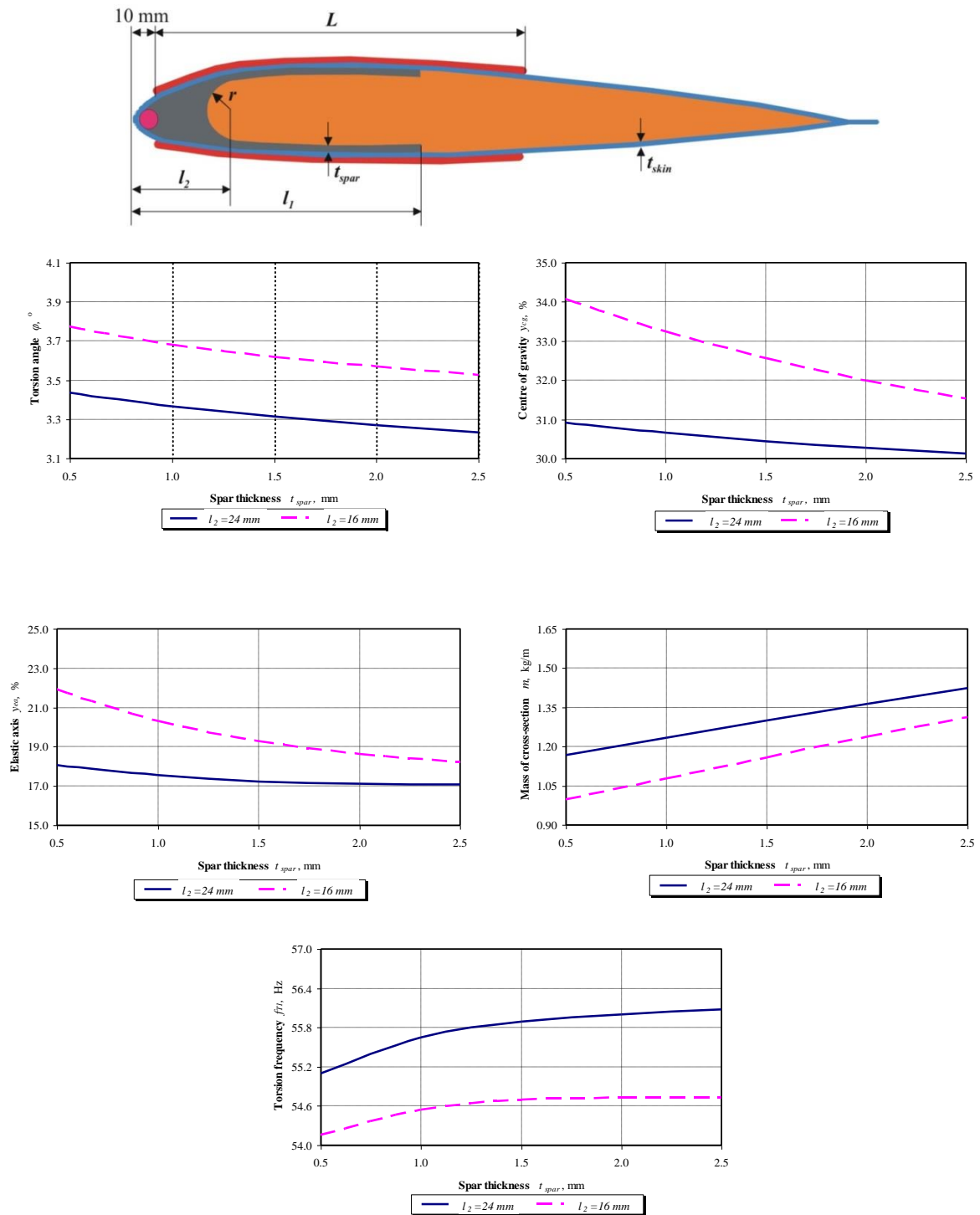


Figure A.2. Influence of the spar “moustaches” thickness t_{spar} on behaviour functions (Constant values: $l_1 = 48$ mm, $t_{skin} = 0.5$ mm, $L = 100$ mm)

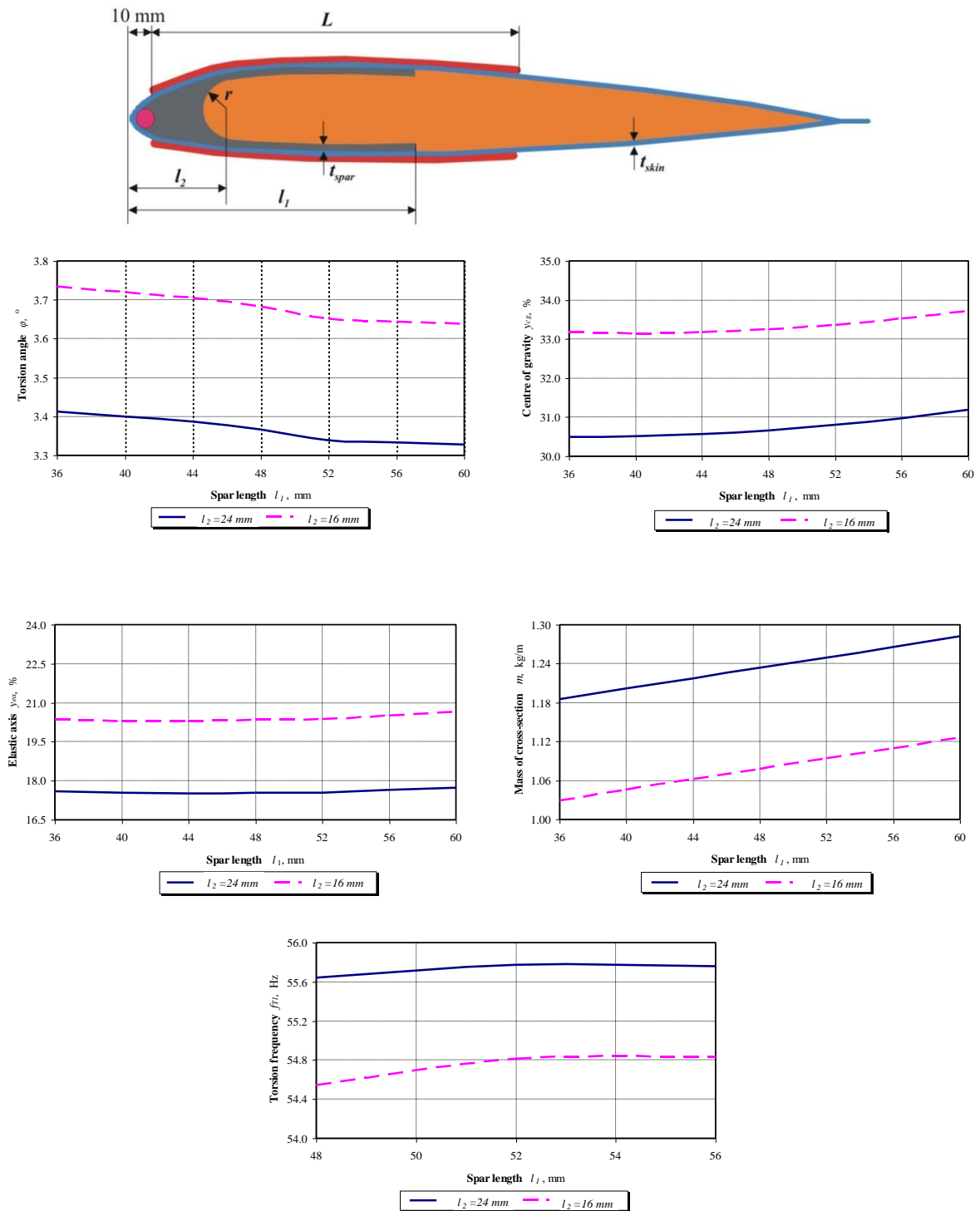


Figure A.3. Influence of the spar “moustaches” length l_1 on behaviour functions (Constant values: $t_{spar}=1$ mm, $t_{skin}=0.5$ mm, $L=100$ mm)

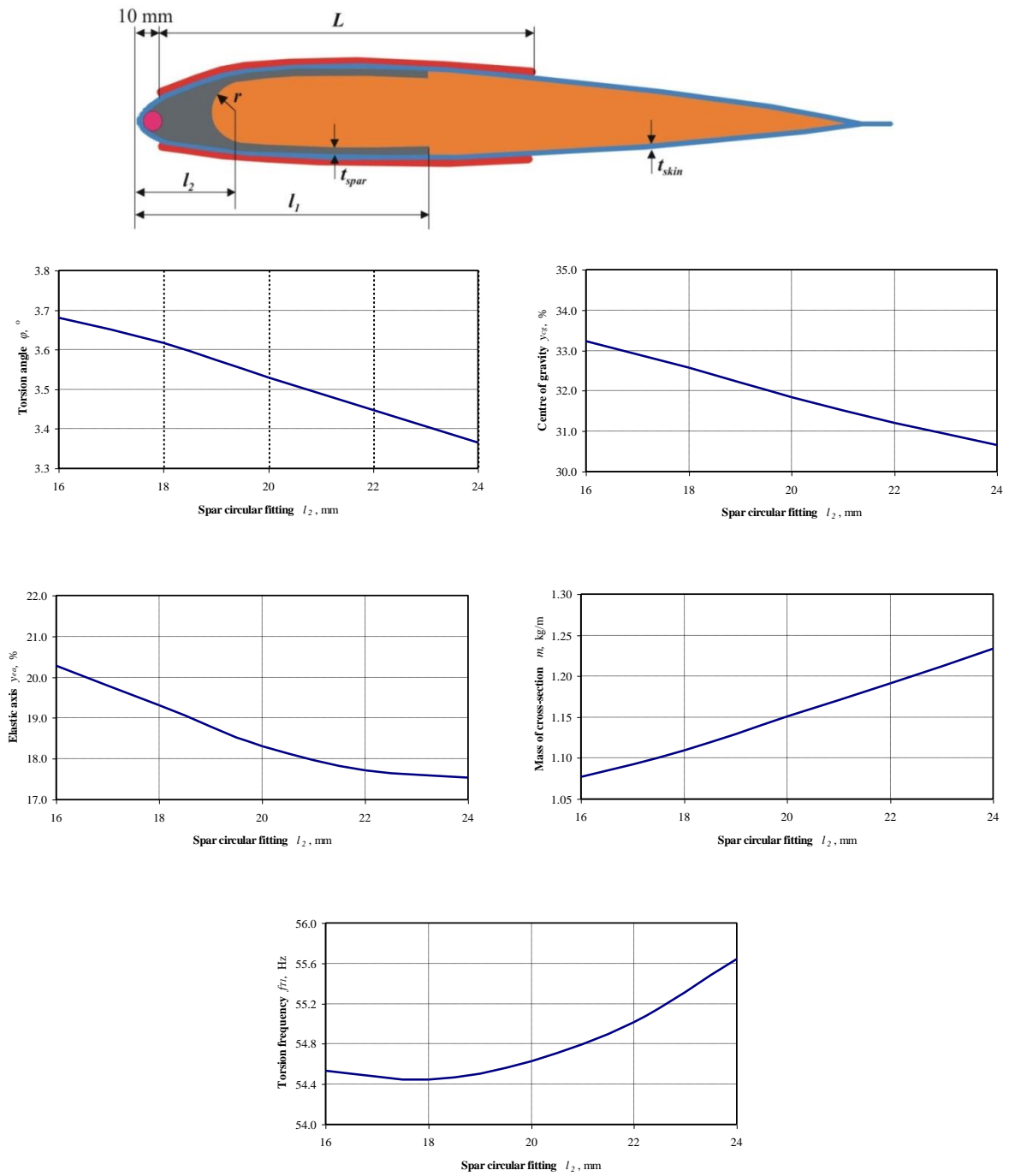


Figure A.4. Influence of spar circular fitting l_2 on behaviour functions
(Constant values: $t_{spar}=1$ mm, $l_1=48$ mm, $t_{skin}=0.5$ mm, $L=100$ mm)

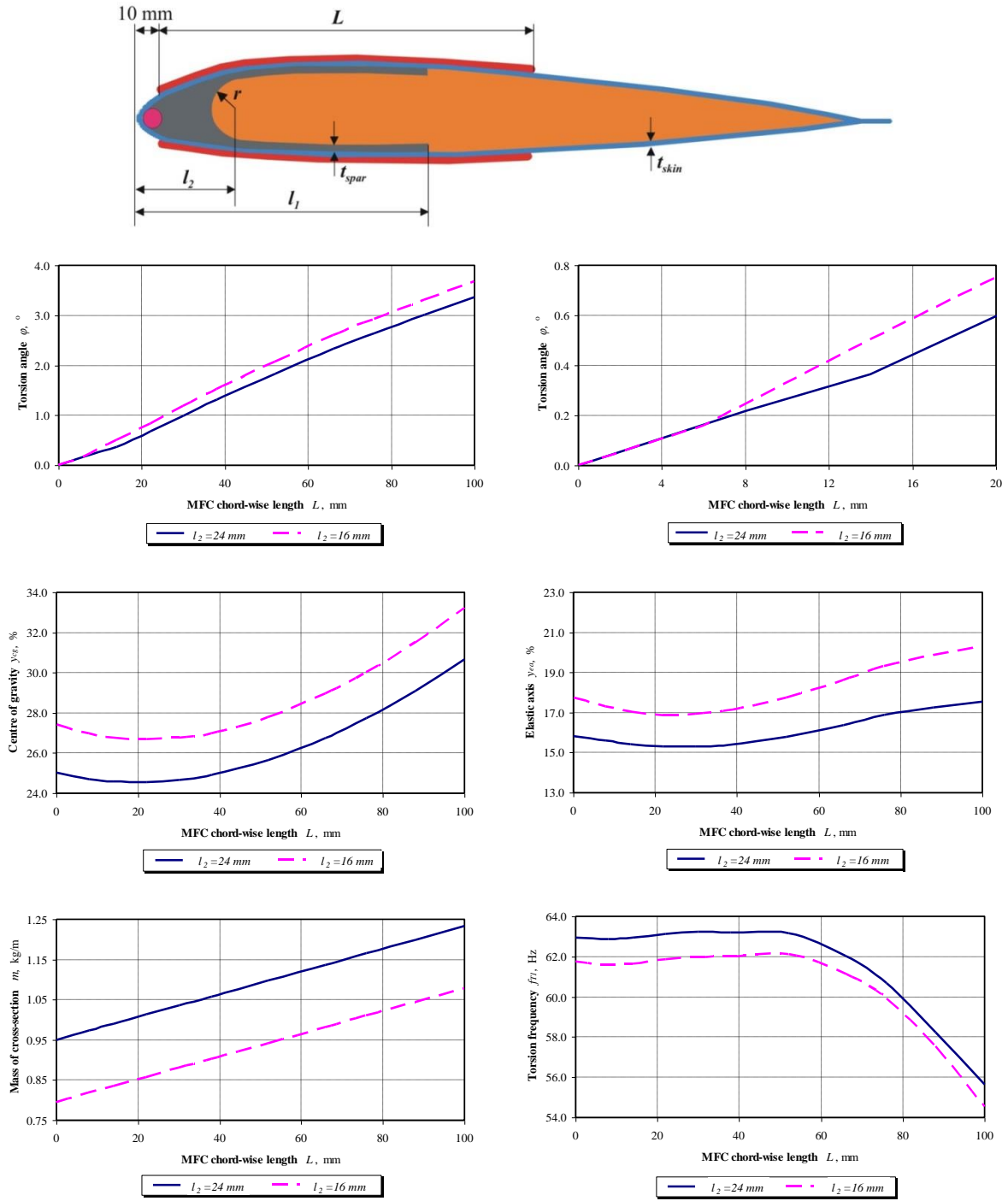


Figure A.5. Influence of MFC actuator chordwise length L on behaviour functions
 (Constant values: $t_{spar}=1$ mm, $l_1=48$ mm, $t_{skin}=0.5$ mm, $V=1000$ V)

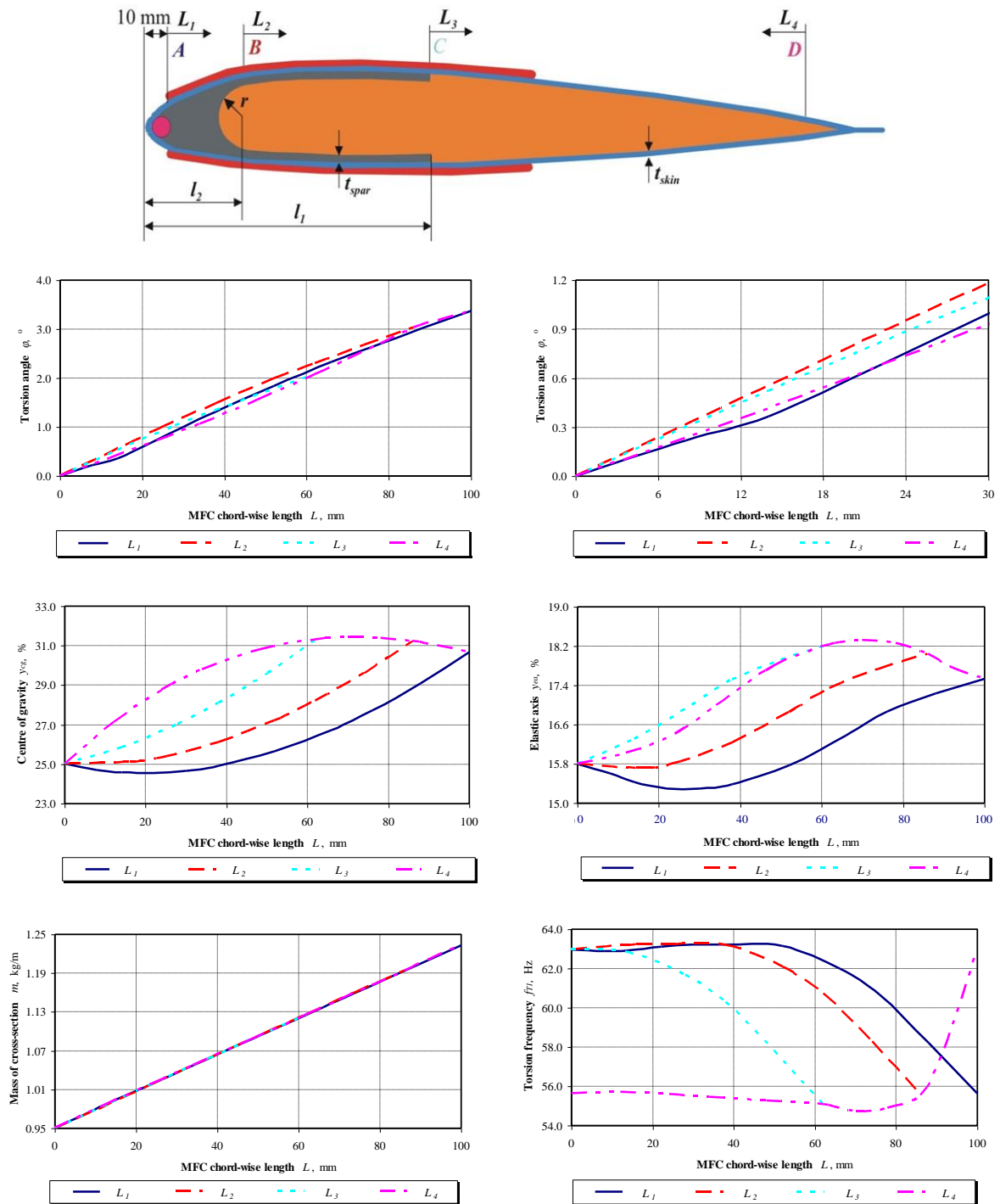


Figure A.6. Influence of MFC actuator chordwise length and gluing variant on behaviour functions (Constant values: $l_1=48$ mm, $l_2=24$ mm, $t_{spar}=1.0$ mm, $t_{skin}=0.5$ mm)

APPENDIX B. Parametric study of rotor blade with D- spar

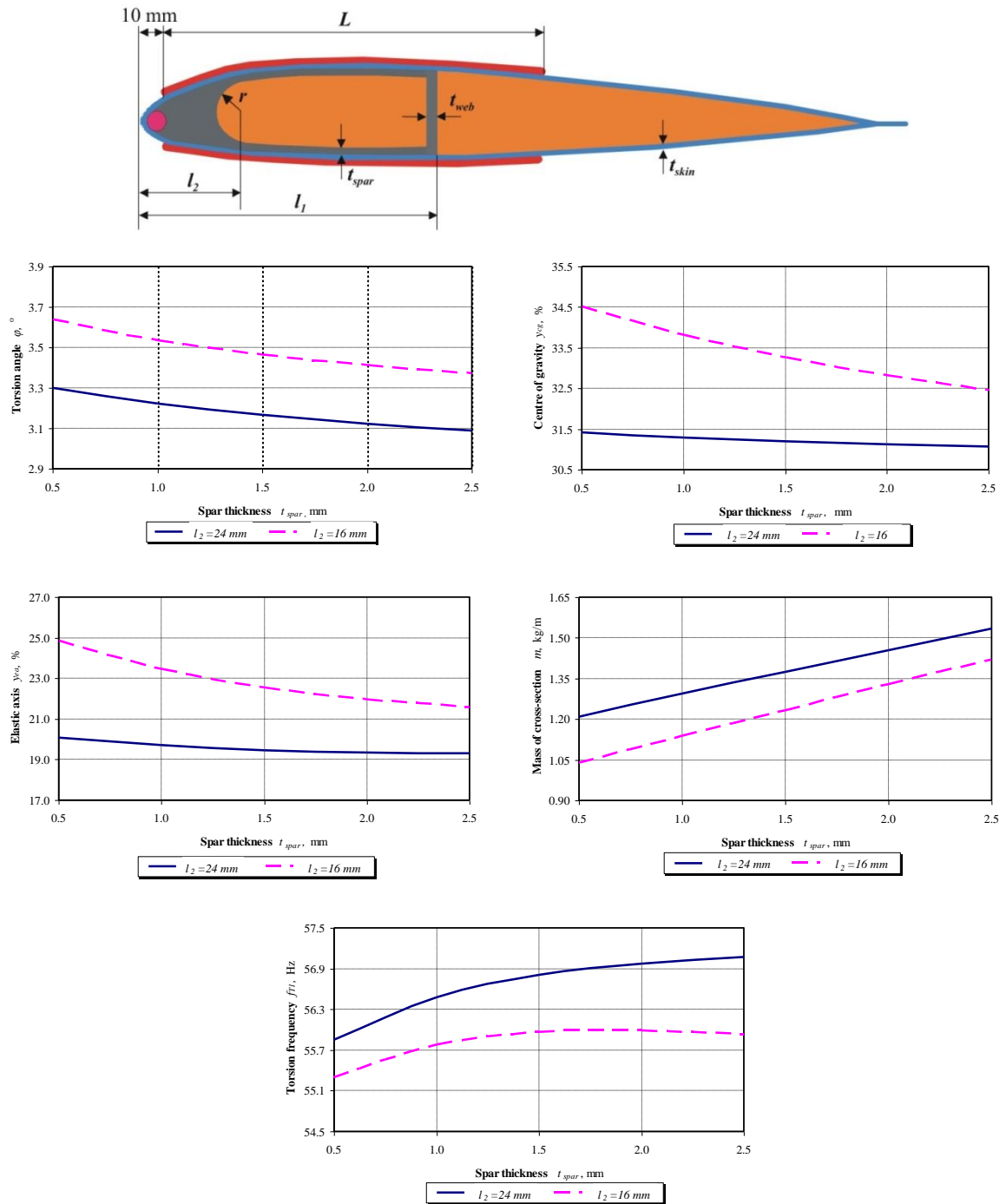


Figure B.1. Influence of the spar “moustaches” thickness t_{spar} on behaviour functions (Constant values: $l_1=56\text{ mm}$, $t_{skin}=0.5\text{ mm}$, $t_{web}=1.0\text{ mm}$, $L=100\text{ mm}$)

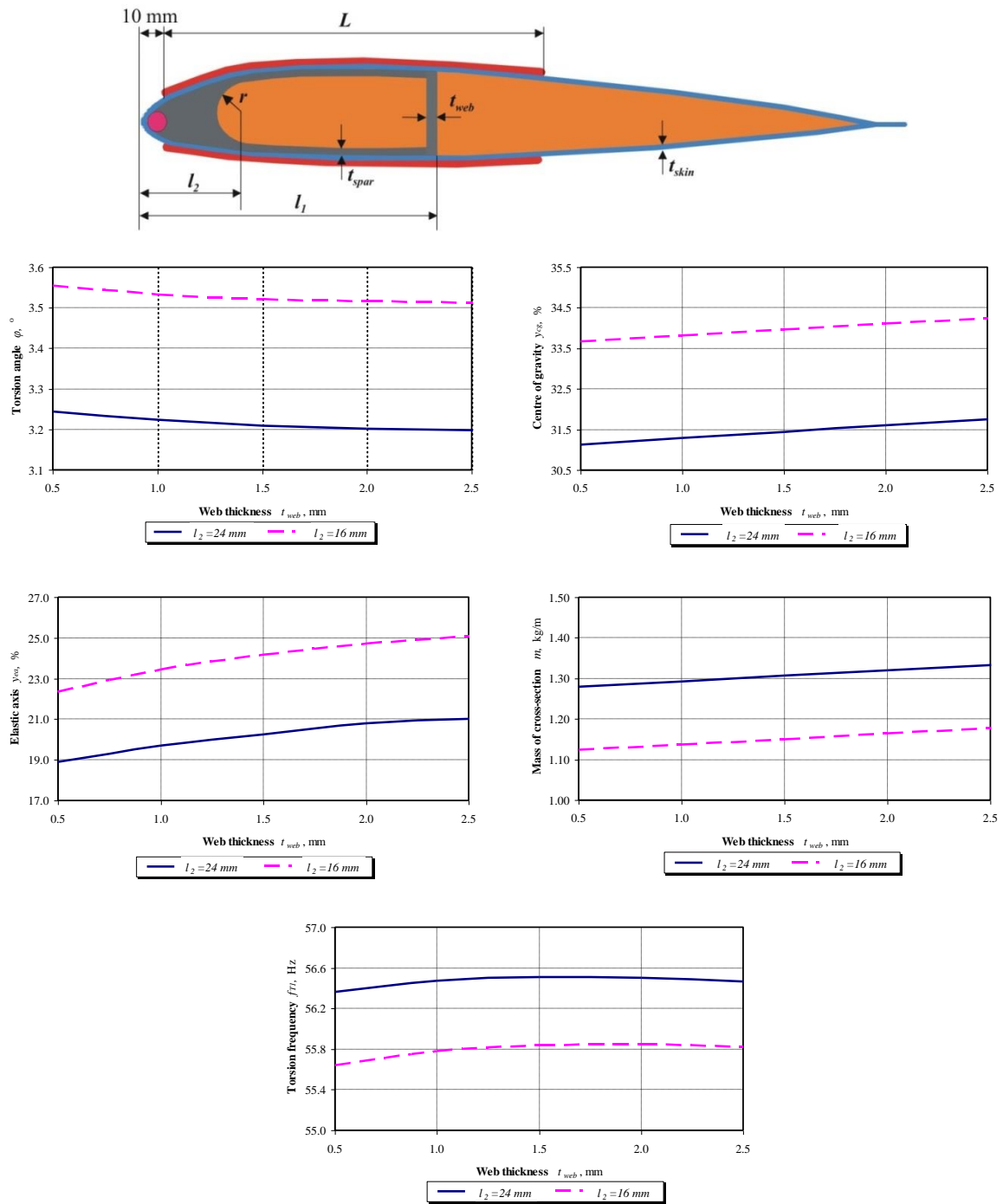


Figure B.2. Influence of the web thickness t_{web} on behaviour functions
(Constant values: $l_1=56$ mm, $t_{skin}=0.5$ mm, $t_{spar}=1.0$ mm, $t_{web}=1.0$ mm, $L=100$ mm)

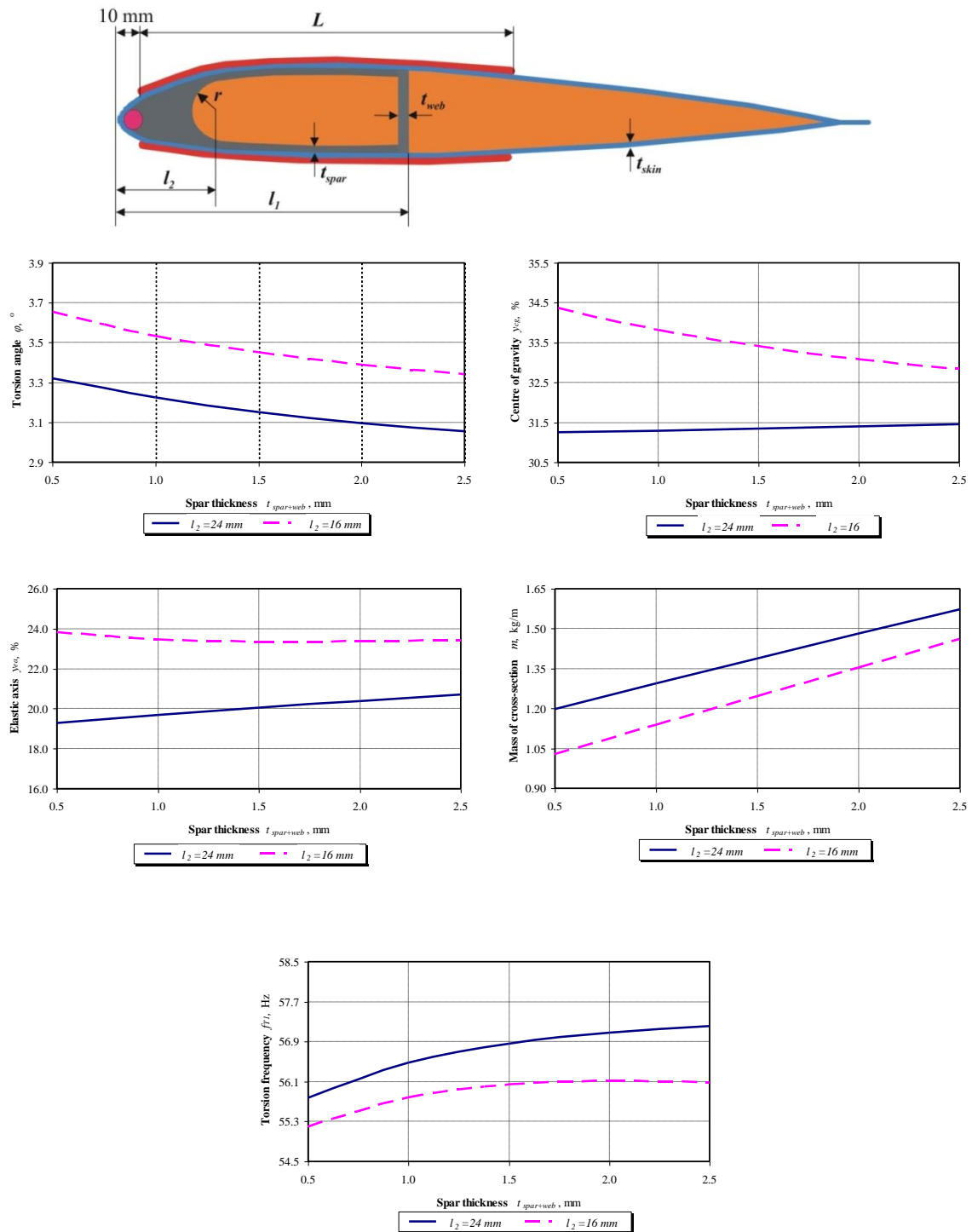


Figure B.3. Influence of the spar and web thickness $t_{spar}=t_{web}$ on behaviour functions (Constant values: $l_1=56$ mm, $t_{skin}=0.5$ mm, $t_{spar}=1.0$ mm, $t_{web}=1.0$ mm, $L=100$ mm)

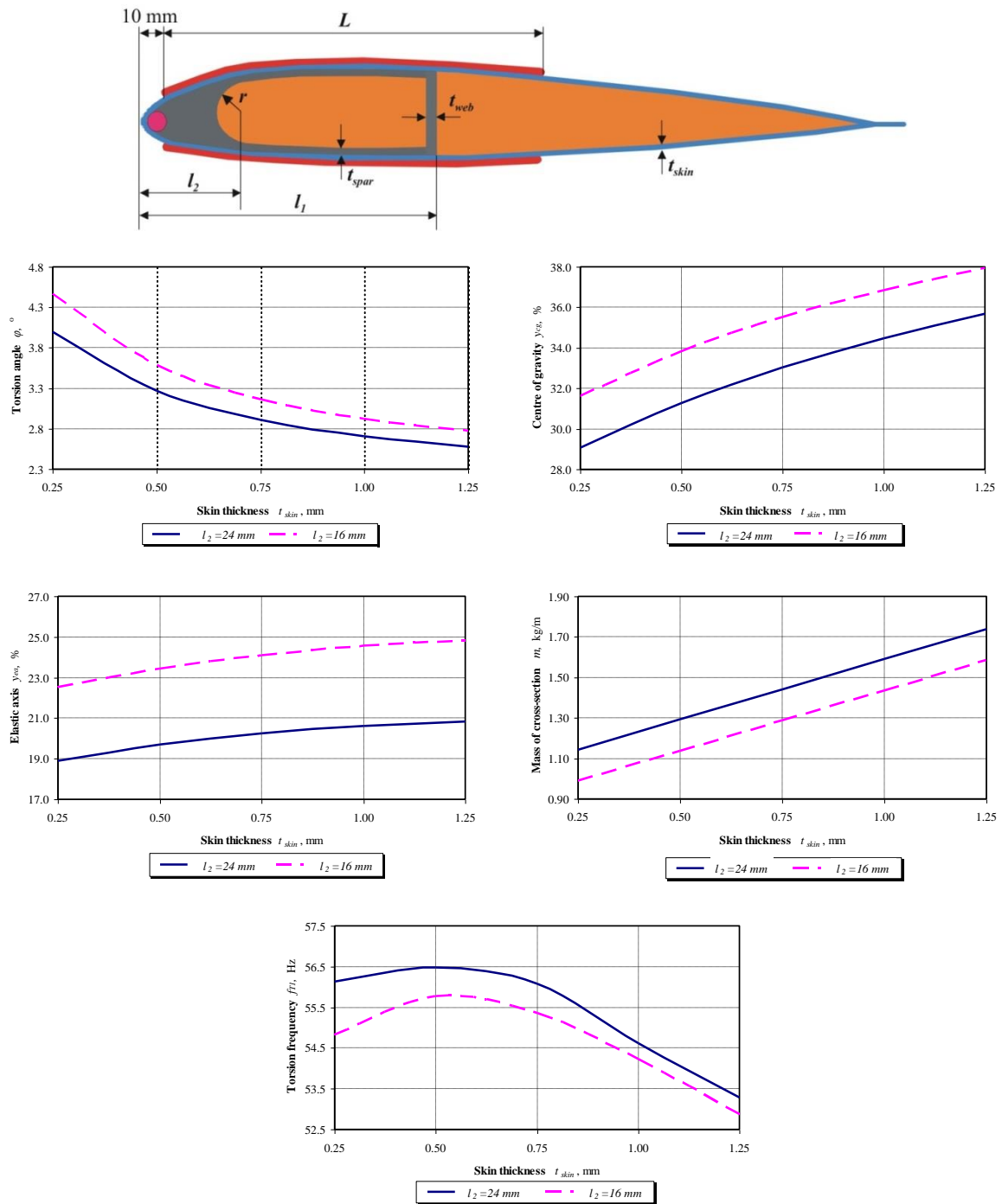


Figure B.4. Influence of skin thickness t_{skin} on behaviour functions
 (Constant values: $l_1=56$ mm, $t_{skin}=0.5$ mm, $t_{spar}=1.0$ mm, $t_{web}=1.0$ mm, $L=100$ mm)

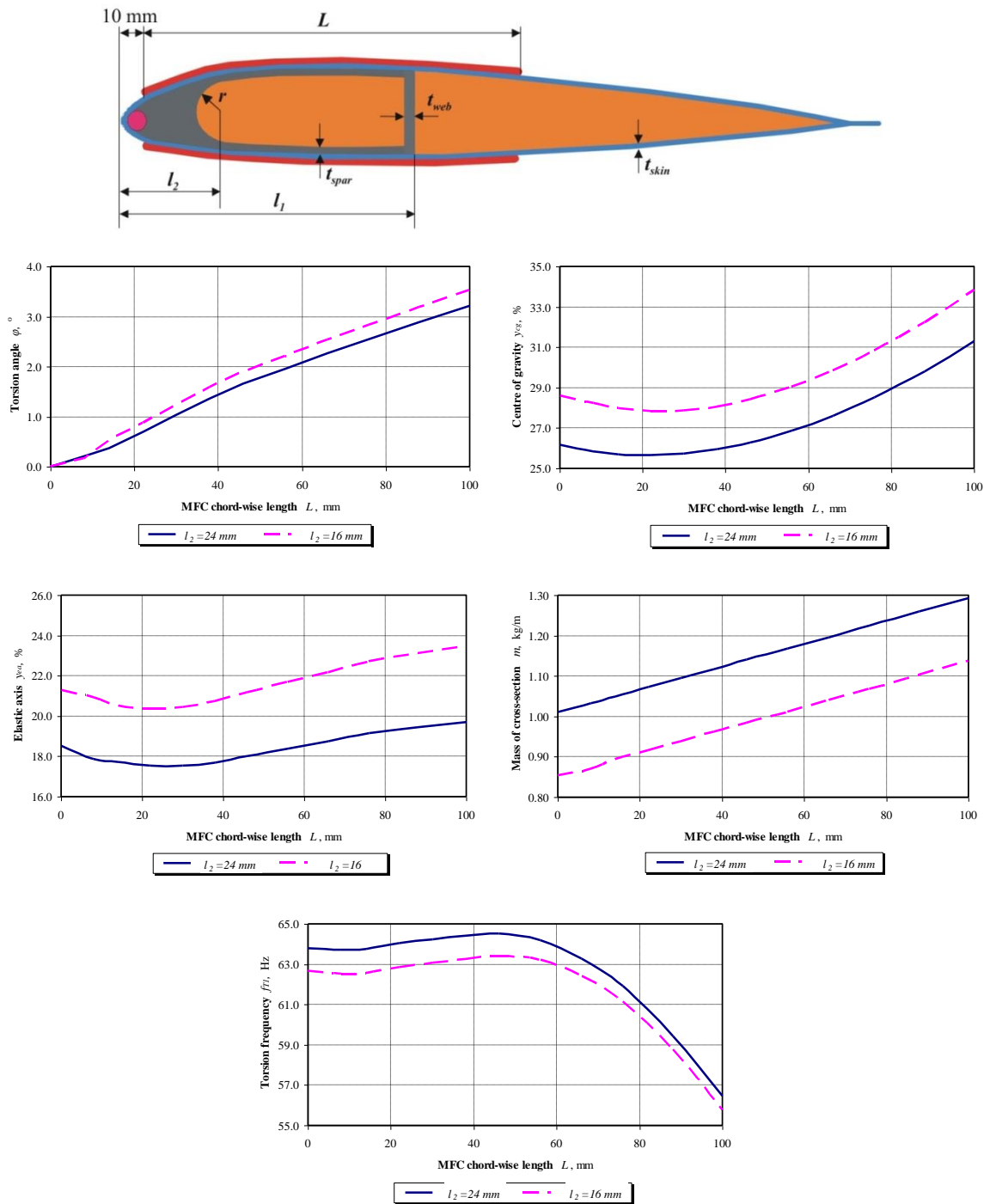


Figure B.5. Influence of the MFC actuator chordwise length L on behaviour functions (Constant values: $l_1=56$ mm, $t_{skin}=0.5$ mm, $t_{spar}=1.0$ mm, $t_{web}=1.0$ mm, $V=1000$ V)

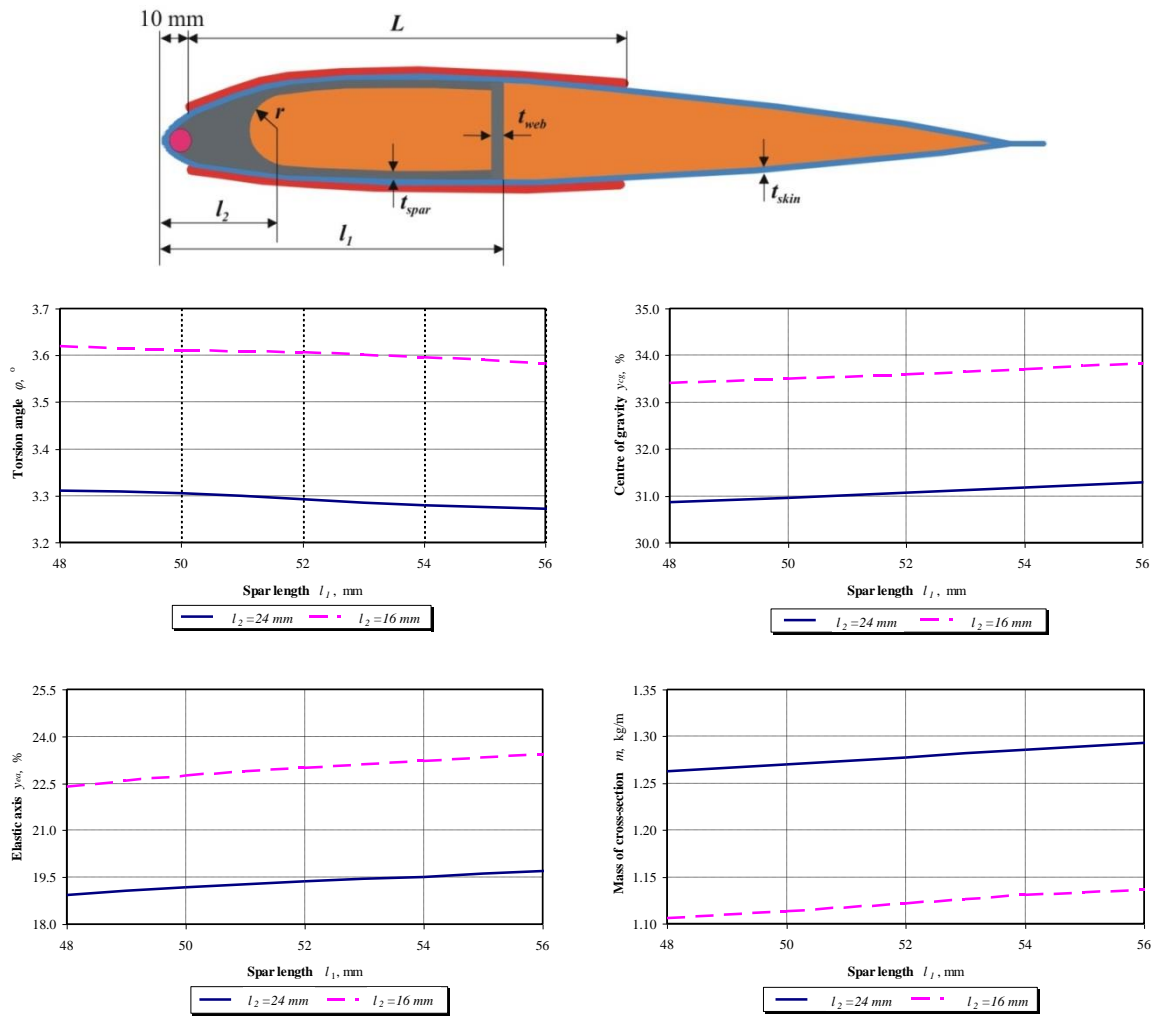


Figure B.6. Influence of the spar “moustaches” length l_1 on behaviour functions
(Constant values: $t_{spar}=1.0$ mm, $t_{skin}=0.5$ mm, $t_{web}=1.0$ mm, $L=100$ mm,)

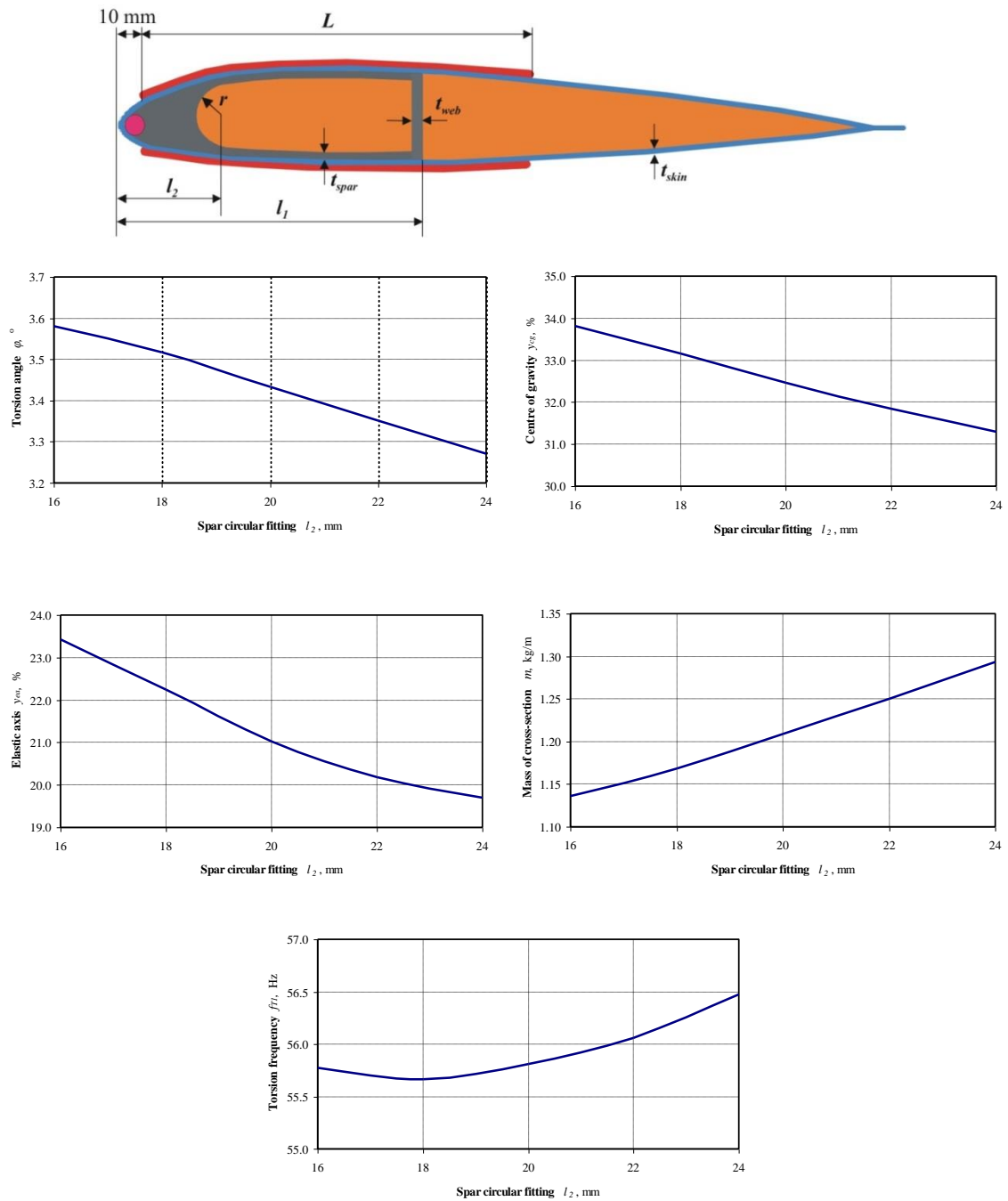


Figure B.7. Influence of the spar circular fitting l_2 on behaviour functions
 (Constant values: $l_1=56$ mm, $t_{spar}=1.0$ mm, $t_{skin}=0.5$ mm, $t_{web}=1.0$ mm, $L=100$ mm)

CURRICULUM VITAE

Andrejs Kovalovs

11 April 1975, Riga, Latvia

EDUCATION

- 2010 – 2011 Riga Technical University, Civil Engineering faculty, Master's degree (M.Sc.)
- 1999 – 2004 Riga Technical University, Civil Engineering faculty, Theoretical course of PhD program (75%).
- 1997 – 1999 Riga Aviation University, Mechanical faculty, Master's degree (M.Sc.)

ADDITIONAL EDUCATION

01.11. – 01.12.2003 exchange program Tempus, Martin-Luther-University Halle-Wittenberg, Germany.

WORK EXPERIENCE

- 2012 – Lecturer, Riga Technical University, Civil Engineering Faculty, Department of Composite Materials and Structures
- 2012 – Researcher, Riga Technical University, Civil Engineering Faculty, Institute of Materials and Structures.
- 2004 – 2012 Researcher, Riga Technical University, Civil Engineering Faculty, Centre of Construction Science.